TRANSIENT ELECTRON-PHONON INTERACTION AND ULTRASONIC GENERATION IN CdS

A thesis submitted to the

University of Leicester

by

D.J.Somerford B.Sc.,

for the degree of Doctor of Philosophy

in the Faculty of Science

1968

ProQuest LLC
789 East Eisenhower Parkway
P.O. Box 1346
Ann Arbor, MI 48106-1346

CONTENTS

Acknowledgements.

The author wishes to thank Professor E.A.Stewardson for the opportunity to undertake research in his department. He is greatly indebted to Dr.W.E.Spear for suggesting the problem and the generous help and guidance given continually throughout the investigation.

Thanks are also due to Dr.A.Weinmann and Dr. P.G.LeComber for their helpful discussions throughout the course of this work.

The author would like to express his gratitude to his wife for her help in the preparation of this thesis. Finally, the financial support of the S.R.C. is gratefully acknowledged.

ABSTRACT.

This thesis describes experimental work on the interaction of the drifting charge carriers with the piezoelectric lattice modes in highly resistive CdS crystals. In these experiments the specimens were fitted with evaporated metal electrodes on opposite faces, and a fast electron or light pulse generated electron-hole pairs in a narrow region below the top electrode. The crystals were mounted on a silica buffer rod with a quartz transducer on its opposite end. A synchronized field pulse drew a thin space charge layer out of this region and the transit time and drift velocity were obtained directly. The new feature of this work is the simultaneous detection of the generated piezoelectric wave in a frequency range from 3 to 75 Mc/s.

The results show a close correlation between the ultrasonic measurements and those features of the drift velocity experiments associated with the transient acoustoelectric interaction. The amplitude of the piezoelectric wave has been studied as a function of the applied field, temperature, excitation pulse length, electron beam current and beam energy (5 - 35 keV) and also as a function of steady, highly absorbed light incident on the specimen top surface. From the measurements it has been possible to estimate the value of the piezoelectric field. This is sufficient to explain the non-ohmic behaviour of the drift velocity versus applied field curves.

On the basis of the above results a microscopic model is proposed. A single incident electron is considered which simultaneously generates

an elementary piezoelectric wavelet and a distribution of free electrons within a few microns of the surface. The local interaction of the electrons with the wavelet leads to ultrasonic amplification in accordance with the White theory. The significance of the surface barrier in connection with the amplification is discussed. A quantitative estimate is made of the local density of the bunched carriers which, on the basis of the White theory, leads to a build-up time of the interaction of less than 10 nsec. The results of this analysis resolve one of the main difficulties in the understanding of the transient acoustoelectric interaction.

CHAPTER 1

Introduction

Since the discovery in 1961 of ultrasonic amplification in CdS considerable interest has been shown in the interaction of the drifting electrons with the piezoelectric lattice modes.

The various studies of ultrasonic amplification and of the associated current saturation effects have given valuable information on the acoustoelectric interaction in semiconducting and photoconducting CdS. The majority of the work was, however, carried out under steady state conditions.

Recently, a new, and more direct approach to the study of the acoustoelectric interaction has been used. It is based on transient methods that allow a study of the interaction during a single transit of the charge carriers. In this work, which is reviewed in Section 2.3 of this thesis, a strong localized interaction was observed in highly resistive CdS specimens. Several basic problems regarding the nature of the mechanism of the interaction remained unsolved.

The main purpose of the work discussed in this thesis has been to study and further clarify the mechanism underlying the transient acoustoelectric interaction. In particular, it has been possible to detect the generated stress wave, and measurements of its amplitude were correlated with those on the drift velocity of the charge carriers.

The interpretation of the results is discussed in Chapter 6,

where a microscopic model for the interaction is presented.

CHAPTER 2

Survey of the Previous Work

2.1 The Acoustoelectric Interaction in the II – VI Compounds.

Single crystals of the II–VI compounds are strongly piezoelectric. It is interesting to compare the piezoelectricity in CdS with that of quartz. For X-cut quartz, the electro-mechanical coupling constant K = 0·095, while for CdS K≃0·2 [Hutson (1960)]. The square of the constant K is the ratio of mechanical energy stored in the piezoelectric material to the electrical energy supplied to it, and hence K is a measure of the efficiency of a piezoelctric transducer.

When a stress wave propagates through a piezoelectric medium strong variations in the local electric field may be produced. In a material of sufficiently high electrical conductivity, the mobile carriers will interact with the fluctuating local field. Hutson and White (1962) formulated a linear theory of this interaction, the main aim of which was to predict the attenuation of the stress wave under these conditions.

An important contribution was made in 1962 by White, who included in his linear theory the effect of a steady electric field across the specimen. His results showed clearly that under certain conditions momentum may be transferred from the carriers to the piezoelectric modes at a rate that more than compensated for the internal losses. This suggested that amplification of a piezoelectric wave should be possible in principle. The White theory is a classical linear small-

signal analysis of the interaction between the charge carriers and the piezoelectric vibrational modes. The analysis combined the electrical continuity equation, Poisson's equation, the piezoelectric equations of state [see Section 3.1, equations (3.1) and (3.2)], and carrier diffusion effects in a single analytical solution. The amplification mechanism is closely related to the space charge bunching by the piezoelectric field and in this respect there exists an analogy to amplification in a travelling wave tube.

The approximate solution obtained by White for the attenuation of an acoustic wave is given by

$$\alpha = \frac{K^2 \omega_c}{2 \gamma v_s} \left[1 + \frac{\omega_c^2}{\gamma^2 \omega^2} \left(1 + \frac{\omega^2}{\omega_c \omega_D} \right)^2 \right]^{-1} \qquad (2.1)$$

Here, α denotes the attenuation in Nepers cm^{-1}, ω the angular frequency, and v_s the phase velocity of the ultrasonic wave. The conductivity parameter ω_c is equal to $\frac{4\pi\sigma}{\varepsilon}$, where σ denotes the conductivity of the medium; ω_c is the reciprocal of the dielectric relaxation time. The effect of carrier diffusion on the local space charge enters into the expression through the diffusion frequency $\omega_D = \frac{v_s^2}{f D}$. The factor f is defined in terms of the lattice mobility μ_L, such that the product $f\mu_L$ is the drift mobility controlled by those traps from which the carriers are released in times short compared with the period of the sound wave. The dependence of the attenuation on the applied field is given by,

$$\gamma = 1 - \frac{f \mu_L E_o}{v_s} \qquad (2.2)$$

When the effective drift velocity $f\mu_L E_o$ is less than v_s , γ and α are positive and the wave is attenuated; if $f\mu_L E_o > v_s$, γ and α are negative, that is, amplification occurs. The changeover from attenuation to gain occurs at $\gamma = 0$ which corresponds to the carriers drifting with the appropriate sound velocity.

Thus, White's theory predicts that the attenuation should change sign when the drift velocity v_d of the electrons is equal to the sound velocity v_s , i.e. at

$$f\mu_L E' = v_s \qquad (2.3)$$

Hutson, McFee, and White (1961) were the first to demonstrate the ~~predicted~~ amplification of an acoustic wave. Their arrangement is shown in fig.2.1 (a). A pulsed ultrasonic shear wave generated by a quartz transducer T_1 was passed through a silica buffer into a large CdS crystal, 7mm in length. The direction of propagation was perpendicular to the hexagonal c-axis of the specimen and the transmitted wave detected by the transducer T_2. The conductivity σ of the specimen was increased to about 10^{-4} $(\text{ohm cm})^{-1}$ by illumination with weakly absorbed light.

The measured attenuation α is shown in fig.2.1 (b) as a function of the applied field E_o. The zero of attenuation was chosen as the value of α in the absence of illumination. When the electrons drifted in the same direction as the ultrasonic wave the applied field was taken to be positive. Frequencies of both 15 Mc.sec^{-1} and 45 Mc.sec^{-1} were used. It can be seen that above a certain critical field E' the

attenuation changed sign and became negative. This corresponds to amplification of the stress wave. These results were found to be in good agreement with the White theory.

Many attempts [Uchida, Ishiguro, Sasaki and Suzuki (1964), Blotekjaer and Quate (1964), and Gurevich and Laikhtman (1964)] have been made to refine the linear theory of White and to include the effects of non-linear terms. However, the small signal theory of White has met with considerable success in explaining the observed ultrasonic amplification and its dependence on such factors as conductivity, crystallographic direction, frequency and applied field.

The White theory and similar analyses are only valid when the wavelength λ of the sound wave is longer than the electron mean free path Λ, which limits its applicability to sound frequencies $\lesssim 10^{10}$ c.p.s. Under these conditions the electrons are able to come into equilibrium with their immediate surroundings. For shorter wavelengths, when $\lambda < \Lambda$, (or $q\Lambda > 1$, where q is the phonon wave vector), it is more appropriate to consider quantum-mechanically the interaction of electrons and phonons. A calculation along these lines was carried out by Prohofsky in 1964. The basis of this work was the suggestion made by Pippard (1963) that the phenomenon of acoustic amplification may be understood by considering the stimulated emission of phonons by electrons having supersonic drift velocities.

In this approach, Prohofsky proposed that a piezoelectrically active phonon band is built up. The normal electron momentum loss

mechanism in the absence of stimulated emission is illustrated in fig. 2.2 (a). The momentum is lost in collisions with optical phonons and very high frequency acoustic phonons with frequencies of the order of 10^{13} c.p.s. When E_o is increased to values greater than E' the stimulated emission processes will populate a piezoelectric phonon band, fig. 2.2 (b). The equilibrium value of the phonon density in this piezoelectric band will be governed by two factors: their rate of generation and their rate of loss. The rate of generation will depend on the applied field and on the number of carriers present, i.e. on the conductivity. Conversion to higher frequency phonons will be a major source of loss. However, the time constant associated with this conversion is relatively long, and the build-up of a large density of piezoelectric phonons is therefore possible. The additional loss of electron momentum to this band of phonons will reduce the electron mobility, giving rise to pronounced non-ohmic behaviour.

Non-ohmic behaviour was first observed by Smith (1962) in semiconducting CdS, $\left[\sigma \sim 0{\cdot}1 \text{ (ohm cm)}^{-1}\right]$ .He found that Ohm's law was obeyed for values of E_o less than a certain critical value E'. For $E_o > E'$, a significant decrease in the slope of the i-E_o characteristic was observed, as shown in fig. 2.3. The results indicated that the onset of this effect occurred when the electron drift velocity was just greater than the sound velocity in the specimen. It was recognised by Smith that the observed effect was closely related to the ultrasonic amplification mechanism.

Using photoconducting CdS, he was also able to show that the change of gradient became less pronounced as the conductivity was decreased, whilst at conductivities less than 10^{-5} $(\text{ohm cm})^{-1}$ the current was completely ohmic.

The work of McFee (1963) clarified the relation between the current saturation effect and ultrasonic amplification. McFee's experimental arrangement was similar to that shown in fig. 2.1 (a), but without the input transducer and buffer. It permitted the direct measurement of the build-up of ultrasonic flux within the specimen under conditions of current saturation. The output transducer and detecting system were tuned to frequencies in the range from 45 to 1000 Mc.sec^{-1}. The results obtained are shown in fig. 2.4. The conductivity of the CdS under uniform excitation was about 3×10^{-5} $(\text{ohm cm})^{-1}$. The top trace shows the voltage pulse applied to the crystal and the middle trace the corresponding current flow. The current was initially ohmic but decreased to a steady state value in about 80 μsec. This behaviour was very similar qualitatively to that observed by Smith.

The lower trace in fig. 2.4 shows the build-up of ultrasonic flux from the piezoelectric thermal vibrations present in the cyrstal, as detected by the transducer T_2. The significant feature is the correlation between the decay of the current and the growth of the ultrasonic flux.

The phenomenon of current saturation has been used to determine

the electron drift mobility in CdS. Smith and Moore (1964) and Hamaguchi, Otsuki, Watanabe and Inuishi (1964), obtained the mobility as a function of temperature.

2.2 Current Oscillations and Domains.

It is possible to observe current oscillations in both semiconducting and photoconducting CdS when the electron drift velocity exceeds the sound velocity. These oscillations are intimately related to the existence of domains, which are regions of high acoustic intensity and high acoustoelectric field [Haydl and Quate (1966)].

In the first part of this section the variation of electric field, current density, and acoustic power density in the presence of a moving domain is discussed. The final part of this section will be concerned with stationary domains.

The square wave type current oscillations discovered in semiconducting CdS (shear wave orientation) by Haydl (1967) are taken as an example in this discussion. In fig. 2.5 (a), the current density J is plotted against the applied field E_o. The graph is divided into two regions; that of acoustic attenuation and acoustic gain. The critical field is designated by E', while E_t is an oscillation threshold field, above which the current was found to oscillate between an ohmic value J_1 and a lower value J_a.

In fig.2.5 (b) the current waveform is shown as a function of time. The time t_o at which the current suddenly decreased, was found

to decrease with increasing applied field. The oscillation period τ is equal to the acoustic shear wave transit time between the electrodes. The electric field distribution, which was determined by using probes placed along the specimen, is shown in fig.2.5 (c) as a function of time. The field remains ohmic for a time t_o, after which time a narrow high field region develops at a distance $\ell_o = v_s t_o$ from the cathode. This region grows in amplitude within a short drift distance via the accustoelectric amplification mechanism. This high field region is the domain. The domain amplitude remains constant while it travels towards the anode at the shear wave velocity, where it collapses at time τ.

Finally, the acoustic noise distribution as a function of distance is shown in fig.2.5 (d). The acoustic thermal noise is amplified for a time t_o corresponding to a distance ℓ_o from the cathode. When the domain forms, the noise grows further inside the domain and decays in the bulk of the sample since the field there is only equal to E_a which is too low to amplify the noise. The acoustic pulse travels with the high field region towards the anode at the velocity of sound. During this time the current remains at the lower value J_a. When the domain reaches the anode, the field in the bulk rises again and the process repeats.

In any theoretical description of the above phenomena, a detailed explanation of domain formation must be included. The phenomena of negative differential bulk conductance (Ridley 1963), which is characterized by the periodic build-up of a very high and narrow

electric field region which travels in the direction of carrier flow is of particular interest here.

The mechanism of acoustic amplification may cause negative differential conductivity. Thus, the total current through the crystal in the presence of an acoustoelectric field E_{ae}, can be written

$$J_t = \sigma\left(E_o - E_{ae}\right) \tag{2.4}$$

where σ is the low field conductivity and E_o is the applied field. The differential conductivity (the slope of the $J - E_o$ curve) is given by

$$\frac{dJ_t}{dE_o} = \sigma\left(1 - \frac{dE_{ae}}{dE_o}\right) \tag{2.5}$$

Therefore, the condition for negative differential conductivity is given by

$$dE_{ae} / dE_o > 1. \tag{2.6}$$

The probable explanation for the observed current oscillations is therefore as follows. An acoustic signal originating from thermal acoustic noise is amplified, and when it has reached a certain threshold level [at $t = t_o$ in fig.2.4 (d)] , a negative differential conductivity appears and a domain is formed. This domain causes the current to oscillate by the mechanism discussed above.

Stationary domains in photoconductive CdS have been observed by McFee and Tien (1966). They have shown that in the current saturated condition a region of high electric field exists near the anode. The presence of this domain may be explained as follows. As the saturation

is caused by travelling wave amplification of acoustic waves, it is expected that the acoustic energy would tend to accumulate in the direction of carrier drift. This spatially nonuniform distribution of acoustic flux will in turn cause a nonuniform electric field distribution. The field distribution within the specimen is shown in fig.2.6 (a) under both non-ohmic and ohmic conditions. The field under ohmic conditions was found to be reasonably constant, as should be the case for a homogeneous sample. In an inhomogeneous sample however, a field distribution under non-ohmic conditions quite different from the previous sample was evident [fig.2.6 (b)]. For this sample the domain was located in the region of the inhomogeneity approximately midway between the two electrodes.

2.3 Transient Acoustoelectric Interaction in CdS and ZnS Crystals.

The interaction between drifting charge carriers and piezoelectric lattice modes during a single transit has recently been observed by LeComber, Spear and Weinmann (1966)* The above work was unique in that highly non-uniform pulse excitation was used, which generated a thin layer of drifting carriers in a highly resistive specimen. This technique allowed the direct determination of the carrier drift velocity v_d.

Drift velocity experiments at room temperature were carried out on numerous crystals of CdS and ZnS. The significant fact of all the

* In the remainder of this thesis, this paper will be referred to as paper I.

(v_d, E_o) curves, one of which is reproduced in fig.2.7, was the abrupt discontinuity in slope at a drift velocity v_d' . In each case the value of v_d' was in good agreement with the velocity of sound v_s in the appropriate crystallographic direction.In view of this good correlation, there seemed little doubt that the observed effect was caused by the interaction of the charge carriers with the piezoelectric lattice modes.

An interesting result of all the drift velocity experiments was the fact that the observed acoustoelectric interaction for $E_o > E'$ built up in a time of 10 nsec or possibly less, corresponding to a drift length of about one tenth of the normal specimen thickness. (see Section 3.1 for further discussion).

The effect of shallow trapping on the interaction was also investigated. Earlier work on the transport properties of CdS [Spear and Mort (1963)] has shown, that as a result of shallow trapping and release during transit, the drift mobility will begin to deviate markedly from the lattice mobility μ_L at sufficiently low temperatures. Fig.2.8 shows the temperature dependence (according to paper I), of the electron drift mobility μ_d in six CdS specimens. The lattice mobility is denoted by μ_L. As the temperature of the specimens was decreased, a point was reached (marked by an asterisk) where the interaction disappeared. The corresponding values of μ_d and μ_L could be represented reasonably well by the relation $\mu_d = 0{\cdot}37\ \mu_L$. This would imply that for the observation of the transient acoustoelectric interaction the condition

$$\mu_d / \mu_L \geqslant 0.37 \qquad (2.7)$$

has to be satisfied.

In a discussion of possible mechanisms for the above interaction it was pointed out that the amplification theory (White 1962) could not account for the result, even if the effect of the non-linear terms was taken into account. A more complete discussion of the possible mechanisms will be presented in Chapter 3. It was concluded that more information on the generated stress wave was required in order to gain a complete understanding of the transient interaction. In particular it seemed that one may have to look more closely at processes taking place in the region of generation near the top electrode. It was largely for this reason that the present work was undertaken.

CHAPTER 3

Theoretical Considerations

3.1. The Mechanism of the Transient Acoustoelectric Interaction.

In this section a review of the mechanisms discussed in paper I is given. These may be divided into three main groups: the classical macroscopic and microscopic theories and the quantum mechanical theory.

(a) Macroscopic Approach.

In order to explain the observed discontinuities in the (v_d, E_o) graphs (for example, see fig.2.7), a piezoelectric field E_1 associated with the piezoelectric stress wave, acting in the opposite direction to E_o and of sufficient magnitude is required. Figure 2.7 shows that this is only possible if $|E_1| \gtrsim 1$ e.s.u., for applied fields not much greater than E'.

It is important to realise that the White theory discussed in Section 2.1, is a linear small signal theory. It applies to the case where the density of carriers bunched by the piezoelectric field remains small compared to the equilibrium carrier concentration. For the transient acoustoelectric interaction it seemed that the non-linear terms, which were negligible for the cases treated by White, were in fact the dominant ones under the experimental conditions. It was of interest therefore to determine whether the observed interaction might possibly be associated with these terms. In the following analysis based on paper I, an estimate is made of the maximum piezoelectric field possible under favourable conditions. The basic

equations used in this estimate are the piezoelectric equations of state, namely:

$$T = c^{E}S - \theta E, \tag{3.1}$$

$$\text{and} \quad D = 4\pi\theta S + \epsilon^{S}E, \tag{3.2}$$

where T is the stress, S the strain, D the electric displacement and E the electric field within the solid. The constant c^{E} is the elastic stiffness at constant E, θ is the piezoelectric constant, and ϵ^{S} is the permittivity of the medium at constant strain.

If u denotes the particle displacement, then from elementary elastic theory,

$$S = \frac{\partial u}{\partial x} \quad \text{and} \quad \frac{\partial T}{\partial x} = m \frac{\partial^2 u}{\partial t^2}, \tag{3.3}$$

where m is the mass density of the material. The wave equation for a piezoelectric medium is obtained by substituting T from equation (3.1) into equation (3.3), which gives,

$$m \frac{\partial^2 u}{\partial t^2} = \frac{\partial T}{\partial x} = c \frac{\partial^2 u}{\partial x^2} - \theta \frac{\partial E}{\partial x} \tag{3.4}$$

Now, from equations (3.2) and (3.3) we have

$$D = 4\pi\theta \frac{\partial u}{\partial x} + \epsilon E \tag{3.5}$$

From Poisson's equation,

$$4\pi\rho = \frac{\partial D}{\partial x} \tag{3.6}$$

therefore,

$$4\pi\rho = 4\pi\theta \frac{\partial^2 u}{\partial x^2} + \epsilon \frac{\partial E}{\partial x} \quad ,$$

or
$$\epsilon \frac{\partial E}{\partial x} = 4\pi\rho - 4\pi\theta \frac{\partial^2 u}{\partial x^2} \quad ..$$

Substituting this into equation (3.4), gives

$$\frac{\partial^2 u}{\partial t^2} - v_s^2(1 + K^2)\frac{\partial^2 u}{\partial x^2} = - \frac{4\pi\theta}{\epsilon m} \rho \qquad (3.7)$$

as

$$K^2 = \frac{4\pi\theta^2}{\epsilon c} \text{ and } \frac{c}{m} \simeq v_s^2 \quad .$$

For CdS, $K^2 \simeq 0{\cdot}04$. Neglecting this in comparison with unity, equation (3.7) becomes

$$\frac{\partial^2 u}{\partial t^2} - v_s^2 \frac{\partial^2 u}{\partial x^2} = - \frac{v_s^2 K^2}{\theta} \rho. \qquad (3.8)$$

In the presence of a drifting charge distribution we put $E = E_o + E_1$, $u = u_o + u_1$, and the electric displacement $D = D_o + D_1$, to represent the deviations from the equilibrium values. Under experimental conditions $u_1 = 0$ and $\partial u_1/\partial t = 0$ at $t = 0$. On substituting $u = u_o + u_1$ into (3.8) and differentiating the resulting equation with respect to x, we obtain an equation for the extra strain $\partial u_1/\partial x$ produced by the drifting charge. For an infinite crystal the solution satisfying the initial conditions is given by

$$\frac{\partial u_1(x,t)}{\partial x} = \frac{v_s K^2}{2\theta} \int_0^t \left\{\rho(x - v_s t + v_s t', t') - \rho(x + v_s t - v_s t', t')\right\} dt' \qquad (3.9)$$

Hence

$$\left|\frac{\partial u_1(x,t)}{\partial x}\right| \leqslant \frac{K^2 v_s t}{|\theta|} |\rho|_{max} \qquad (3.10)$$

where $|\rho|_{max}$ denotes the largest value of $|\rho(x,t')|$ for all x and for $t' \leqslant t$. To estimate the corresponding electric field E_1, we now use equation (3.5), and substitute $E = E_o + E_1$ etc. This gives (in e.s.u.)

$$\epsilon E_1 = D_1 - 4\pi\theta \frac{\partial u_1}{\partial x} \tag{3.11}$$

From Poisson's equation we find that $\partial D_1/\partial x = 4\pi\rho$. Hence $D_1 = D_1' + D_1''$, where D_1'' is a constant and $|D_1'| \leqslant 4\pi Q$, where $Q = \int |\rho|\, dx$, the integral being taken from x = 0 to x = d, the thickness of the specimen. Now the experimental conditions were such that the sample was practically short circuited to sudden changes of field, so that $\int E_1 dx \simeq 0$. Hence integration of equation (3.11) from x = 0 to d enables us to find the constant D_1'', and we then deduce that

$$|D_1''| \leqslant 4\pi(Q + |\theta|\, |\partial u_1/\partial x|_{max}) \tag{3.12}$$

Combining the preceding results with (3.11) and using (3.10), leads to the desired bound for E_1, namely

$$|E_1| \leqslant \frac{8\pi}{\epsilon}(Q + K^2 v_s t |\rho|_{max}) \tag{3.13}$$

For charges moving with velocity $v_d \sim v_s$, $v_s t \leqslant d$ approximately. Typical values of the constants for the CdS specimens are $\epsilon \sim 9$, $K^2 \simeq 0{\cdot}04$ (Hutson and White 1962), and $d \simeq 0{\cdot}05$ cm. In the experiments the maximum number of generated carriers within the drifting layer was about 2×10^6, spread over an area of 0·1 cm^2. Also $|\rho|_{max} \simeq Q/\delta$, where δ is the thickness of the drifting charge layer. It is assumed that the thickness δ is determined by an essentially uniform generation during the length T_p of the excitation pulse. If

this model is correct, then $\delta = d_p + \mu E T_p \simeq u E T_p$, as the absorption depth d_p is normally smaller than the second term. If we take $\delta = 4 \times 10^{-3}$cm, then equation (3.13) leads to $|E_1| \leq 15$ V.cm^{-1}. Even if $\delta = 4 \times 10^{-4}$cm, we would still only get $|E_1| \leq 60$ V.cm^{-1}, which is too small by at least a factor of 100.

The above analysis shows that even if the non-linear terms in the White theory are retained, it is impossible to account for the observed transient acoustoelectric interaction.

It is possible that E_1 may be generated by some other cause. The following three mechanisms have been considered:

(i) The application of E_o shock excites the crystal. However, in the experiments slow rising field pulses, and in some cases steady fields, were used. In all cases the same strong interaction was observed, and this possibility may therefore be excluded.

(ii) The strongly absorbed incident excitation pulse may generate a stress wave of sufficient magnitude. It was pointed out in paper I that energy and momentum have to be conserved in the generation process. The proposed model which satisfied the conservation laws is shown in fig.3.1 where several of the parameters involved are shown as functions of the distance x from the top electrode at a time immediately after the onset of the excitation. The energy dissipation per micrometre of 35 keV electrons, based on measurements of Ehrenberg and King (1963) are shown in fig.3.1 (a). The initial distribution of generated electron-hole pairs should have a similar

shape. It was assumed that the excitation pulse produced a particle displacement u_1 in the form of a single pulse [fig.3.1 (b)] which results mainly from the interaction of the front of the excitation pulse with the cryatal. Figure 3.1 (c) represents the generated piezoelectric field $E_1 \propto -(\partial u_1/\partial x)$. This follows from equation (3.5) since it can be shown that momentum conservation implies $D_1 \simeq 0$.

From energy considerations it was shown that a piezoelectric field of sufficient magnitude could be produced if the width of the stress wave δ_s were less than one-quarter of the electron range i.e. less than 10^{-4}cm.

Once this field was generated in the region near the top electrode the subsequent interaction could be explained classically by the bunching mechanism illustrated in fig.3.2. The resultant field $E = E_o + E_1$ has been plotted against x for the transit of a cloud of electrons, represented by the shaded region. For $E_o < E'$ [fig.3.2 (a)], $v_d < v_s$ and the stress wave will 'run away' from the space charge layer, so that no interaction can take place between the two. But when $E_o > E'$, as in fig.3.2 (b), the electrons will catch up the wave within a fraction of the transit time and reach a stable bunching region B where they are confined to drift with velocity v_s. As indicated, diffusion forms an escape mechanism.

Results of the present investigation, presented in Chapter 5, show however, that the excitaion pulse cannot by itself produce any appreciable stress wave.

(iii) The relatively dense electron-hole plasma generated by the excitation pulse may be connected with the generation of the stress wave. The maximum charge density in the region of generation leads to a plasma frequency ω_p of about 10^{11} radian sec^{-1}. The electron-phonon relaxation time τ in this region is probably about 10^{-13} sec., and consequently the condition $\omega_p \tau >> 1$, for the build-up of plasma oscillations, is not satisfied. The type of amplification which has been discussed by Carleton and Auer (1965) would not therefore appear to be possible. However, the above plasma frequency lies close to the piezoelectric phonon band which, according to Prohofsky will be strongly coupled to the free carriers, (see Section 2.1.) It is therefore possible that this could lead to a strong local interaction between the electrons and phonons.

(b) Classical Microscopic Approach.

In this approach a charge carrier is first considered separately. Its Coulomb field will set up a piezoelectric stress in the surrounding medium. When the charge drifts with $v_d > v_s$ a shock wave front develops in its rear with its apex at the charge as shown in figure 3.3. This will be the region of maximum strain, and both elastic and electrical energy will flow across the shock wave front. The loss of energy then introduces a retarding force on the charge carrier. Such an approach should be applicable to an insulating solid in which the density of carriers is sufficiently small so that little interaction between shock wave fronts may take place. With increasing charge

density the shock waves will interfere and the effect is then more conveniently described by the macroscopic piezoelectric field.

Tsu (1964) has calculated the energy radiated by a charged particle moving along the c-axis of a hexagonal crystal with a uniform velocity. The power radiated was shown to be proportional to the frequency. This approach could, in principle, explain the experimental results. However, it would be difficult to carry out any quantitative comparisons and this has not been attempted.

(c) Electron-Phonon Interactions.

It is possble that Prohofsky's work (described in Section 2.1) may provide an explanation of the observed acoustoelectric interaction.

However, it would appear that the same problems as those met in the classical theory will arise again. With the small carrier densities involved the stimulated emission of phonons will take a relatively long time to build up a sufficient phonon density to affect the mobility. In order to explain the observed strong interaction within 10 nsec it is again necessary to assume that a high phonon density is generated by some other mechanism,

3.2. Theory of the Metal-semiconductor Contact.

During the course of this work it was decided to illuminate the top of the CdS specimen with highly absorbed light. By this means it was possible to perturb the barrier formed at the gold-CdS boundary, and investigate if it was in any way connected with the generation of

the observed ultrasonic signals. In Chapter 5 the results of such experiments are discussed, and in this section the formation of the barrier, and its behaviour under illumination are considered.

If a semiconductor is placed in contact with a metal, then, in thermal equilibrium, the Fermi levels must be at the same height in the metal and semiconductor. Charge will be transferred until this situation is established, leading to the presence of a dipole layer at the interface. If the work function of the metal ϕ_m is greater than ϕ_s the work function of the semiconductor [fig.3.4 (a)], then the energy levels at contact are as shown in fig.3.4 (b). The condition $\phi_m > \phi_s$ is pertinent to the gold-CdS barrier under discussion.

The depth λ of the potential barrier may be calculated as follows Schottky (1942). Let there be N impurity or defect centres per unit volume in the semiconductor. Then if all these have lost an electron there will be in the surface layer a positive space charge Ne per unit volume. Poisson's equation then gives

$$\frac{d^2V}{dx^2} = -\frac{4\pi Ne}{\epsilon} \qquad (3.15)$$

for $x \ll \lambda$, where ϵ is the dielectric constant. This leads to the following relation, for the thickness λ of the barrier:

$$\lambda = \left[(\phi_m - \phi_s)/2\pi eN \right]^{1/2} \qquad (3.16)$$

Taking $(\phi_m - \phi_s) \lesssim 0{\cdot}7$ volt [Goodman (1964)], and $\epsilon \simeq 9$ [Hutson and White (1962)], then $\lambda \simeq 3 \times 10^{-4}$ cm, for $N \simeq 10^{14}$ cm^{-3}.

The behaviour of additional free charge carriers generated in the barrier by light will now be considered. For the barrier shown in

fig.3.4 (b) the gold electrode becomes the positive terminal by illumination. This corresponds to a voltage in the low resistance direction. If a current is allowed to flow, then the photocurrent corresponds to a current of electrons from the electrode at the barrier layer to the semiconductor.

In the following analysis [Lehovec (1948)] , a general equation is first derived, and then the open circuit voltage is obtained by putting the external resistance equal to infinity. With reference to the experiments described in Chapter 5, it is the open circuit photovoltage that is the relevant quantity. It is assumed that recombination within the barrier layer is negligible.

The thermodynamical potential at the barrier layer which gives rise to a potential difference appearing across the specimen is the sum of an electric potential and a diffusion potential:

$$V_B = V_o + \frac{kT}{e} \log(n_\lambda / n_o) \qquad (3.17)$$

where n_o and n_λ are the densities of free electrons at $x = 0$ and $x = \lambda$ respectively.

The corresponding current (formulated for electrons) will be calculated by means of the following relation:

$$\frac{I}{h\nu} e^{-(x/a)} \frac{\alpha.1}{a} = -\frac{1}{e} \frac{\partial}{\partial x} \left[-ne\mu \frac{\partial V}{\partial x} + eD \frac{\partial n}{\partial x} \right] \qquad (3.18)$$

In this relation, I is the intensity of the light when entering the semiconductor, α is the number of electrons released by one light

quantum and a is the absorption depth.

The left side of equation (3.18) represents the number of free electrons released by the absorbed light quanta in a unit volume at a distance x from the electrode.

In the brackets on the right hand side there is the total current carried by electrons, made up of a drift and a diffusion term. The electron current is dependent on space. The independence on space of the total current is guaranteed by an additional current of positive charges released by the light. For these positive charges an equation very similar to (3.18) may be written. The boundary conditions for (3.18) are the densities of electrons for $x = 0$ and $x = \lambda$ and the electron current at $x = \lambda$ which is equal to the total current through the bulk semiconductor.

The first integral of equation (3.18) is:

$$I/h\nu.\alpha.\left[e^{(-x/a)} - e^{(-\lambda/a)} \right] = -n\mu\, \partial V/\partial x + D\,\partial n/\partial x - i/e \qquad (3.19)$$

where i is the photo-current through the barrier layer. The integration constant has been expressed by the values at $x = \lambda$. This is a linear differential equation of the first order in n; its integral has the general form

$$n = \left[\text{const.} + Z \right] \exp\left(\frac{Ve}{kT}\right) \qquad (3.20)$$

where the relation $\frac{kT}{e} = \frac{D}{\mu}$ and the abbreviation

$$Z = I/h\nu.\alpha/D \int_0^x \left\{ \exp(-x/a) - \exp(\lambda/a) + \frac{i.h.\nu}{I.e.\alpha} \right\} \exp(-Ve/kT)\,dx$$

have been used.

According to the boundary conditions we have

$$\text{const.} = n_o \exp(-V_o e/kT)$$

$$\text{and } n_\lambda = n_o \exp(-V_o e/kT) + Z_\lambda$$

Appreciable contributions to the integral of Z arise only from the lowest values of the voltage V (which is negative); for $V_o \ll -K_1 T$, we may therefore, use the approximation

$$V \simeq V_o + Ex + \ldots. \tag{3.21}$$

where E is the field intensity at x = 0, and extend the limits of the integral from 0 to ∞.

Then we get

$$Z_d = \frac{I\alpha kT}{h\nu DEe} \exp\left(\frac{-V_o e}{kT}\right) \left\{ \left(1 + \frac{kT}{Eae}\right)^{-1} - \exp\left(-\frac{\lambda}{a}\right) + \frac{ih\nu}{Ie\alpha} \right\} \tag{3.22}$$

Using the connection between n_λ and Z_λ mentioned above, we have with regard to equation (3.17):

$$\frac{Ie\alpha}{h\nu}\left[\left(1 + \frac{kT}{Eae}\right)^{-1} - \exp\left(-\frac{\lambda}{a}\right)\right] + i = n_o e\mu E \left[\exp\left(\frac{V_B e}{kT}\right) - 1\right] \tag{3.23}$$

This equation may be split up into the following two equations:

$$(Ie/h\nu)\alpha A + i = n_o e\mu E \left[\exp\left(\frac{V_B e}{kT}\right) - 1\right] \tag{3.24}$$

$$\text{and} \quad A = \left[1 + \frac{kT}{Eae}\right]^{-1} - \exp\left(-\frac{\lambda}{a}\right) \tag{3.25}$$

The factor A is closely related to the quantum yield. The value A = 1 would be reached if (a) all light quanta were absorbed within the barrier layer, and (b) all generated electrons were carried by the electric field toward the semiconductor. In the experiments (see Chapter 5) only highly absorbed light was used, hence condition (a) is

satisfied. In addition, condition (b) holds approximately, because of the high field which is known to exist at the gold-CdS contact.

The open circuit photo-voltage condition corresponds to the resistance R of the external circuit being equal to infinity. Under these conditions

$$i = 0 \tag{3.26}$$

Substituting equation (3.26) into equation (3.24) we have, with A = 1;

$$(Ie/h\nu)\alpha = n_o e\mu E \left[\exp\left(\frac{V_B}{kT/e}\right) - 1 \right]$$

and therefore,

$$V_B = \frac{kT}{e} \log \left[\frac{I\alpha}{n_o E h\nu \mu} + 1 \right] \tag{3.27}$$

This relation has been applied in the interpretation of the experiments described in Chapter 5.

CHAPTER 4

Experimental Method

4.1 Introduction.

A technique has been developed which permits the simultaneous observation of the transit of the generated layer of charge carriers and the associated piezoelectric stress wave.

The first part of this chapter considers the fast pulse techniques for the study of charge transport in solids, [e.g. Spear (1960), Spear and Mort (1963)] and then an account is given of the apparatus used to detect the stress wave.

The fast pulse techniques have been developed in this laboratory during the last eight years. A block diagram of the apparatus is shown in fig.4.1. In a drift mobility experiment the specimen S is prepared in the form of a platelet of known thickness d, and electrodes are evaporated onto the main faces T (top) and B (bottom). A very short excitation pulse of electrons is focussed onto one side of the specimen. This is absorbed within a few microns and generates free electron-hole pairs. The application of an electric field E_o draws carriers of one sign out of the excited region. The transit time t_t is obtained by charge integration measurements. This will lead to the drift velocity v_d and the drift mobility μ_d from the equations,

$$v_d = \frac{d}{t_t} \quad \text{and} \quad \mu_d = \frac{v_d}{E_o} \tag{4.1}$$

4.2 Electron Pulse Excitation.

The electron gun and the associated fast pulse techniques have been described in detail previously, [Spear (1960) and Spear, Lanyon and Mort (1962)] , and only a brief description will be given here.

As shown in fig.4.1 a tetrode electron gun with a directly heated tungsten filament was used. Sliding 'O' ring seals were incorporated into the filament assembly which made horizontal and vertical adjustment possible under running conditions. The electron gun and its associated components were raised to a negative potential of about 35 kV and the second anode A_2 held at earth potential.

The gun was biased off by the potential V_B ($\sim$22 volts) applied between the cathode and the gun housing. A fast rising positive voltage pulse was applied from the mercury wetted contact relay M to the 75 ohm terminating resistor between the grid and the gun housing, to switch the gun on for the duration of the pulse. The connecting line CL between the relay and the grid was terminated inside the gun housing to provide a good match. The length of the excitation pulse could be varied between 2 nsec and 300 nsec by switching in different lengths of delay line DL, by means of the coaxial switch CS*; typical pulse lengths ranged from 2 - 10 nsec for the drift velocity experiments. The beam current was controlled by the charging potential applied to the delay line.

The relay was triggered by a generator to which it was optically

* Supplied by Hatfield Instruments Ltd.

coupled by a GaAs lamp GL. The generator could be run at single shot, at 50 c.p.s. (either phase) or 100 c.p.s. The phase of the trigger pulse could be shifted by a phase shift network in the generator.

The first anode, held at a fixed voltage V_{A1} of 300 volts with respect to the negative accelerating potential, ensured that the beam current was largely independent of the accelerating potential. The beam was focussed onto the specimen by the magnetic lens L.

The specimen holder (described in Section 4.7) contained a small Faraday cup for collecting and measuring the incident beam. By turning a switch, (not shown in fig.4.1) a steady potential could be applied to the biasing circuit to give a steady beam current equal to that used during pulsed operation. This was measured and multiplied by the excitation pulse length to give the number of incident electrons per pulse.

4.3 Light Flash Excitation.

It appeared of interest to compare some of the results obtained with electron excitation with those obtained with photo-excitation. For this a fast rising, intense light flash is necessary. From the point of view of intensity some form of spark discharge is adequate, but this introduces two major difficulties. First, the electrical interference caused by a high voltage discharge is generally such as to paralyse any sensitive electronic equipment in the same room. The provision of adequate screening is a problem. Secondly, the decay of

the light output is generally much slower than its rise-time.

The first problem was solved reasonably well by a triggered spark gap built as a completely coaxial and constant impedance system as described for example, by Fletcher (1949)*. The complete unit is shown in fig.4.2 and produced a pulse of about 100 nsec duration. The E.H.T. supply to the spark gap S was provided by a Brandenburg 20 kV generator. The Kerr cell K was intended to achieve a rapid decay time of the light output. Unfortunately, it only transmitted about 10% of the incident light, so the experiments were carried out without the Kerr cell. The resulting longer decay time ($\sim$50 nsec) did not fundamentally affect the stress wave measurements. The light pulse was focussed through two lenses L, whilst a filter F selected highly absorbed light.

Most results have, however, been obtained by means of electron excitation, where the advantages over photo-excitation are the ease with which the pulse length and intensity may be varied. It is also possible to vary, within certain limits, the depth of penetration of the beam into the specimen by adjustment of the accelerating potential.

4.4 Field Pulse Unit.

It has been found in drift velocity and stress wave measurements that the magnitude of any space charge resulting from the trapping of

* The spark gap used was designed and constructed by Dr. L.S.Miller of this department.

injected carriers may be considerably reduced by pulsing the applied field.

The field pulses were derived by switching the potential from a battery box by means of a mercury wetted contact relay, (Elliott EBSC 65015). The relay was driven from the 50 c.p.s. ac mains through the phase shift network P as shown in fig.4.3. The 30 k.ohm potentiometer in series with the coil allowed a variation of the pulse length from 2 - 6 msec. The normal repetition rate was 50 p.p.s., but a few pulses at a time could be obtained by having switch S_4 open and closing the microswitch S_5.

The voltage source V was built up from 9, 90 and 300 volt batteries to give 0 to 1200 volts in 1·5 volt steps. The switch S_1 was used to obtain either positive or negative potentials, and switch S_2 to give a steady field when required.

The relay used was of the break-before-make type and no current limiting resistors were therefore necessary. The 1 k.ohm resistor was provided to damp out oscillations on the leading edge of the field pulse; it also had the effect of reducing the rise-time of the pulse to about 100 nsec. For the stress wave measurements a much slower field pulse was used; a typical 5 msec pulse had a rise and decay time of 1 msec. This slower pulse was produced by loading the output with suitable condensers. Such slow pulses eliminated the possibility of producing spurious stress waves within the CdS crystal due to shock excitation.

The phase of the field pulse was adjusted so that the excitation pulse occurred approximately in the centre of the field pulse.

4.5 Determination of the Transit Time.

For the measurement of transit times, a charge integration method was employed, the principle of which is illustrated in fig.4.4. The excitation pulse, absorbed in a depth $d_p \ll d$, generates N_g electron-hole pairs close to the top electrode T. Due to the rapid recombination that will occur in this region only a number Q of one type will be drawn into the bulk of the specimen under the action of the applied field. These will induce a charge on the bottom electrode B proportional both to their number and the distance moved. The integrated charge q (t) at a time t will give rise to a potential difference ΔV (t) across the resistance R, this is given by,

$$\Delta V(t) = \frac{Q_{ex}(t)}{Cd} = \frac{Q e \mu_d E_o t}{Cd} \qquad (4.2)$$

It is assumed that the value of RC is much greater than the time during which the drift takes place and that no carriers are lost during transit.

The value of ΔV (t) expected under ideal conditions is shown in fig.4.5 (a). The linear increase in ΔV terminates sharply at $t = t_t$. By measuring the transit time at various fields the drift mobility is obtained from the gradient of a graph of $\frac{1}{t_t}$ against E_o using equation (4.1).

From equation (4.2) it is seen that the potential difference across R is inversely proportional to the total capacity C across R. To reduce this capacity to a minimum a cathode follower was used before the signal was amplified. The circuit of the cathode follower is given in fig.4.6 and that of the wideband preamplifier in fig.4.7. The switching transients associated with the use of a pulsed field would normally paralyse the detection equipment. To overcome this difficulty, pairs of diodes were wired back to back and fitted as grid leaks to bypass these large transients. This arrangement was tested and was found to amplify linearly for outputs up to about 150 mV, twice as large as those typically used in the experiments. The 1·8 pF. condenser at the cathode follower input was provided for charge sensitivity calibration.

The total voltage gain of the cathode follower and preamplifier was fifteen and the total rise-time eight nsec. The signals were displayed on a Tektronix 581 oscilloscope fitted with a type 86 plug-in unit. The maximum charge sensitivity of the system was such that a vertical deflection of 1 cm on the oscilloscope corresponded to the transit of about 2.10^5 electrons.

The following conditions have to be satisfied in order to observe a well defined transit of carriers.

(a) The drift of the generated carriers across the specimen is a perturbation from space charge neutrality. If this is not to be neutralised, the relaxation time of the crystal must be longer than

the transit time. This is satisfied by the low conductivity specimens used in these experiments.

(b) The transit time must be longer than the rise-time of the measuring equipment.

(c) The thickness of the drifting sheet of charge should be much less than the specimen thickness. This can be satisfied by making the excitation pulse duration much shorter than t_t and by ensuring that the depth of penetration of the excitation pulse is much less than d.

(d) Above a certain carrier density the space charge effects of the moving carriers become important and modify the field distribution. Experience has shown that to avoid this effect it is necessary to limit the number of carriers in the excitation pulse to about 10^5 electrons, corresponding experimentally to less than 10^7 electrons drifting across the specimen.

(e) The carrier lifetime with respect to deep traps must be greater than t_t. If this is not so there will be a loss of carriers (to deep traps) during the transit. These trapped charges will alter the field distribution and may affect it appreciably if present in sufficient quantity.

In addition to the above conditions there will always be some broadening of the charge cloud due to diffusion and the statistical nature of shallow trapping, which may make the transit too diffuse for accurate measurements.

If the transit time is of the order of the lifetime τ with

respect to a spatially uniform distribution of deep traps, then the charge integration observed will be of the shape shown in fig.4.5 (b). If t' is defined by the intersection of the tangents at $t = 0$ and $t \gg t_t$ then Spear and Mort (1963) have shown that,

$$\frac{1}{t'} = \frac{1}{\tau}\left[1 - \exp\left(\frac{-t_t}{\tau}\right)\right]^{-1} \qquad (4.3)$$

The value of t' extrapolated to zero applied field will give τ. Over the range of E_o generally used, the mobility obtained from the gradient of a graph of $\frac{1}{t'}$ against E_o is only a few percent different from that obtained by plotting $\frac{1}{t_t}$ against E_o, [t_t obtained from equation (4.3)]. At a given value of E_o, however, equation (4.3) must be used to obtain the true drift velocity $\frac{d}{t_t}$ from the measured quantity $\frac{d}{t'}$.

In order to monitor space charge effects in the crystals during transit measurements, the excitation pulse was triggered at 100 p.p.s. and field pulse at 50 p.p.s. The 'discharge' pulse, observed during the period when the field was off, gave an indication of the magnitude of the space charge field present. Whenever possible the height of the excitation pulse was reduced until this discharge pulse was not detectable.

4.6 Current Pulse Height Measurements.

For these measurements the resistance R (fig.4.4) was decreased to 200 ohms giving a rise-time less than 10 nsec. The current pulse

was amplified, using two Hewlett Packard Wideband Amplifiers (Model 460 AR) in series, and displayed on an oscilloscope. The overall voltage gain of this system was about 100.

The actual pulse height I_p was recorded as a function of field for a given incident excitation intensity. The excitation pulse length was increased, generally to 300 nsec. As the transit time was less than this value for the majority of applied fields, the cloud of drifting charges extended throughout the specimen for most of this time. The observed current pulse is shown in fig.4.5 (c).

4.7 Ultrasonic Detection Apparatus.

(i) Basic Specimen Holder.

The most recent version of the specimen holder used in ultrasonic measurements of up to 50 Mc/s is shown in fig.4.8.

The specimen S was attached to a short ($\frac{3}{4}$") fused silica buffer rod B, $\frac{1}{2}$" in diameter, the latter being held in position by a clamping arrangement C. The upper and lower faces of the buffer and the lower part of its side were Al. plated. The lower face was connected to the earthed base plate BP via the clamp in contact with the buffer side. The quartz transducer T was held between the buffer and a thin brass disc D which rested on a slightly compressed rubber disc R. D was connected through a glass-metal seal to a socket on the lower side of the base plate, which provided the output terminal from the detecting transducer.

Fine wires were connected to the CdS specimen S with silver paste. Wires from S and F were attached to glass-metal seals such as G1, which were in turn connected to sockets mounted on the lower face of BP.

The incident electrons could be focussed through the aperture A or, if the incident pulse itself was to be measured or observed, onto the Faraday cup F. Excitation pulses of 2 - 300 nsec duration were used in the ultrasonic measurements.

The base plate was clamped underneath the electron bombardment gear against a neoprene 'O' ring seal, and the complete specimen housing above BP was evacuated to a pressure of less than 10^{-4} torr.

With this apparatus both longitudinal and shear wave interactions could be investigated. It was found convenient for measurements at room temperature, to bond acoustically both longitudinal and shear wave CdS specimens to the top of the buffer with silver paste (Johnson Mathey Grade FSP 36). For measurements of longitudinal stress waves, using an X - cut quartz transducer, it was sufficient to apply a thin film of silicone oil to the transducer for bonding. For shear wave measurements, however, it was essential to bond the Y - cut quartz transducer to the buffer with silver paste, which sets hard and was found to yield a good bond for frequencies up to 50 Mc/s.

The purpose of the buffer is threefold. It electrically isolates the CdS specimen from the transducer, and also introduces a known delay which makes it possible to observe the ultrasonic signal in absence of any pick-up signals that might be caused by the excitation

pulse. Finally, from the velocity for ultrasound in the buffer, the delays of the direct signal and subsequent reflected signals are accurately known. Such information is important when identifying the various signals observed on an oscilloscope.

(ii) Coaxial Holder.

For ultrasonic measurements concerned with frequencies greater than about 50 Mc/s a special coaxial holder was constructed. Here, the buffer and transducer were mounted within a coaxial socket. The advantage of this design lies in the fact that no serious electrical discontinuities are introduced, and also that the matching element can be connected directly to this socket, very near to the transducer.

A cross-section of this holder is shown in fig.4.9. A socket SO (General Radio Type 874-BBL), was attached to the base plate BP. One side of the quartz transducer T was connected to the inner conductor I of the socket via the brass disc BD. The insulating disc ID held I central with respect to the external conductor E. The base plate was fitted with a special brass bush BB in which was formed a series of springy fingers F. As before the upper and lower faces of the buffer and lower part of its side were Al plated. The fingers F in contact with the Al formed the earth return to E, the external conductor. The other end of the buffer carried the specimen S. An 'O' ring between B, BB and the clamping arrangement C completed the vacuum seal. This holder was also used for measurements with CdS thin film transducers.*

* The CdS thin films were prepared by Mr. A. Vecht of A.E.I. Rugby.

In this case the lower face of the buffer and part of its side were covered with a thin film of nesa, a transparent highly degenerate semiconductor. The CdS thin film was evaporated onto the nesa. This film was then furnished with a gold electrode. The fingers F made contact with the nesa, whilst contact between the gold electrode and BD was made using crushed Al foil, thereby eliminating the possibilty of damage to the fragile thin film transducer.

This holder had the advantage that the buffer, with its associated thin film transducer may be plugged in and removed with comparative ease.

(iii) Specimen Holder for Low Temperature Measurements.

This holder was a modified version of that discussed under 4.7 (i). The transducer enclosure was identical. The additional parts are indicated in fig.4.10. A sheet of copper foil CF was sandwiched between the specimen S and the buffer B. A copper pipe P, encircling B was placed near CF. Nonaq Stopcock grease was used as the bonding material, a thin film of which was placed between S and CF, and CF and B. This bond was certainly well behaved down to about -140°C. Good thermal contact between CF and the pipe P was ensured by using some thermally conducting grease, although, CF and P were electrically isolated by a thin sheet of melinex M. The Chromel-Alumel thermocouple leads TC, used to measure the temperature of the specimen, were passed through a seal in the base plate. The junction of TC was kept in place

by a small drop of low temperature varnish. The ends of the copper pipe were led out through the base plate via a thin walled stainless steel tube thereby thermally isolating the copper tubes from the brass base plate. Temperatures in the range 20°C to about -130°C could be maintained reasonably constant by varying the rate at which liquid nitrogen was introduced into the pipe.

4.8 Associated Electronic Equipment.

For measurements of the stress wave at frequencies up to about 50 Mc/s, a tuned preamplifier with variable bandwidth was used, the circuit of which is shown in fig.4.11. Various coils were wound for this amplifier and by means of switches S2 and S3 a given coil could be selected. Coils giving frequencies of about 3,4,10,19,22 and 45 Mc/s were used with this amplifier. By means of switches S1 and S4 the bandwidth of the amplifier could be varied within the limits 0·5 Mc/s to 2 Mc/s for any one of the given centre frequencies.The transducer output was connected directly to the input of the amplifier. In general the output from the amplifier was fed into an oscilloscope, the gain of the amplifier being about 500 or greater. On some occasions further gain was achieved with a Hewlett Packard Wideband Amplifier Type 461A placed between the tuned amplifier and the oscilloscope.

Measurements above about 50 Mc/s were made using the apparatus shown in fig.4.12. An impedance matching unit MU, in the form of a triple-stub tuner was connected between the transducer T and a crystal

mixer M (General Radio Type 874-MR). In M, mixing of the signals from T with the signal from the local oscillator LO, produced signals at an intermediate frequency of 30 Mc/s. These were amplified by a low-noise intermediate frequency amplifier IF (Decca Type 30/15 P) having a gain of 48 db, and were displayed on an oscilloscope O. The bandwidth of this amplifier was 18 Mc/s thus enabling the observation of very short signals. The circuit of this amplifier is shown in fig. 4.13. This set up was suitable for frequencies in the range 50 Mc/s to 5 Gc/s and could detect signals down to about 10μV.

An important part of this equipment is the matching unit which is shown in fig.4.14. This consisted of three, 50 cm adjustable stubs S, each being a coaxial line with a sliding short circuit of the multiple-spring-finger type. The three stubs were connected to three tee junctions T, which were in turn connected to two rigid 10 cm coaxial lines L.

To tune the above unit a test frequency was used. If, for example a signal of about 100 Mc/s was to be detected, using a transducer with a resonant frequency of about 100 Mc/s, a test signal of this frequency was applied to the CdS crystal on the top of the buffer rod. Using the equipment shown in fig.4.12, this signal was displayed on an oscilloscope. However, in general a signal having maximum amplitude was not obtained, for the transducer may not be in exact resonance and optimum matching conditions may not exist. The three stub positions were then adjusted until the signal was at a maximum. The process was

then repeated for other frequencies close to 100 Mc/s. The largest maxima then corresponded to the exact resonance of the receiving transducer, and at this point maximum sensitivity of the entire receiving system prevailed.

The theory of stub matching is considered in Appendix I.

4.9 Specimens and Their Preparation.

In the present investigations both platelet crystals and larger boule crystals of CdS were used. The former were obtained from four sources: A.E.I. at Harlow, E.M.I. at Hayes, Dr. Wright of Birmingham University, and from Dr. Müller of the Deutsche Akademie der Wissenschaften, Berlin. All the crystals used were 'pure' in the sense that no impurities were deliberately added during growth. The main faces of these platelets were usually about ten square millimetres in area. In the majority of the crystals the c-axis was contained in the platelet face. The thickness of the crystals ranged from about 100 to 500 μm.

The larger boule crystals were obtained from the Eagle Picher Company and the Harshaw Company. Some of these boules were already orientated, while from others trial slices were cut and orientated using highly convergent polarised light. Further slices were then cut as basal sections, or with the c-axis contained in the main face. The crystals were cut into platelet form on a crystal saw by diamond paste embedded in a thin nylon line.

The crystal thickness d lay in the range from 100 to 200 μm. The limits imposed on d arise from the shortest transit time that may be measured and the lifetime of the electrons (with respect to deep traps) respectively.

The faces of these slices were ground flat and parallel with successively finer grades of diamond paste.

In order to determine the drift velocity and mobility of the carriers it is necessary to know accurately the specimen thickness. This was measured by means of a miniature optical lever gauge having a magnification of about 10^3, [Spear, Adams and Henderson, (1963)]. Its advantages are that there is little chance of damaging the often fragile specimens and that it is possible to probe the specimen thickness. Only areas of uniform thickness were used for the experiments.

Metal electrodes were evaporated onto opposite faces of the crystal at pressures below 5.10^{-5} torr. The bottom electrode (i.e. the electrode furthest from the excitation pulse) was generally of indium, and the top electrode of gold.

Several thicker specimens were used in a probe experiment. Specimens up to 600 μm thick had electrodes evaporated on their opposite faces as before. In addition a thin 60 μm strip of In was evaporated onto one of the sides of the specimen and parallel to its faces. The strip was positioned midway between the two faces.

CHAPTER 5

Experimental Results

5.1 Introduction.

In the previous work, reported in paper I, the interaction of the electrons with the phonons was evident from drift velocity measurements. Even more important was the fact that the interaction built up within a very short distance below the top electrode.

Results presented here are concerned with the generated stress wave. In particular the stress wave has been studied whilst the region where the wave is believed to originate has been probed, both by the electron beam and by highly absorbed light.

5.2 Drift Velocity Measurements at Room Temperature and their Correlation with the Generated Stress Wave.

In the initial part of the work some drift velocity measurements were repeated, and these showed substantial agreement with those reported in paper I. A typical drift velocity curve for a shear wave specimen is shown in fig.5.1 (a), where the drift velocity v_d is plotted against E_o. This curve has the same form as that shown in fig.2.7. The abrupt discontinuity is observed at a drift velocity v_d'. In all cases v_d' agreed well with the appropriate sound velocity v_s. In fig.5.1 (b) the stress wave amplitude is plotted as a function of E_o for the same specimen. The signal was detected at a frequency of 10 Mc/s, the electron excitation energy was 34 keV and the excitation pulse

length was 100 nsec. The significant result is the fact that the extrapolated onset of the generated stress wave coincides closely with the condition $E_o = E'$.

The majority of the measurements on the generated stress wave were made on slices cut from boule crystals, the c-axis being perpendicular to the face of the slice. Unfortunately the electron lifetime in these samples with respect to shallow traps was usually too short to make any accurate drift mobility measurements. For these specimens current pulse height measurements were made. A plot of the current pulse height I_p against field E_o is shown in fig.5.2 (a). The discontinuity is again observable at the critical field E'. The ultrasonic output for the longitudinal interaction is plotted in fig.5.2 (b) , the characteristics being the same as for fig.5.1 (b). In these measurements an excitation pulse of 35 keV electrons and 60 nsec duration was used. The incident electron beam current for the current pulse height measurement was 3μA, while for the stress wave amplitude measurement this current was increased to 10μA.

Curves similar to those in fig.5.2 (a) and (b) have been obtained using optical excitation instead of the electron beam. Intense light flashes of about 100 nsec duration were produced by the pressurised spark gap described in Chapter 4. A suitable filter selected a highly absorbed spectral region near 480 mμ.

An example of one of the observed ultrasonic signals (19 Mc/s) is shown in fig.5.3 (a). The photograph shows six groups of pulses. In the

first group, five individual pulses are evident, these are labelled a, b,c,d and e. Fig.5.3 (b) shows these pulses in greater detail. The risetime of an individual pulse may be correlated with the bandwidth of the detection apparatus used. Thus, for the signals at 19 Mc/s shown in fig.5.3, the bandwidth of the receiver was about 2.5 Mc/s. The corresponding risetime is about 160 nsec which is in reasonable agreement with the observed pulse risetime. The repetition of the groups of signals at intervals of about 6 μsec was caused by the reflection of the stress wave at the ends of the buffer rod. Within a given group however, the pulse repetition time is 0·8 μsec. This time appears to be related to the two-way transit time of the ultrasonic pulse within the brass disc supporting the quartz transducer at the lower end of the buffer (see fig.4.8). In the experiments the amplitude A of the first pulse was measured in terms of the voltage of the signal observed on the oscilloscope screen. For these photographs the field E_o was 8·9 kV cm^{-1}, whilst the incident electron energy was 35 keV and the duration of the excitation pulse was 30 nsec. The form of these signals was found to be independent of the duration of the excitation pulse in the range used (2-300 nsec).

It is important to realise that the above signals are only observed in the presence of:

(a) A drift field $E_o > E'$.

(b) An excitation pulse.

For all specimens investigated no signal was observed with just (a) or (b)

The relation between the ultrasonic amplitude A and the applied field E_o for different values of the beam current i_b is shown in fig.5.4. The measurements were made at 19 Mc/s using a 30 nsec excitation pulse length, whilst the electron excitation energy was 34 keV. The general feature of these curves is the linear relation between A and E_o for $E_o \lesssim 3{\cdot}5E'$ and the saturation which occurs at about 6E'. Using the same values of the beam currents and fields, the charge Q drifting across the specimen was also determined. These results are shown in fig.5.5.

In addition to the above results, the A vs. Q dependence for $E_o \simeq 3{\cdot}5E'$ was investigated. The relation was found to be a linear one as shown in fig.5.6.

The depenence of A on i_b, E_o and Q will be discussed in Chapter 6.

5.3 The Dependence of the Stress Wave Amplitude on the Energy and Duration of the Excitation Pulse.

It was possible to vary the depth of penetration of the incident electrons within the range of 0·5 to 3·5 μm. This range corresponds to incident electrons having energies V_p from 5 to 40 keV. The dependence of A/Q on V_p is shown in fig.5.7, where the depth d_p below the surface of the half-width of the distribution is also indicated. Here, Q is held constant by adjustment of the beam current i_b, and curves are shown for three different applied fields. The energy-depth relation has been derived from the work of Ehrenberg and King (1963), and will be considered in more detail in the following chapter.

The effect of the duration of the electron excitation pulse T_p over the range 2 to 150 nsec was also investigated. Once again Q was held constant. Results for one of the specimens investigated are shown in fig.5.8 for six frequencies. These curves show $(A/Q)/(A/Q)_{max}$ as a function of T_p. For these curves $E_o = 9{\cdot}2$ kV cm^{-1} and $V_p = 35$ keV.

An interesting feature of these curves is the plateau at smaller T_p, which decreases in extent as the frequency increases. On each of the six curves in the figure a point half-way between the maximum and the observable minimum of $(A/Q)/(A/Q)_{max}$ has been denoted by T_p'. A graph of T_p' against the inverse of the frequency ν is shown in fig.5.9. The straight line obtained has a slope of approximately one half, and thus $T_p' \simeq \nu/2$. The implication of this result will be discussed in Chapter 6.

From the same set of results it is also possible to plot $\mathcal{E}(k)/Q$ as a function of ν, as shown in fig.5.10. Results for a second specimen of different thickness, are also included. The quantity $\mathcal{E}(k)$ is related to A through an expression [equation(6.11)] to be derived in Section 6.2, and represents the amplitude associated with a particular frequency component of the generated stress wave. With this information it has been possible to estimate the piezoelectric field associated with these low frequency components of the generated stress wave (Section 6.2.). The peak at about 30 Mc/s in fig.5.10 is probably associated with a fundamental resonance within the acoustic detection system. The fundamental frequency of the transducer used in these experiments was

about 75 Mc/s, and is therefore about twice the frequency corresponding to the peak.

5.4 The Effect of Monochromatic Illumination on the Gold-CdS Contact.

The work described in paper I showed that the transient acoustoelectric interaction built up in a time of 10 nsec or less. The region of interest therefore within the crystal is a thin layer just below the top electrode which includes the barrier region discussed in Chapter 3. It was decided to modulate this barrier using highly absorbed monochromatic illumination to determine the effect, if any, on the generation of the ultrasonic wave.

Under this illumination both the ultrasonic amplitude and the number of drifting charges were found to decrease. However, when the number of drifting charges was increased to its original value by increasing the incident electron beam current, the ultrasonic amplitude was found to be lower than its value in the absence of illumination.

A Kodak Wratten Filter (No.45) was used to give monochromatic illumination centred on 480 mμ. The maximum penetration depth for light in the band used (450 to 520 mμ) was about 1·5 μm, and has been calculated from optical absorption data by Cardona and Harbeke (1965). The intensity could be varied by the use of Wratten Neutral Density Filters. For an average intensity used, about 10^{10} photons were incident on the top electrode.

The decrease in the stress wave amplitude A for increasing light

intensity I is shown for two of the specimens investigated in fig.5.11 (a) Q being kept constant throughout the range. In a second experiment, using the same values of I the change in barrier height V_B was recorded using a high input impedance vibrating reed electrometer placed across the crystal. The change in barrier height as a function of the light intensity is shown for the same specimens in fig.5.11 (b), and amounts to about 0·5 V. If V_B is plotted against log I, then the relation is linear, as expected from equation (3.27). In a further experiment the bulk conductivity of the specimens was monitored. The specimen conductivity did not increase by more than an order of magnitude over the range of intensities,used, and therefore the normal macroscopic White type amplification mechanism (Section 2.1) may still be excluded.

5.5 Temperature Dependence of the Ultrasonic Output.

An important result of previous work on the transient acoustoelectric effect in CdS (reported in paper I), was that the electrons no longer interacted appreciably when $\mu_d \lesssim 0{\cdot}37\mu_L$. This relation was deduced from drift mobility measurements made at different temperatures. It was equally important to see if the production of a stress wave became less efficient when $\mu_d \lesssim 0{\cdot}37\mu_L$.

In these experiments the crystal was slowly cooled using the temperature holder described in Section 4.7 (*iii*), and the temperature at which the discontinuity in the pulsed current-field curves disappeared was recorded. At the same time the stress wave amplitude was recorded.

The temperature dependence of the stress wave amplitude for one of the specimens investigated is shown in fig.5.12. The temperature T', at which the discontinuity disappeared is indicated by the dotted line. At this temperature, the relation between μ_d and μ_L was found to be in agreement with equation (2.7). The stress wave amplitude is seen to decrease with decreasing temperature until the temperature T' is reached, and remains essentially constant for temperatures less than T'. The effect of changing temperature on the acoustic bonds was monitored by means of a constant amplitude test signal, which was applied to the CdS crystal at regular intervals during the cooling. In fig.5.12 the readings have been corrected for varying bond efficiency.

The above results will be discussed in Section 6.9.

5.6 Experiments on CdS Thin Film Transducers.

During the present investigation several attempts were made to study the ultrasonic output in the 100 to 500 Mc/s range. In this frequency range it is impossible to produce half-wavelength quartz transducers, so for this purpose some CdS thin film transducers were made. This type of transducer was recently developed by Foster (1964).

In these experiments three thin film transducers were tried. The films* were evaporated in a conventional evaporation apparatus. CdS platelets were used as the charge in the evaporation source. The nesa

*We are most indebted to Mr. A.Vecht of A.E.I. Rugby, for the preparation of these specimens.

covered silica substrate was heated to about 200°C.

Recrystallisation of one of the films was achieved by heating the film in a controlled atmosphere. For the other two films, powdered Cu_2S was added prior to heating in a controlled atmosphere. Complete details of the films are given in Table I.

Thin film transducers are essentially broad-band devices, thus a 500 Mc/s transducer may have a bandwidth of 70 Mc/s. By applying a test signal to the CdS specimen (fig.4.9), it was found that all three films exhibited transducer action. However, film No.1 appeared to be the most efficient. Unfortunately, signals corresponding to those shown in fig.5.3 were never observed in the 100 to 500 Mc/s range.

In addition to the above experiments one attempt was made to detect ultrasonic signals in our high resistivity specimens at 9 Gc/s In this experiment the CdS crystal was placed in a tuneable reentrant microwave cavity, however, no signal was observed. It is interesting to note that Haydl and Quate (1965) have observed microwave emission from n-type CdS with a resistivity of 1·45 ohm cm, over the frequency range 2 to 4 Gc/s.

5.7 Probe Measurements.

In the course of this work it was thought that more information could be obtained on the nature of the stress wave by studying its transit across the CdS specimens. For this purpose an In probe strip was evaporated on the side of one of the thicker specimens. It was

hoped that the passage of the electric field associated with the stress wave would be detected by the probe. After amplification, the probe output was displayed on an oscilloscope. The only pulse observed was that expected from the drifting electrons. It resembled the current pulse seen at the bottom electrode, but was of less definite shape. The field associated with the drifting layer of electrons would be of the order of 1 to 2 e.s.u. cm^{-1}. In view of this high field it is difficult to understand why no signal other than that expected from the drifting electrons was observed.

CHAPTER 6

Discussion and Conclusions.

6.1 Introduction.

In this chapter the experimental results and their interpretation will be discussed. A model for the transient acoustoelectric interaction will then be given.

The experimental results presented in the previous chapter yield much information regarding the generated stress wave. However, in interpreting the results it is important to bear in mind the relation between the generated stress wave and the observed ultrasonic wave.

In its simplest form the generated stress wave takes the form of a short pulse as shown in fig.3.1. It is reasonable to assume that the half-width of this pulse is essentially the same as the penetration depth, i.e. a few microns (see fig.6.6). The particle displacement u_1 gives rise to a piezoelectric field $E_1 \propto - du_1/dx$ [see fig.3.1 (c)] as described in Section 3.1 (a) subsection (*ii*). The piezoelectric wave may be analysed into its Fourier components. The frequency of the fundamental would be expected to be about $v_s/2\delta_s \simeq 10^9$ c.p.s. Under our experimental conditions we could obtain information on the long wave Fourier components at frequencies in the range 3 to 75 Mc/s.

The question arises as to whether the information on the long wavelength Fourier components is representative of the E_1 pulse shown in fig.3.1 (c). From the form of the Fourier integral of E_1 (see equation 6.1), it can be seen that provided the E_1 pulse propagates without change

in shape, its amplitude will vary as the amplitudes of the Fourier components over the complete frequency range. This is the basic assumption made in the following interpretation.

6.2 Analysis of the Generated Stress Wave.

The piezoelectric field associated with the generated stress wave [see fig.3.1 (c)] is in principle given by

$$E_1(x,t) = \frac{1}{(2\pi)^{\frac{1}{2}}} \int_{-\infty}^{\infty} e^{i(kx - \omega t)} dk\, \mathcal{E}(k) \tag{6.1}$$

where $kv_s = \omega$ and $\mathcal{E}(k)$ is the spectral distribution function of the amplitudes associated with the piezoelectric stress wave within the crystal. As pointed out in the introduction, only those stress wave components in a frequency range $\Delta\omega = v_s \Delta k$ will be received by the detection apparatus, giving an output $A(\omega)$. Stress waves in the range $\Delta\omega$ will be associated with a piezoelectric field

$$\Delta E_1(x,t) = \frac{1}{(2\pi)^{\frac{1}{2}}} e^{i(kx - \omega t)} \frac{\Delta\omega}{v_s} \mathcal{E}(\omega) \tag{6.2}$$

The amplitude of the strain corresponding to this field may be calculated by means of the following relation

$$\frac{\partial u_1}{\partial x} \simeq - \frac{\epsilon}{4\pi\theta} E_1 \tag{6.3}$$

This relation follows from the following three equations:

$$D = 4\pi\theta S + \epsilon E \tag{6.4}$$

$$D_1 \simeq \text{constant} \tag{6.5}$$

$$\int_0^d E_1 dx = 0 \tag{6.6}$$

Equation (6.4) is one of the piezoelectric equations of state as given in Section 3.1. Because of the comparatively small total free charge Q within the specimen under the experimental conditions, Poisson's equation yields the relation (6.5). Also the condition $\int_0^d E_1 dx \simeq 0$, where d is the specimen thickness, is satisfied in the experiments.

The amplitude of the strain corresponding to the piezoelectric field ΔE_1 is therefore, according to equation (6.3) given by

$$\frac{\partial u_1}{\partial x} \simeq - \frac{\epsilon}{4\pi\theta} \frac{1}{(2\pi)^{\frac{1}{2}}} \frac{\Delta\omega}{v_s} \mathcal{E}(\omega) \tag{6.7}$$

The measured amplitude is given by

$$A(\omega) \simeq a(\omega) \frac{\partial u_1}{\partial x} \tag{6.8}$$

and a calibration experiment has to be carried out to determine the frequency dependent quantity $a(\omega)$. To perform the calibration, a signal generator, tuned to the frequency ω of the transducer, was connected across the CdS specimen as indicated in fig.6.1, and a sine wave of amplitude h was applied across the electrodes. Using the same amplifier gain as in the actual experiment, a signal of amplitude H was observed on the oscilloscope screen. Under these conditions, it can be shown that the calibrating strain $\left(\frac{\partial u}{\partial x}\right)_c$ produced in the specimen is approximately

$$\left(\frac{\partial u}{\partial x}\right)_c \simeq \frac{\theta}{c} \frac{h}{d} \tag{6.9}$$

Corresponding to equation (6.8) we have

$$H(\omega) \simeq a(\omega) \left(\frac{\partial u}{\partial x}\right)_c \qquad (6.10)$$

From equations (6.7), (6.8), (6.9) and (6.10) we obtain:

$$\left|\mathcal{E}(\omega)\right| = (2\pi)^{\frac{1}{2}} K^2 \frac{v_s}{\Delta\omega} \frac{h}{d} \frac{A(\omega)}{H(\omega)} \qquad (6.11)$$

where $K^2 = \frac{4\pi\theta^2}{\epsilon c}$ is the square of the electromechanical coupling constant.

With the result of the above analysis, it should be possible to estimate the amplitude $\mathcal{E}(\omega)$ of any particular component of the E_1 field pulse generated in the crystal.

By integrating equation (6.1) it should then have been possible to determine $E_1(x,0)$. However, one difficulty lies in the fact that the phase of $\mathcal{E}(\omega)$ cannot be determined. But the total extent of $E_1(x,t)$ can be found from the exact relation:

$$\int_{-\infty}^{\infty} |E_1(x,0)|^2 dx = \int_{-\infty}^{\infty} |\mathcal{E}(k)|^2 dk \qquad (6.12)$$

Suppose that by neglecting phase differences, results for $\mathcal{E}(k)$ and $E_1(x)$ would be obtained, as indicated in fig.6.2 (a) and (b). Then, if the values of k and x extend over a range δk and δx respectively, it can be shown that

$$\delta x \times \delta k \geqslant \tfrac{1}{2} \qquad (6.13)$$

It is sufficient in the present approximation to write

$$\delta x \times \delta k \simeq 1 \qquad (6.14)$$

If $|\mathcal{E}|_M$ and $|E_1|_M$ are the approximate maximum values indicated in fig. 6.2 (a) and (b), then we may write equation (6.12) as

$$|E_1(x)|_M^2 \delta x \simeq |\mathcal{E}(k)|_M^2 \delta k \qquad (6.15)$$

From equations (6.14) and (6.15) we have

$$|E_1(x)|_M \simeq \frac{|\mathcal{E}(k)|_M}{\delta x} \qquad (6.16)$$

The above result will now be applied to the experimental results for the long wavelength Fourier components shown in fig.5.10. These results give the values of $\mathcal{E}(\omega)$, normalized to the charge Q, for six different frequencies. In view of the resonance effect at about 30 Mc/s, it seems reasonable to take the average amplitude of the components in the low frequency range from 3 to 75 Mc/s. The piezoelectric field E_1 according to equation (6.16) is then about 1·2 kV cm^{-1}, using a value of 3.10^{-4}cm for δx. This must be regarded very much as a lower limit of E_1, because the experimentally determined value of $\mathcal{E}(\omega)$ refers to the low frequency components and is likely to be only a fraction of $|\mathcal{E}(k)|_M$. Nevertheless, piezoelectric fields >1 kV cm^{-1} go a long way towards explaining the non-ohmic transport behaviour shown in fig.5.1 (a). For instance, for an applied field of 1·3 kV cm^{-1}, a value of $E_1 \simeq 0{\cdot}5$ kV cm^{-1} is required to explain the discontinuity in fig.5.1 (a).

6.3 The Main Results.

The principal results described in the last chapter are the following:

(a) The dependence of the observed acoustic amplitude A on the applied field E_o (Fig.5.4).

(b) The dependence of A on the charge Q flowing through the

crystal (Fig.5.6).

(c) The dependence of A/Q on incident electron excitation energy V_p (Fig.5.7).

(d) The temperature dependence of the acoustic amplitude A (Fig.5.12).

In addition, the dependence of A on the excitation pulse length T_p, and on the intensity of monochromatic illumination incident on the top electrode was determined.

A model for the interaction will now be proposed, which is, within certain limits, consistent with the above results.

6.4 The Microscopic Model.

In this approach a single incident electron is considered, and its contribution to the build-up of the observed piezoelectric wave is assumed to be independent of any other incident electron. The total observed interaction may therefore be regarded as the superposition of all the individual interactions. This assumption is justified in view of the average separation between any two neighbouring incident electrons. Thus, for an incident beam current of 2·5 μA, about 5×10^5 electrons fall on an area of 0·03 cm^2 during a 30 nsec pulse. Even if all the electrons arrived simultaneously, the average distance between them would still be 2·5 μm.

As suggested in Fig.3.1 (c), each incident electron gives rise to a piezoelectric wavelet and it is reasonable to assume that the extent

of this wavelet is equal to the average penetration depth d_p of the incident electrons [Section 3.1 (a)]. Because of the spatial separation referred to above, interference between the piezoelectric wavelets is unlikely for the beam currents used here.

On the microscopic model it is possible to see how the observed ultrasonic amplitude A depends on some of the experimental parameters. This analysis refers to results at room temperature and the effects of shallow trapping and release will be neglected.

The amplitude A may be expected to depend on two factors:

(i) the total number of piezoelectric wavelets produced. This number is equal to the total number of electrons incident during the excitation pulse $i_b T_p / e$, and

(ii) the density of charge available for bunching in each of the piezoelectric wavelets. Now, the number of electrons generated by one incident electron having energy V_p is V_p / χ, where χ is the energy required to generate one electron-hole pair and is equal to about 10 eV in CdS [Lappe (1959)]. A fraction $f(E_o, d_p)$ which will depend on the applied field and on the average depth of penetration of the incident beam, escape recombination in the generation region, so that the density of charge available for bunching in each piezoelectric wavelet is given by $\frac{V_p}{\chi} f(E_o, d_p) \frac{1}{a\delta} C$. In this equation $a\delta$ denotes the initial volume occupied by the charge carriers which have escaped recombination. The parameter C describes the subsequent concentrating effect of the field

gradient in the barrier region (see Section 6.5).

As there are $i_b T_p / e$ individual wavelets, superposition leads to the total observed amplitude

$$A = \beta \frac{i_b T_p}{e} \quad \frac{V_p}{\chi} \quad f(E_o, d_p) \quad \frac{1}{\alpha\delta} \quad C \qquad (6.17)$$

where β is a constant of proportionality.

Now, the quantity $\frac{i_b T_p}{e} \quad \frac{V_p}{\chi} \quad f(E_o, d_p)$ is Q, the total number of electrons that have escaped from the generation region. Thus $A \propto Q$ at a given E_o and d_p, a relation that has been verified (see fig.5.6).

The form of the function $f(E_o, d_p)$ may be determined from the graph of Q against E_o (fig.5.5). The charge Q increases linearly with field for values of $E_o \lesssim 4E'$, whilst at higher fields Q saturates. This behaviour resembles closely the dependence of A on E_o as seen in Fig.5.4. From these results A/Q has been plotted in Fig.6.3 as a function of E_o. It can be seen that A/Q is approximately constant up to values of $E_o \simeq 7E'$. The saturation of A with E_o is therefore a direct consequence of the saturation of Q.

The linear increase of Q with E_o at lower fields may be explained if a constant recombination lifetime τ_r in the generation region is assumed. Thus the fraction $f = \mu E_B \tau_r / d_p$, where E_B is the field in the barrier region (see Section 6.5). At higher fields Q saturates, and from Fig.5.5 it can be deduced that only about 1/5 of the generated carriers are extracted for an incident beam current of 2·4 μA. Therefore the observed saturation does not represent a complete extraction of the

carriers from the generation region. A possible reason for this behaviour is that there may be a limited fraction of the applied potential that can develop across the barrier region; this will be discussed in the next Section.

6.5 The Dependence of the Ultrasonic Amplitude on the Barrier Field and the Incident Electron Energy.

(a) The Effect of the Barrier Field.

Experimental results presented in Fig.5.11 suggest that the field within the barrier is closely related to the amplitude A of the observed ultrasonic wave.

The average field in the barrier $\bar{E}_b$ for zero applied field may be calculated using equation (3.16). Thus, for $N_d \simeq 10^{14}$ cm^{-3}, $\lambda \simeq 3 \times 10^{-4}$ cm., E_b may be determined using the relation

$$|\bar{E}_b| = \frac{V_D}{\lambda} \qquad (6.18)$$

where $V_D = \phi_m - \phi_s \simeq 0{\cdot}7$ eV. Thus $|\bar{E}_b| \simeq 2{\cdot}3 \times 10^3$ V cm^{-1}, whilst if $N_d \simeq 10^{15}$ cm^{-3}, $|\bar{E}_b| \simeq 7 \times 10^3$ V cm^{-1}.

Under the influence of an applied potential, the field in the barrier may be appreciably altered. The resistivity of the barrier region is likely to be greater than the resistivity of the bulk, so that the fraction of the applied field that will develop across the barrier would be larger than that across a similar width in the bulk of the specimen. Equation (3.16) then becomes :

$$V_D + V_1 = 2\pi N_d e \lambda^2 / \epsilon \qquad (6.19)$$

where V_1 denotes that part of the applied potential developing across the barrier.

It is now necessary to estimate V_1. The results of paper I (see Section 2.3) verified the relation $v_s = \mu E'$ along different crystallographic directions for a large number of specimens to within about 10% or less. This indicates that the value of E', calculated from V_o and d, must have been correct to within about 10%. This fact will now be used as a criterion to estimate the maximum value of V_1.

Consider the following rather oversimplified model:

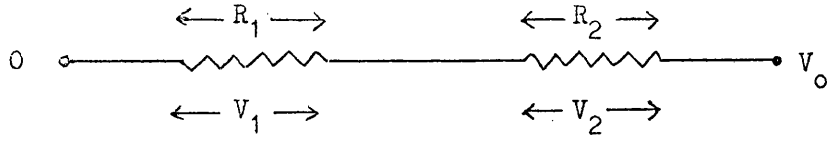

The resistances of the barrier and the bulk of the specimen are represented by R_1 and R_2 respectively and the corresponding potentials are V_1 and V_2. If the resistivities of the barrier and the bulk of the specimen are ρ_1 and ρ_2 respectively, then $\rho_1 \lambda / \rho_2 d \lesssim 0{\cdot}1$. Now, $\lambda/d \lesssim 1/50$, so that $\rho_1 / \rho_2 \lesssim 5$. Using these results we have :

$$V_2 \simeq V_o \qquad (6.20)$$

$$\text{and} \quad V_1 \simeq z \lambda E_o \qquad (6.21)$$

where $z = \rho_1 / \rho_2$. Under these conditions equation (6.19) becomes

$$V_D + z \lambda E_o = 2\pi N_d e \lambda^2 / \epsilon \qquad (6.22)$$

The solution for λ is

$$\lambda = \frac{zE_o \pm \sqrt{z^2 E_o^2 + 4V_D\, 2\pi N_d\, e/\epsilon}}{2.2\pi N_d e/\epsilon} \qquad (6.23)$$

and corresponding to equation (6.18) we have

$$|E_B| = \frac{V_D + zE_o\lambda}{\lambda} \qquad (6.24)$$

For values of $E_o \gtrsim 3E'$, and $N_d \lesssim 10^{15}$ cm^{-3}, the first term under the square root in equation (6.23) becomes the dominant term. If then the second term is neglected, we have

$$\lambda \simeq \frac{zE_o}{2\pi N_d e/\epsilon} \qquad (6.25)$$

$$\text{and} \quad |E_B| \simeq z|E_o| \qquad (6.26)$$

If we take $z \simeq 5$ (see above), and $N_d \simeq 10^{15}$ cm^{-3}, then $|E_B| \simeq 5|E_o| \simeq 25$ kV cm^{-1} and $\lambda \simeq 3\mu$m. Therefore, with applied fields $\gtrsim 3E'$ one would expect on the above simple model a high field $|E_B| \simeq 5|E_o|$ to exist within the barrier region. In the bulk of the specimen the field is approximately E_o, and between these two field regions there must be a transition region as indicated in Fig.6.4.

The above analysis led to a maximum value of about 5 for the ratio ρ_1/ρ_2. According to the simple model this implies that for $E_o \gtrsim 3E'$, E_B increases linearly with E_o. This rests on the doubtful assumption that R_1 remains constant, independent of E_o. A number of factors, such as the increasing value of Q at the larger fields and possibly also an increase in hole density near the surface, suggests that R_1 is likely to decrease at the higher applied fields. Under these

conditions, E_B may reach a substantially constant maximum value and no longer increase in proportion to E_o. As the barrier field is primarily responsible for the extraction of the generated electrons, the observed saturation of Q with E_o (fig.5.5) may well be associated with this.

The effect of the barrier field on the density of a group of electrons will now be considered. If a sheet of charges of density n_B drifts in the field gradient from E_B to E_o, then

$$n_o = n_B \; E_B / E_o \simeq n_B \; z \qquad (6.27)$$

Therefore the space charge density may be increased by a factor of up to 5. This increase in density is described by the parameter C in equation (6.17), so that within the limits of the above estimate $C \lesssim 5$.

(b) The Effect of the Incident Electron Energy.

In the experiments the depth of penetration of the incident electrons was altered by varying their energy eV_p. This provides a useful way of probing the processes taking place in the barrier region.

The results of Ehrenberg and King (1963) reproduced in Fig.6.5 show the dissipation of energy per micron of the incident electrons as a function of the depth below the surface for CsI. It is possible to use these results for CdS as both materials have about the same density. The depth d_p below the surface of the halfwidth of the distribution as a function of the incident electron energy may be deduced from Fig.6.5 and is shown in Fig.6.6.

The above information was used in Fig.5.7 where A/Q was plotted

against V_p for three different applied fields. The three curves show an approximate linear increase at low values of V_p, whilst at higher V_p A/Q tends to a saturation value.

An attempt will now be made to describe this result in terms of the microscopic model. Equation (6.17) may be written in the following form

$$\frac{A}{Q} = \beta \frac{1}{a\delta} C \qquad (6.28)$$

Now, for lower values of V_p most of the escaping electrons experience the field gradient from E_B to E_o (fig.6.4), and therefore C should be approximately constant. Thus an increase in A/Q with increasing V_p indicates that the factor $a\delta$ must decrease. This will be discussed further in the next Section where a quantitative estimate of a and δ is made.

The saturation following the linear region may be explained in the following way. With larger values of V_p, and hence d_p, some of the carriers are generated in the field E_o beyond the transition region (fig.6.4). These carriers do not experience the concentrating effect of the field gradient and therefore their contribution to the subsequent interaction with the piezoelectric wavelet will be reduced. As V_p is further increased, more of the escaping carriers are produced outside the critical depth. Figure 5.7 indicates that this is 2 - 3 μm, comparable to the estimated barrier width.

6.6 Details of the Interaction of the Carriers with the Generated Stress Wave.

A model was presented in the preceding sections in which each incident electron generated a piezoelectric wavelet. A relation for the ultrasonic amplitude A was derived from considerations on the interaction of the generated electrons with the piezoelectric wavelets [equation (6.17)]. In this Section the parameters of equation (6.17) are evaluated in an attempt to determine whether the interaction between the electrons and wavelets may be explained in terms of the linear White theory (see Section 2.1).

The form and dimensions of the generated electron distribution is shown in Fig.6.7 for $V_p \simeq 30$ kV. This has been deduced directly by Ehrenberg and Franks (1953), from measurements of the cathodoluminescence in CsI crystals containing luminescent centres. It can be seen from Fig.6.7, typical of the results obtained by the above authors, that the electron cloud extends to within an average depth d_p and also has a diameter of about that value. The electrons likely to escape recombination are represented by the shaded region.

From Fig.5.5 the number of electrons escaping recombination is $Q = 1{\cdot}6 \times 10^8$ for an applied field $E_o \simeq 3E'$ and beam current of 2·4 μA. If it is assumed that generation is essentially uniform throughout the generated distribution, then, to a first approximation the width of the shaded region $\delta = d_p / 10 \simeq 0{\cdot}25$ μm. If the radius of the escaping distribution is $\simeq 1$ μm then the density in this localized region is

$\simeq 10^{15}$ cm^{-3}. This may be increased by up to a factor of 5, and in this case the corresponding conductivity would be 2×10^{-1} $(\Omega\, cm)^{-1}$. Most of these electrons then catch up with the generated piezoelectric wave and begin to interact.

It is possible to apply the White theory (Section 2.1) to the above system and calculate the expected amplification. With the above conductivity of 2×10^{-1} $(\Omega\, cm)^{-1}$, equation (2.1) gives an amplification factor $\alpha = 3 \times 10^{2}$. The corresponding build-up time constant is $\simeq 7{\cdot}5$ nsec. This value has been calculated for a frequency component leading to maximum amplification ($\nu = 8 \times 10^{9}$ c.p.s.).

The important conclusion of the above analysis is that the White theory can account for the extremely rapid build-up of the transient acoustoelectric interaction in high resistivity CdS observed in the previous work (paper I).

6.7 The Effect of Monochromatic Illumination.

The factor C was altered in the experiments, by means of highly absorbed monochromatic illumination on the top electrode. The effect of increasing the light intensity was shown in Fig.5.11. This causes a decrease in the barrier field so that the concentrating effect of the barrier diminishes (i.e. C decreases). Under these circumstances the density of carriers available for bunching is less, leading to a reduced amplification of the piezoelectric wavelet.

6.8 The Dependence of the Ultrasonic Amplitude on the Excitation Pulse Length.

On the basis of the above model the generated piezoelectric wavelets are unlikely to interfere with each other by virtue of their spatial separation (Section 6.4). The interference effects observed in the results shown in Fig.5.8 of A/Q against T_p appear at first sight to be inconsistent with this conclusion. However, it must be remembered that experimentally we measure the amplitude of the low frequency Fourier components, whose wavelength is comparable to the specimen thickness. Destructive interference between these long wavelength components is to be expected if the appropriate conditions are satisfied.

It is therefore concluded that the results are associated with the method of detection, and not with the microscopic phenomena discussed in Section 6.4.

6.9 The Temperature Dependence of the Amplitude of the Generated Stress Wave.

In the previous sections it has been assumed that all of the electrons escaping the generation region are available for bunching. This assumption is reasonable, since for most CdS specimens at room temperature the measured drift mobility $\mu_d \simeq \mu_L$, the lattice mobility. However, at lower temperatures only a fraction of the drifting charge will be free at any instant due to the presence of shallow traps. By

virtue of the statistical nature of trapping and release, the width of the distribution of drifting electrons will increase with time, and therefore the effective local density within the distribution will decrease.

A comparison of the transit time for a carrier traversing the barrier region and the free time of the carrier shows that there is a high probability of carriers being trapped during their transit across the barrier region. Typically, the barrier transit time in absence of shallow trapping is $\simeq 10^{-9}$ sec , while the carrier free time τ_f is of the order of 10^{-10} sec at 80°K and 10^{-9} sec at 220°K. These values for τ_f have been calculated using the relation $\tau_f = 1/N_t v_{th} S$, with a trap density $N_t = 10^{16}$ cm^{-3} , and a capture cross section $S = 3{\cdot}6 \times 10^{-10} T^{-2}$.

It is necessary to discuss the effect of trapping and release in the following two intervals:

(*i*) During the first few nanoseconds after generation, but <u>before</u> a stable bunching point has been reached. The decrease in the local density of electrons in this region will affect the build-up of the piezoelectric signal. The loss of amplitude with decreasing temperature is clearly shown in Fig.5.12. The interesting feature of the result is that at a temperature T' of about 170°K, when $\mu_d / \mu_L \simeq 0{\cdot}37$ for the particular specimen, A reaches an essentially steady value. This indicates that even at temperatures below T', the density of the electron distribution reaching the wavelet is still sufficient to cause some interaction leading to an apparently constant small

background signal.

(ii) In the interval between the initial bunching process and the completion of the transit. During this time trapping and release will lead to an increased effective diffusion out of the stable bunching region [fig.3.2 (b)] . This has been observed in the experiments described in paper I where the marked discontinuity in the (v_d , E_o) curves (e.g. fig.2.7) disappears completely at a critical temperature T'. The drift mobility measurements showed that the temperature T' always corresponded to the limiting ratio $\mu_d / \mu_L \simeq 0{\cdot}37$, so that there appears to be a close correlation between phenomena taking place in the two time intervals. Although the present work shows that there still exists a background signal at $T < T'$, its amplitude is not sufficient to cause any prolonged bunching during transit, which could lead to an observable effect on the drift velocity.

6.10 Conclusions.

1. A correlation has been established between the threshold of the ultrasonic signal and the onset of the transient acoustoelectric interaction. This threshold occurs when the electron drift velocity is equal to the sound velocity in the appropriate crystallographic direction.

2. The acoustic amplitude is proportional to the number of drifting electrons Q which complete their transit across the specimen.

3. The dependence of the acoustic amplitude A on the applied field E_o

is essentially determined by the dependence of Q on E_o.

4. There exists a critical region which plays an important role in the generation of the observed ultrasonic wave. The extent of this region has been determined from measurements with different incident electron energies and with steady illumination of the top gold electrode.

5. In experiments where the duration T_p of the excitation pulse is varied, interference effects are observed. It is fairly certain that these are connected with the long wavelength Fourier components which were detected by the transducer in the experiments.

6. The frequency dependence of the generated ultrasonic amplitude has been investigated between 3 and 75 Mc/s. An estimate based on the results for these long wavelength Fourier components leads to a piezoelectric field in excess of 1 kV cm^{-1}.

7. A microscopic model for the transient acoustoelectric interaction is presented in which a single incident electron (or photon) is considered. An incident electron simultaneously generates a piezoelectric wavelet and a cloud of charge. The charges are subsequently bunched in the wavelet.

8. The presence of a strong barrier field leads to a high field gradient within a few microns from the surface. This gradient is likely to cause an increase in the density of the drifting charge before bunching in the piezoelectric wavelet.

9. On the basis of the microscopic model the local charge density was determined and found to be of sufficient magnitude to lead to a build-up time for the interaction of less than 10 nsec , as calculated from the linear White amplification theory. This conclusion resolves one of the main difficulties of the previous work on the transient acoustoelectric interaction.

10. The effect of steady illumination and of decreasing temperature both tend to decrease the local density of the generated carriers. In the case of illumination this occurs through a decrease in the barrier height, whilst lowering the temperature causes a reduced density as a result of shallow trapping and release.

APPENDIX I

The Theory of Stub Matching.

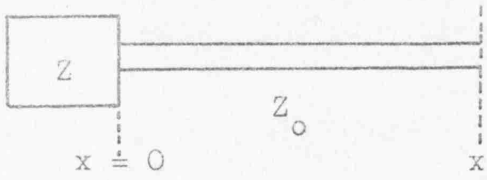

Fig.(a)

If a device having an impedance Z is connected to a length of coaxial line having a characteristic impedance Z_o, then, looking towards the device from a point x fig.(a) , the impedance Z' is given by

$$Z' = Z_o \frac{Z + jZ_o \tan\beta x}{Z_o + jZ\tan\beta x} \qquad (A1)$$

where $\beta = 2\pi/\lambda$. In deriving the above relation, [see, for example, Rollin (1964)], the coaxial line is assumed to be lossless. It is possible to write equation (A1) in terms of admittance Y:

$$Y' = Y_o \frac{Y + jY_o \tan\beta x}{Y_o + jY\tan\beta x} \qquad (A2)$$

There is obviously some distance x_1 for which the real part of the expression $\frac{Y + jY_o \tan\beta x}{Y_o + jY\tan\beta x}$ is unity and therefore Y' is of the form $Y' = Y_o + jS$, where Y_o is the characteristic conductance and 1/S is a pure reactance. If at x_1 we connect in parallel with the line a pure reactance X exactly cancelling S, the admittance looking towards the device at this point is Y_o. Under these conditions the line is correctly terminated. The stub, which provides the pure reactance X is

shown below in fig.(b).

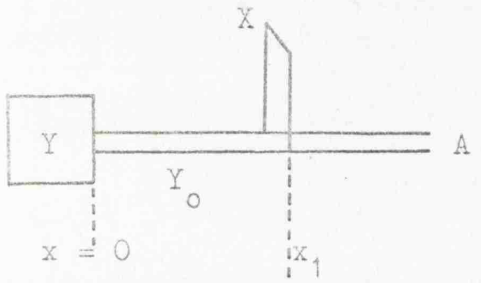

$$\text{At } x = x_1,\ Y' = Y_o + jS + j\frac{1}{X} = Y_o$$

Fig.(b)

From A, an arbitrary point on the line an admittance Y_o is seen.

In the experiments the device was a transducer. For the coaxial cable used, Z_o = 50 ohm. The input impedance of the crystal mixer was also 50 ohm. As shown above, the transducer may be matched to the crystal mixer by placing a stub having a pure reactance X at a particular distance from the transducer.

The disadvantage of using a single stub is that the distance x_1 has to be correct for a given system. An analysis similar to that given above shows that matching may be achieved in most instances with two stubs placed at an arbitrary distance from the device. In this case the two stubs are usually spaced $\lambda/4$ apart.

A more rigorous investigation of the double stub unit, using a Smith Chart [Smith (1939)] shows that in order to match any impedance to any other impedance then three stubs are necessary. For this reason the triple stub tuner, described in Chapter 4 was used.

References.

Blotekjaer, K., and Quate, C.F., Proc. IEEE, 52, 360, (1964).

Cardona, M., and Harbeke, G., Phys. Rev. 137, A1467, (1965).

Carleton, H.R., and Auer, P.L., Solid State Electronics, 8, 285, (1965).

Ehrenberg, W., and Franks, J., Proc. Phys. Soc. B, 66, 1057, (1953).

Ehrenberg, W., and King, D.E.N., Proc. Phys. Soc., 81, 751, (1963).

Fletcher, R.C., Rev. Sci. Instrum., 20, 861, (1949).

Foster, N.F., IEEE, Trans.on Sonics and Ultrasonics, 11, 63, (1964).

Goodman, A.M., J. Appl. Phys., 35, 573, (1964).

Gurevich, V.L., and Laikhtman, B.D., Soviet Physics JETP, 19, 407, (1964).

Hamaguchi, C., Otsuki, T., Watanabe, Y., and Inuishi, Y., Jap. J. Appl. Phys., 3, 492, (1964).

Haydl, W.H., Stanford University, Microwave Laboratory Report, No. 1517, (1967).

Haydl, W.H., and Quate, C.F., Appl. Phys. Letters, 7, 45, (1965).

Haydl, W.H., and Quate, C.F., Phys. Letters, 20, 463, (1966).

Hutson, A.R., Phys. Rev. Letters, 4, 505, (1960).

Hutson, A.R., McFee, J.H., and White, D.L., Phys. Rev. Letters, 7, 237, (1961).

Hutson, A.R., and White, D.L., J. Appl. Phys., 33, 40, (1962).

Lappe, F., Z.Phys., 154, 267, (1959).

LeComber, P.G., Spear, W.E., and Weinmann, A., Brit. J. Appl. Phys., 17, 467, (1966).

Lehovec, K., Phys. Rev., 74, 463, (1948).

McFee, J.H., J. Appl. Phys., 34, 1548, (1963).

McFee, J.H., and Tien, P.K., J. Appl. Phys. 37, 2754, (1966).

Pippard, A.B., Phil. Mag., 8, 161, (1963).

Prohofsky, E.W., Phys. Rev. 134, A1302 , (1964).

Ridley, B.K., Proc. Phys. Soc., 82, 954, (1963).

Rollin, B.V., " An Introduction to Electronics", page 13, Clarendon Press, Oxford, (1964).

Schottky, W., Zeits. f. Physik, 118, 539, (1942).

Smith, P.H., "Transmission Line Calculator", Electronics, Jan., (1939).

Smith, R.W., Phys. Rev. Letters, 9, 87, (1962).

Smith, R.W., and Moore, A.R., Proceedings International Conference on the Physics of Semiconductors, 575, (1964).

Spear, W.E., Proc. Phys. Soc., 76, 826, (1960).

Spear, W.E., Adams, A., and Henderson, G., J. Sci. Instrum., 40, 332, (1963).

Spear, W.E., Lanyon, H.P.D., and Mort, J., J. Sci. Instrum., 39, 81, (1962).

Spear, W.E., and Mort, J., Proc. Phys. Soc., 81, 130, (1963).

Tsu, R., J. Appl. Phys. 35, 125, (1964).

Uchida, I., Ishiguro, T., Sasaki, Y., and Suzuki, T., J. Phys. Soc. Japan, 19, 674, (1964).

White, D.L., J. Appl. Phys. 33, 2547, (1962).

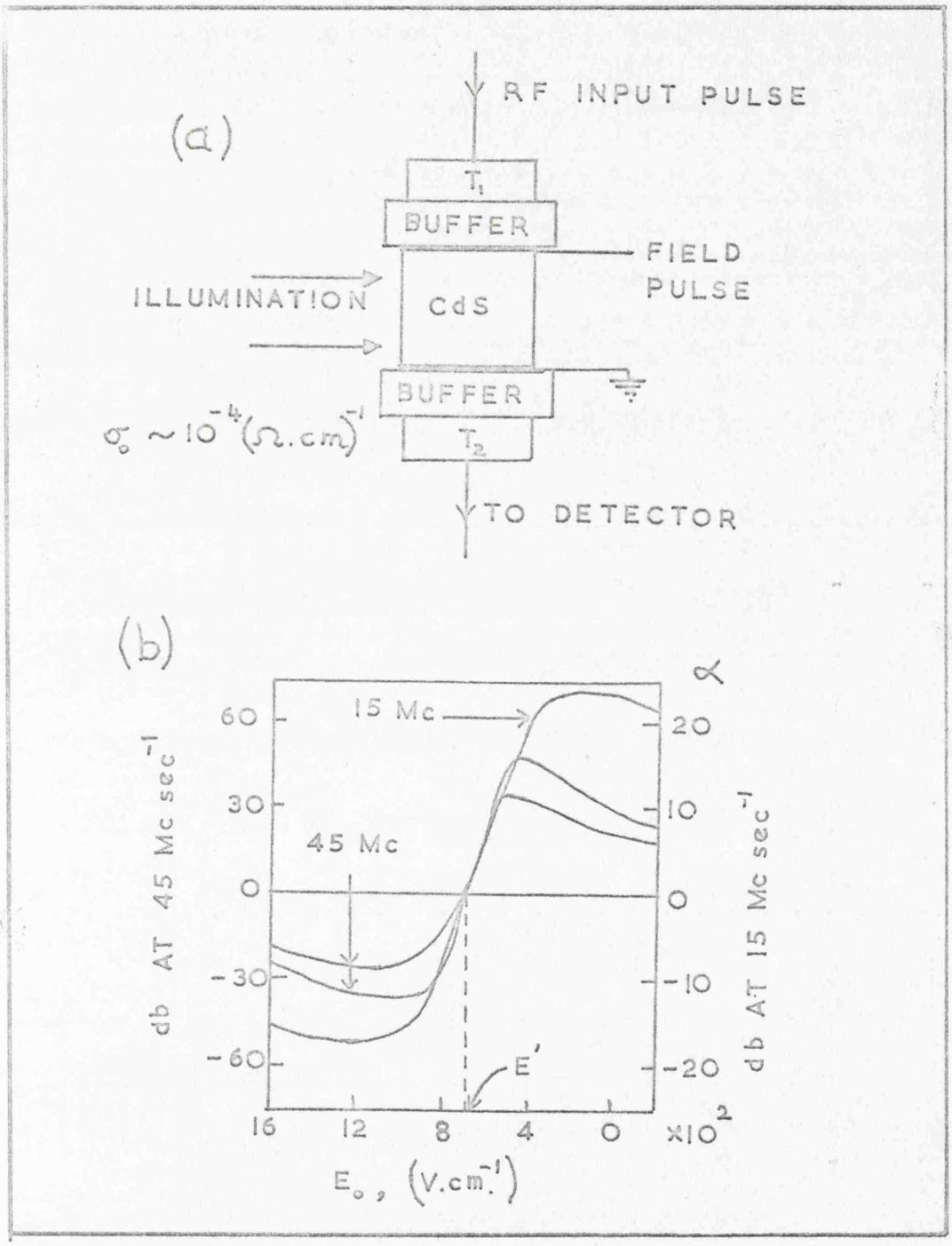

Fig.2.1 (a) Block diagram of the experimental arrangement used to observe ultrasonic amplification in CdS.

(b) Observed attenuation as a function of the applied field. After Hutson, McFee and White (1961).

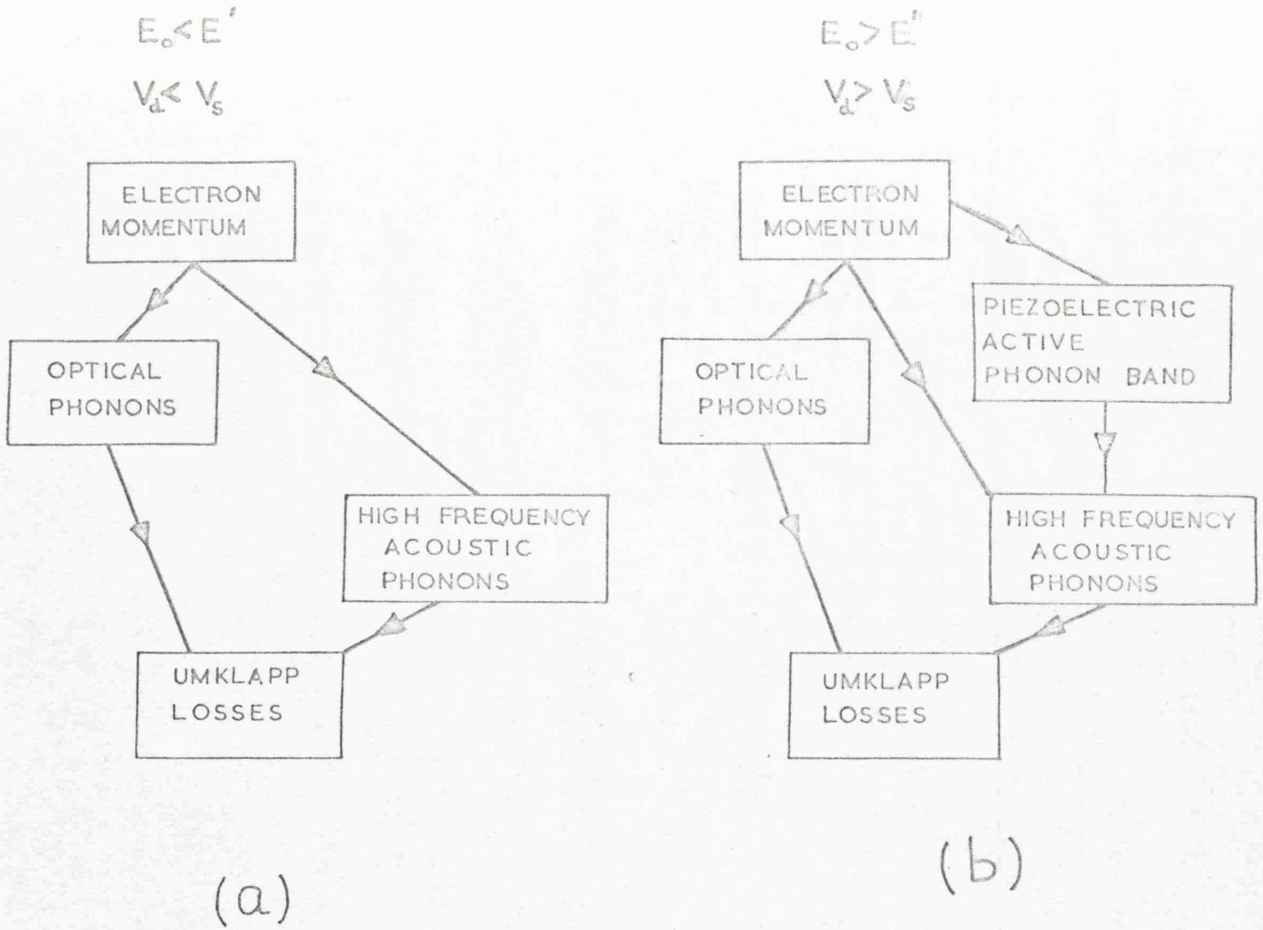

Fig.2.2 Momentum relaxation diagram for electrons,

(a) in the absence of stimulated emission

(b) in the presence of stimulated emission.

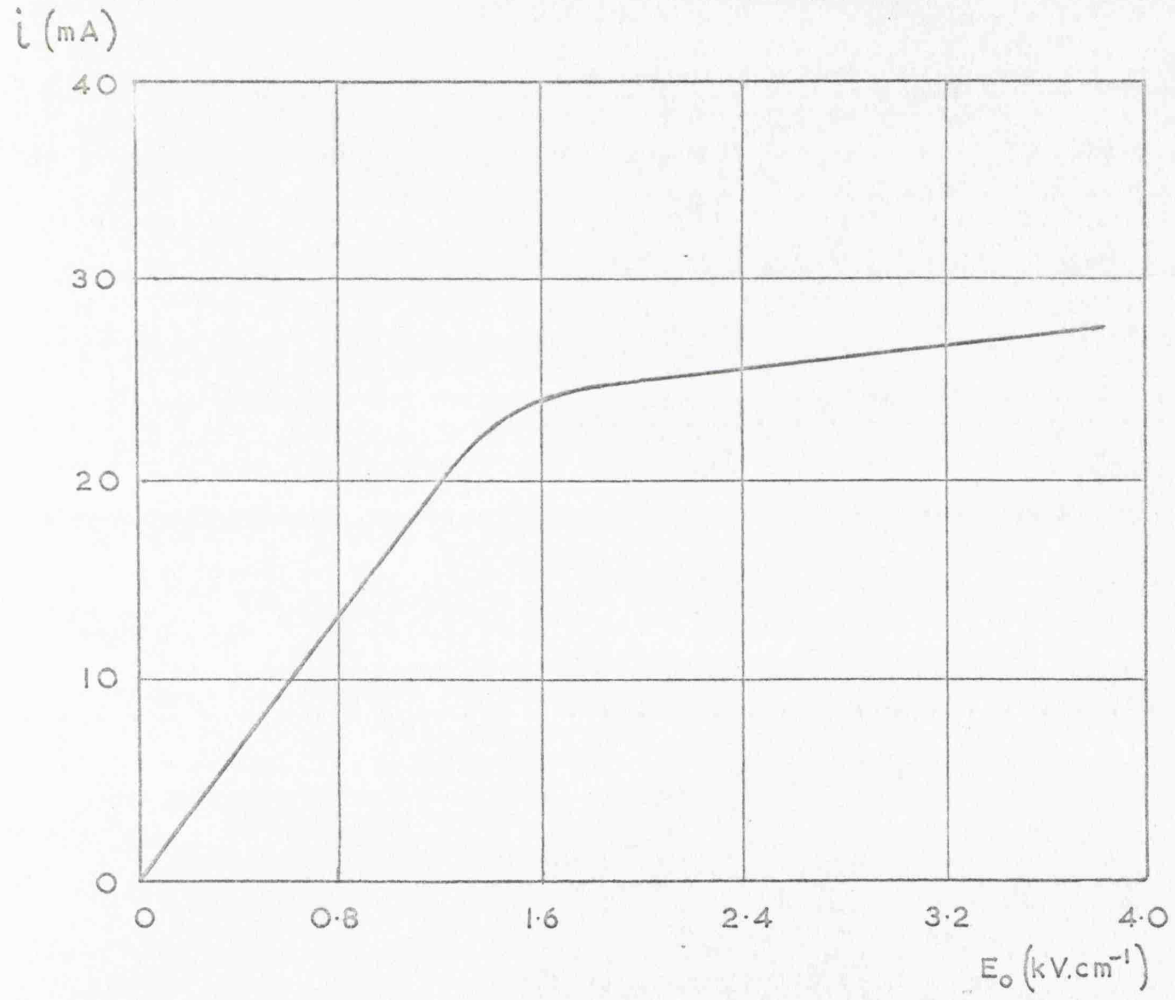

Fig.2.3 Showing the observed i-E_o characteristic for a semiconducting CdS specimen, with the applied field parallel to the c axis. After Smith (1962).

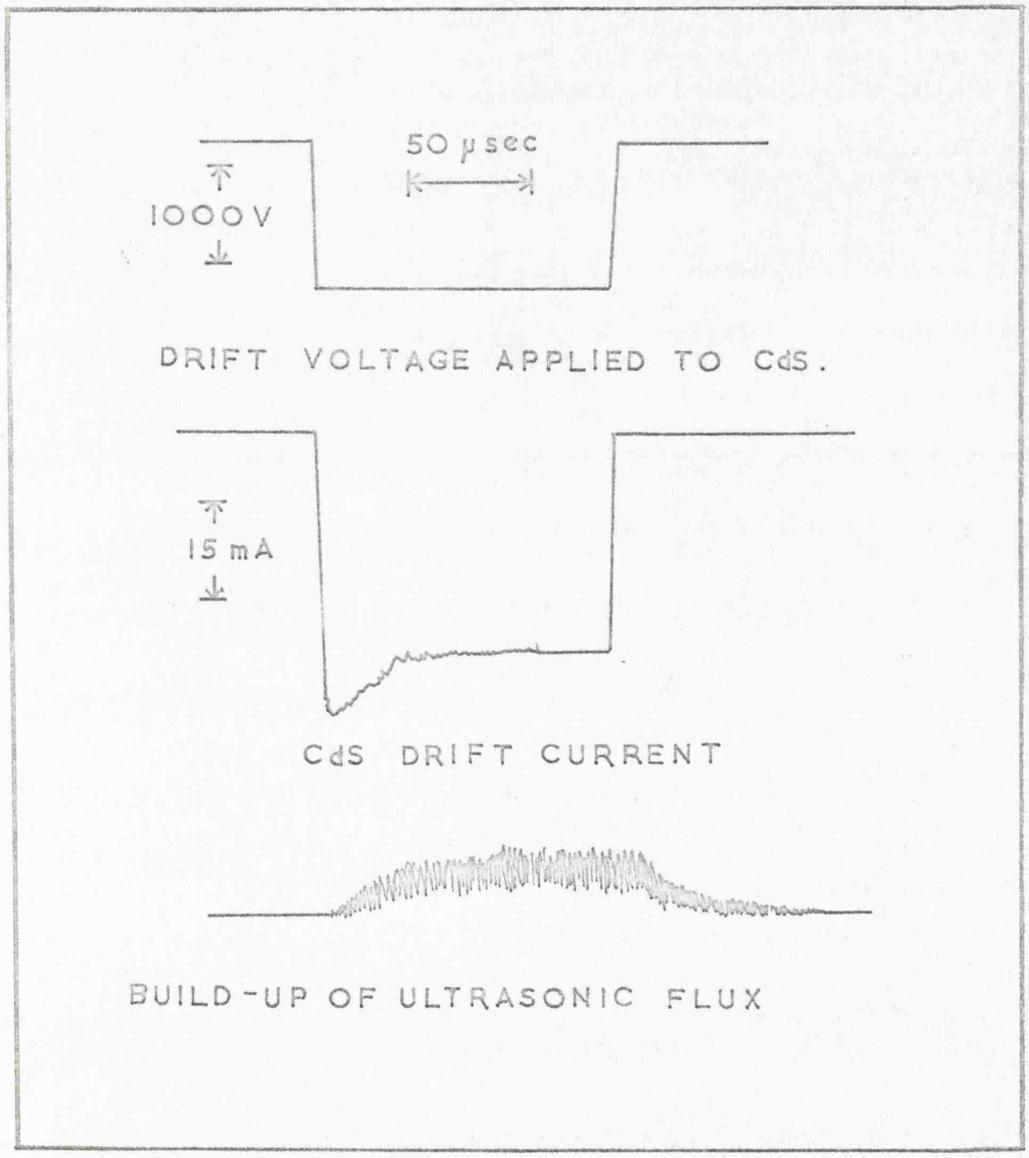

Fig.2.4 Current saturation and build-up of ultrasonic flux in a CdS sample.

After McFee (1963).

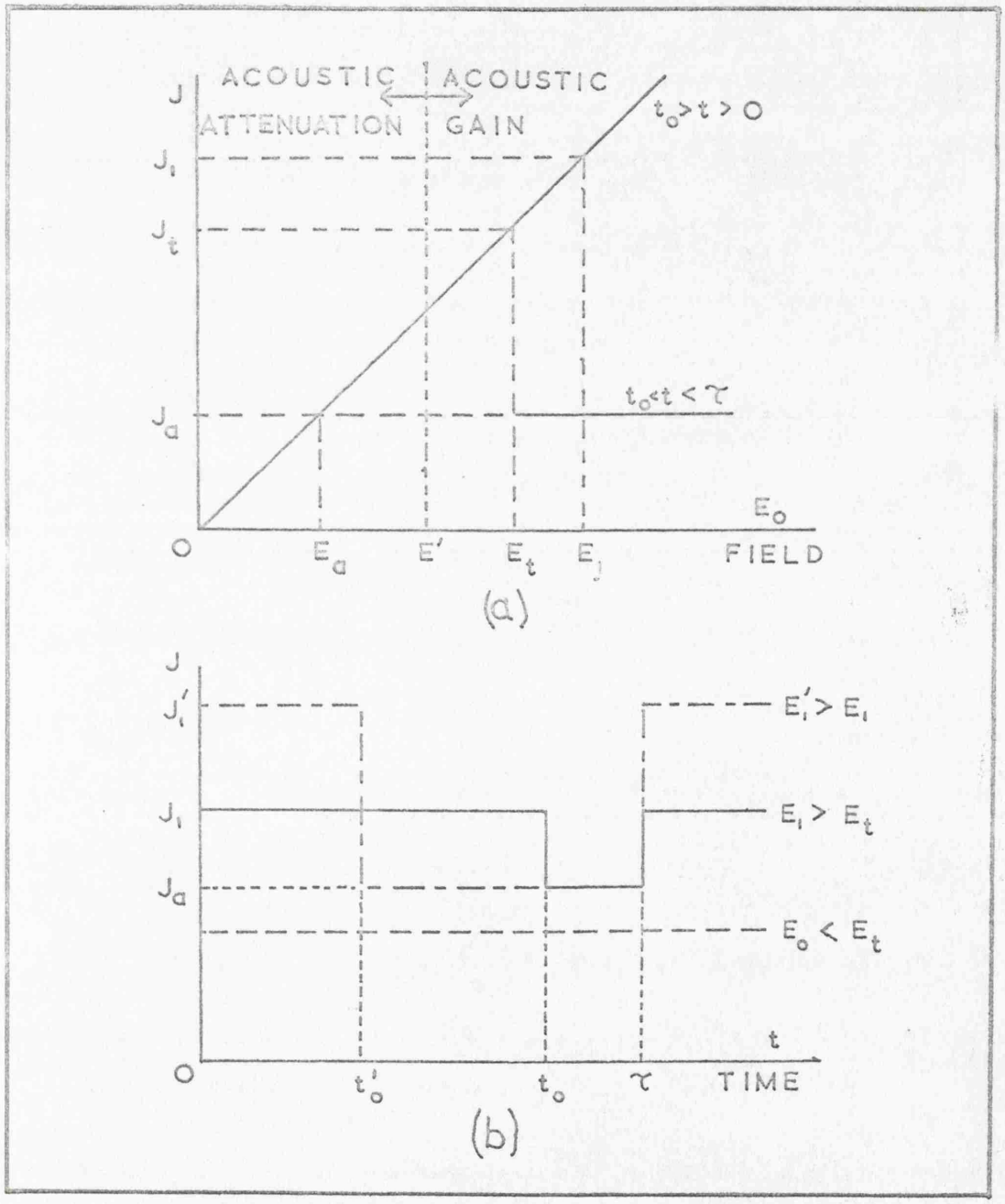

Fig.2.5 (a) and (b) showing the J-E_o curve and the current waveform as a function of time respectively, for the case of current oscillations in a homogeneous piezoelectric semiconductor. After Haydl (1967).

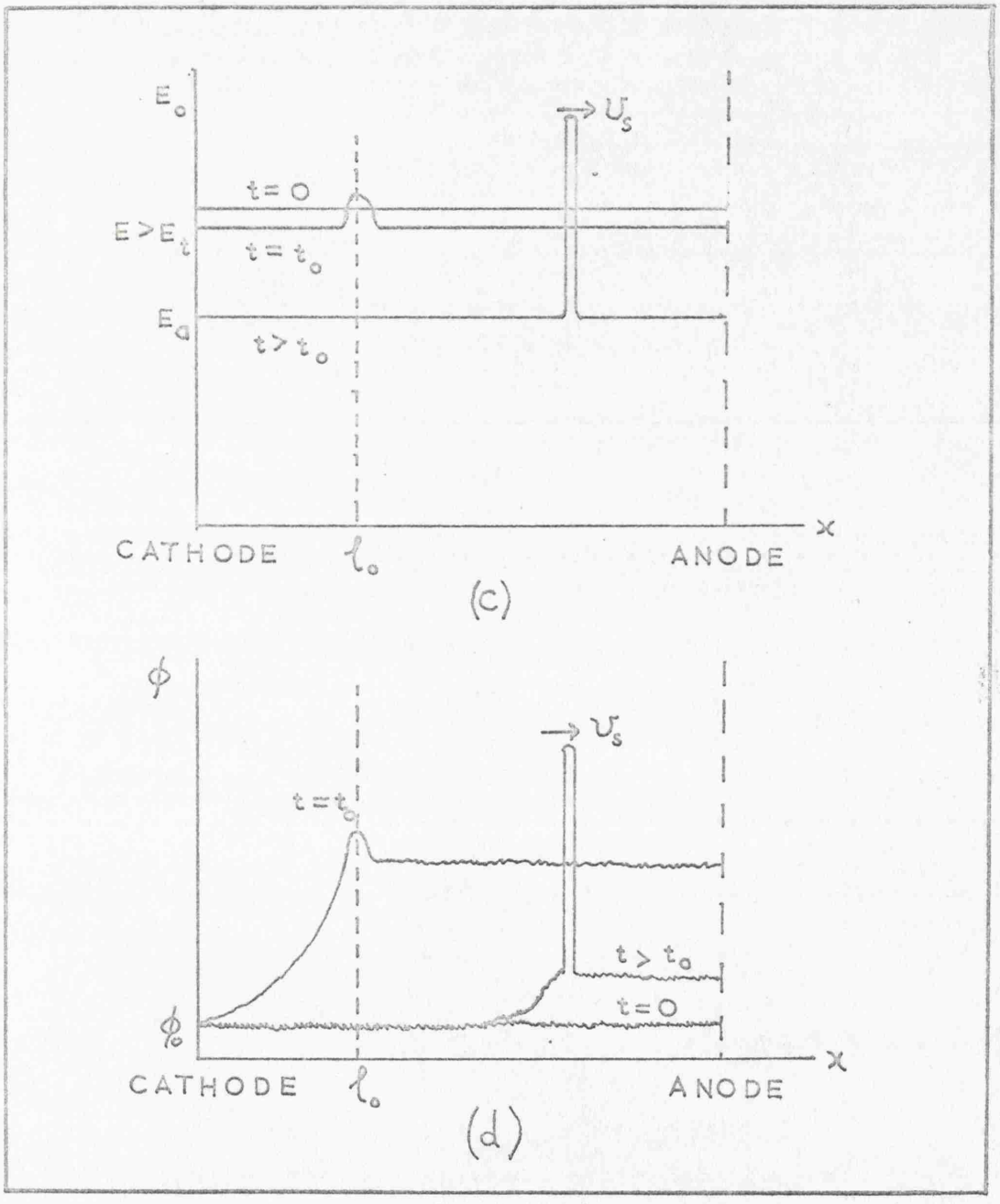

Fig.2.5 (c) and (d) showing the field distribution and the acoustic noise distribution ϕ as a function of time, during the formation of a domain.

After Haydl (1967).

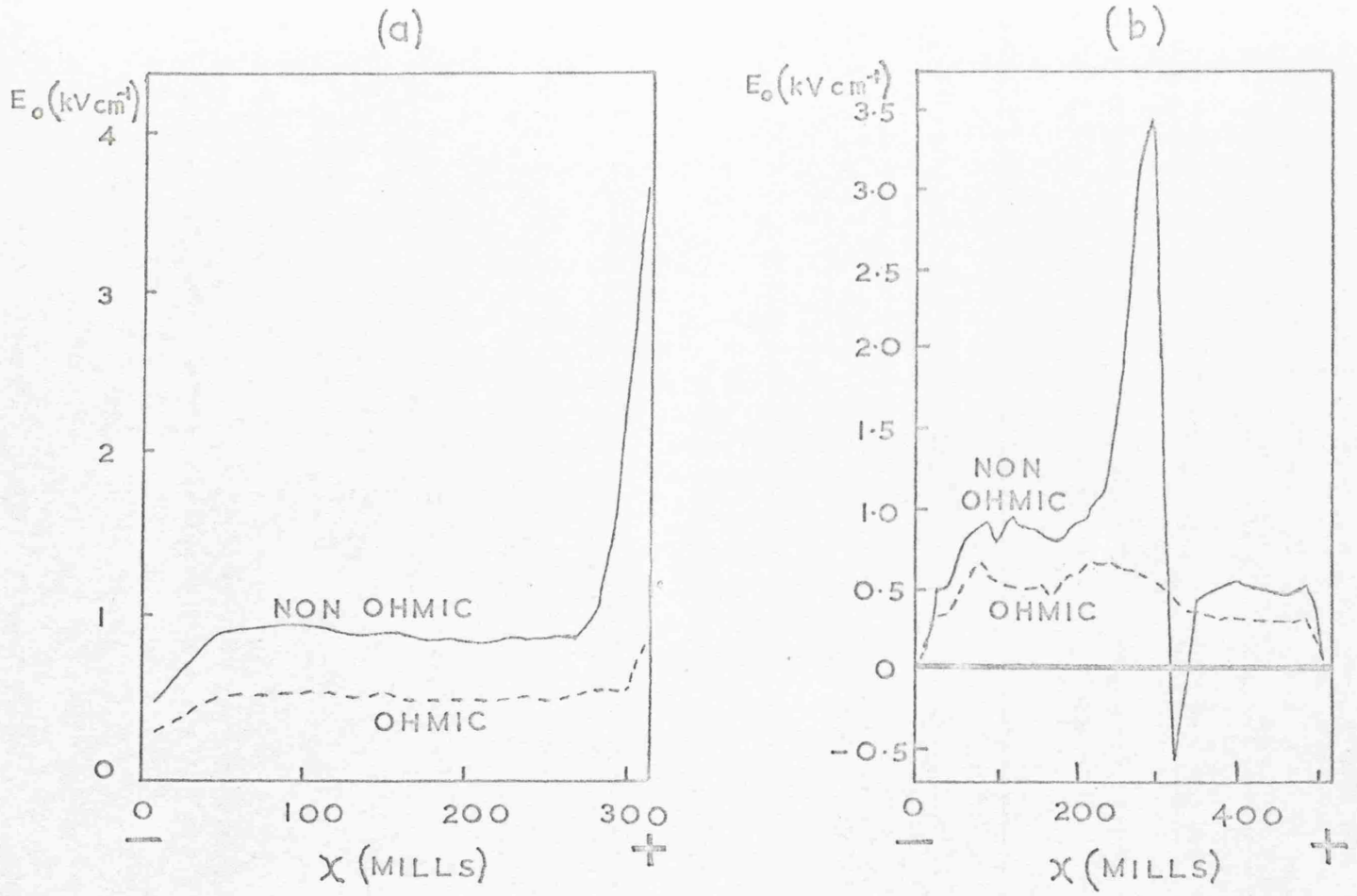

Fig.2.6 (a) and (b) Electric field vs distance from the cathode for a homogeneous and an inhomogeneous sample respectively.

After McFee and Tien (1966).

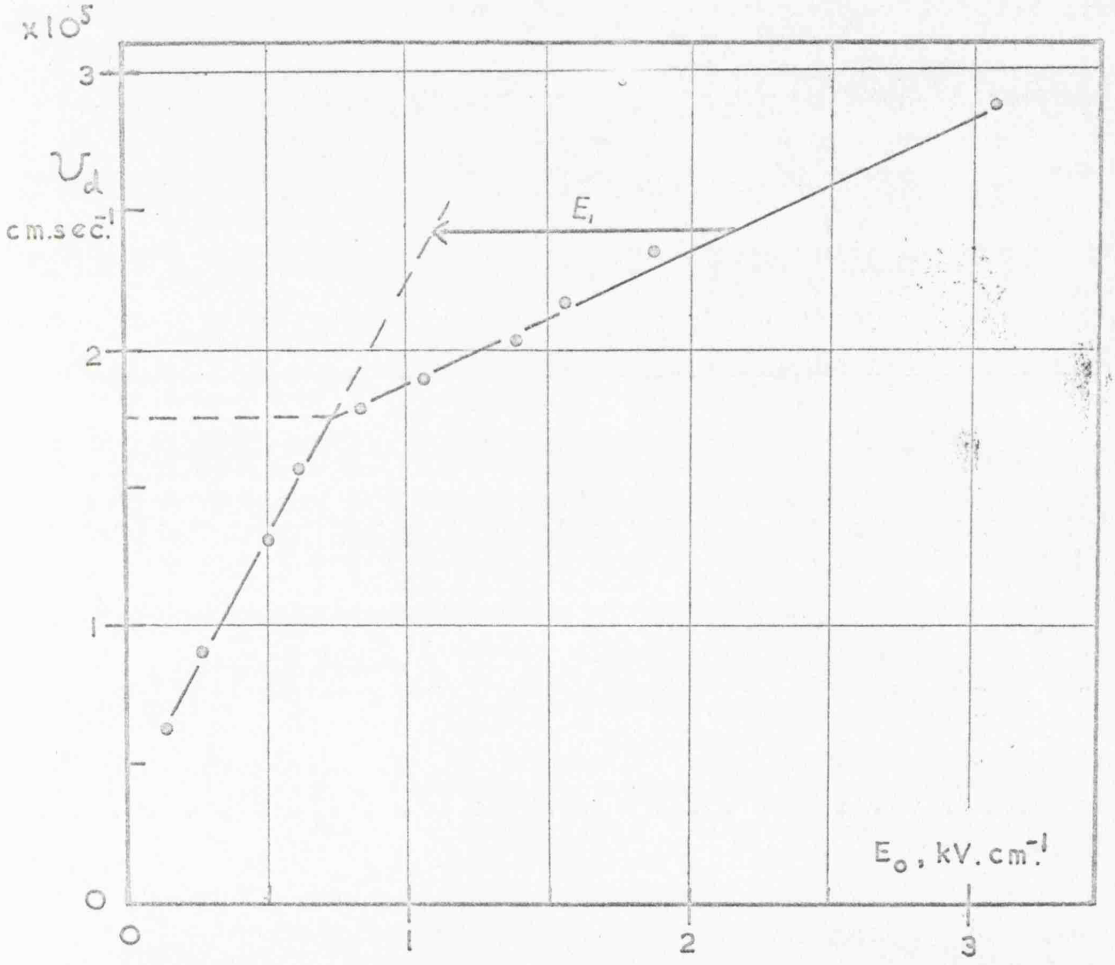

Fig.2.7 Measured electron drift velocity v_d as a function of the applied field E_o. (Shear wave interaction). The discontinuity occurs at $v_d = v_d'$.

After LeComber, Spear and Weinmann (1966).

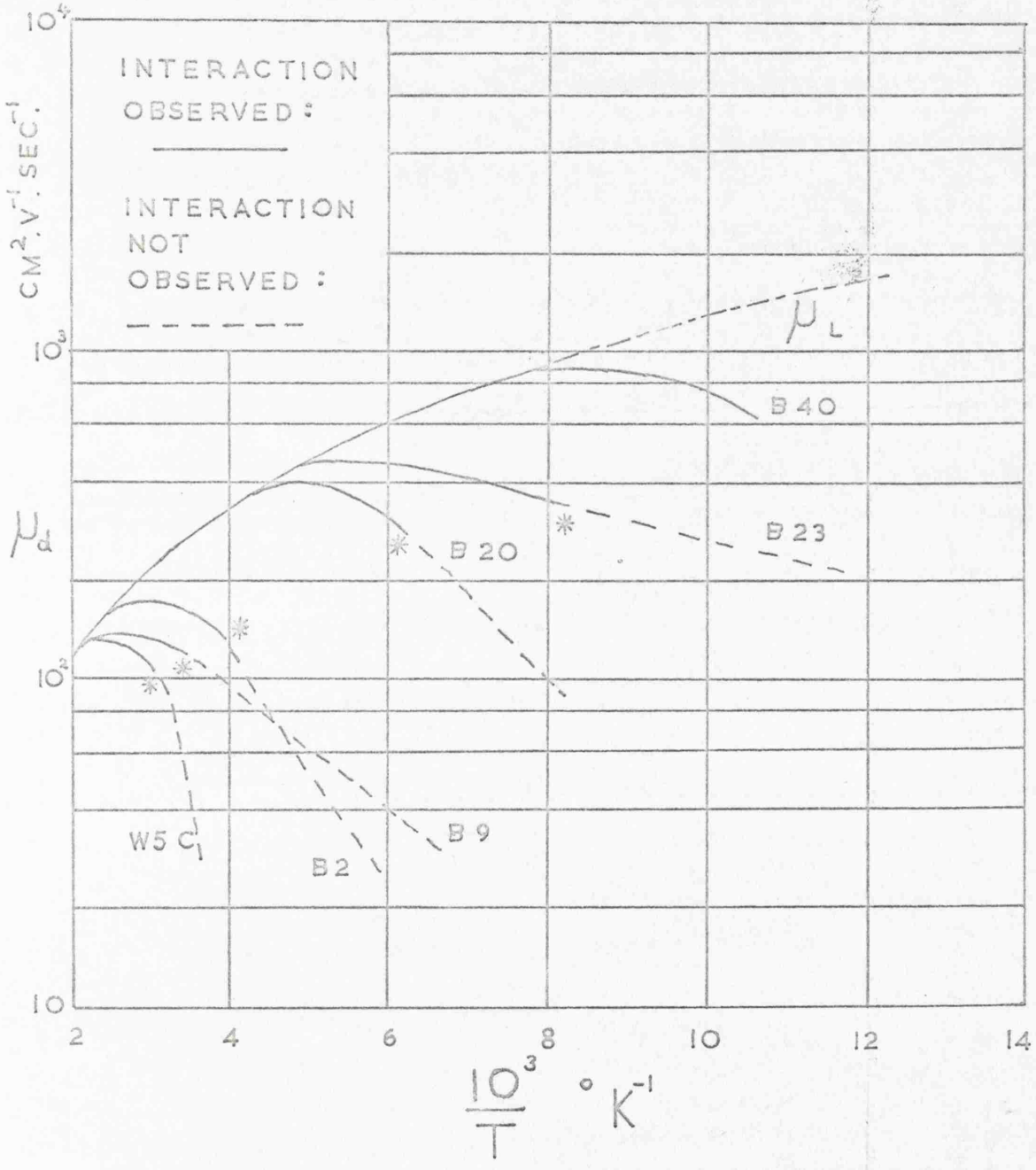

Fig.2.8 Temperature dependence of the electron drift mobility μ_d in six CdS specimens. μ_L denotes the lattice mobility. The asterisk marks the disappearance of the interaction with decreasing temperature. After LeComber, Spear and Weinmann (1966).

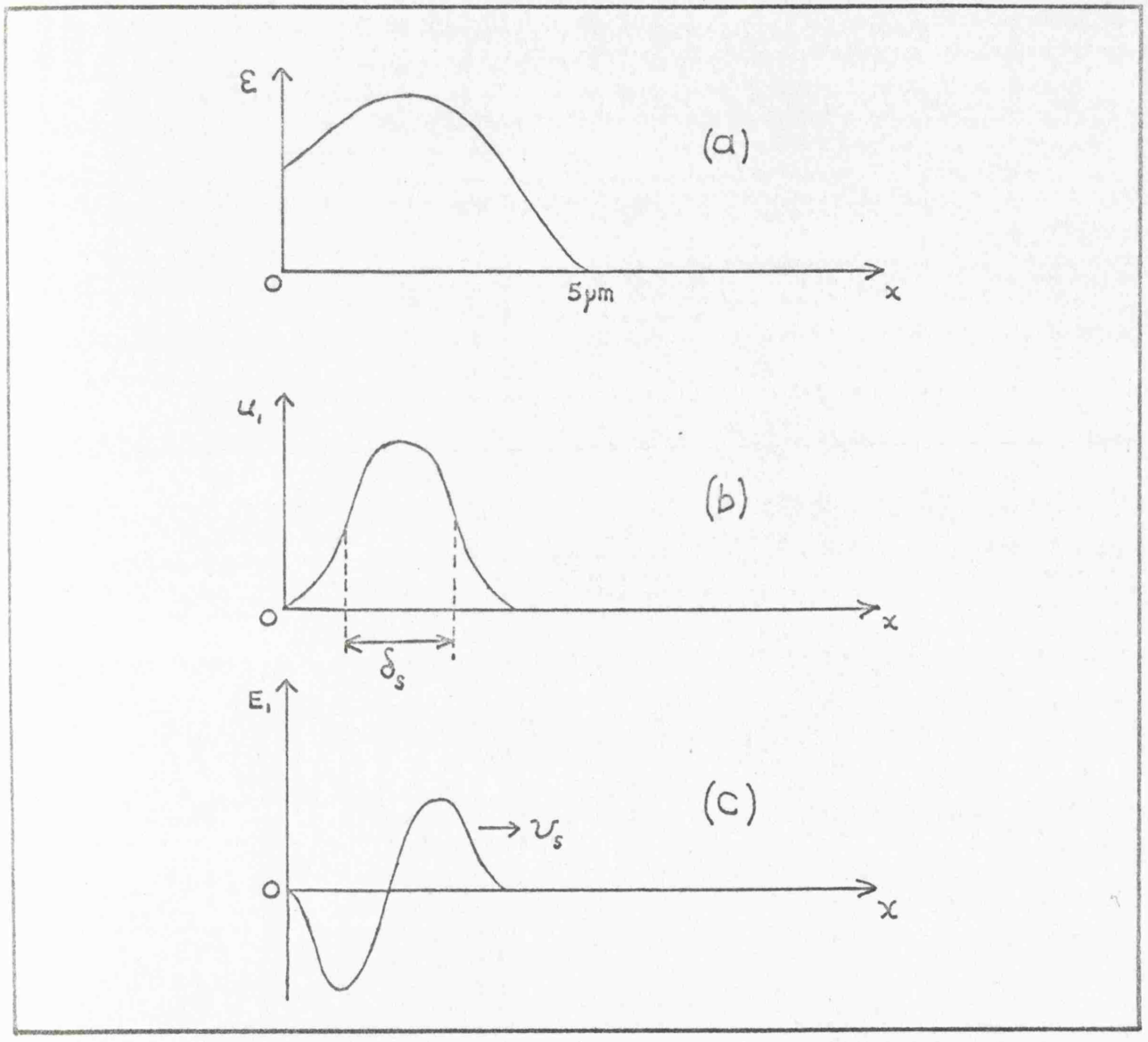

Fig.3.1 Illustration of the model in which the incident electron excitation pulse generates the stress wave. (a) , the energy dissipated per micrometre by the excitation pulse is shown as a function of the distance below the top electrode;
(b) particle displacement u_1 produced by the excitation pulse;
(c) resulting piezoelectric field E_1.
After LeComber, Spear and Weinmann (1966).

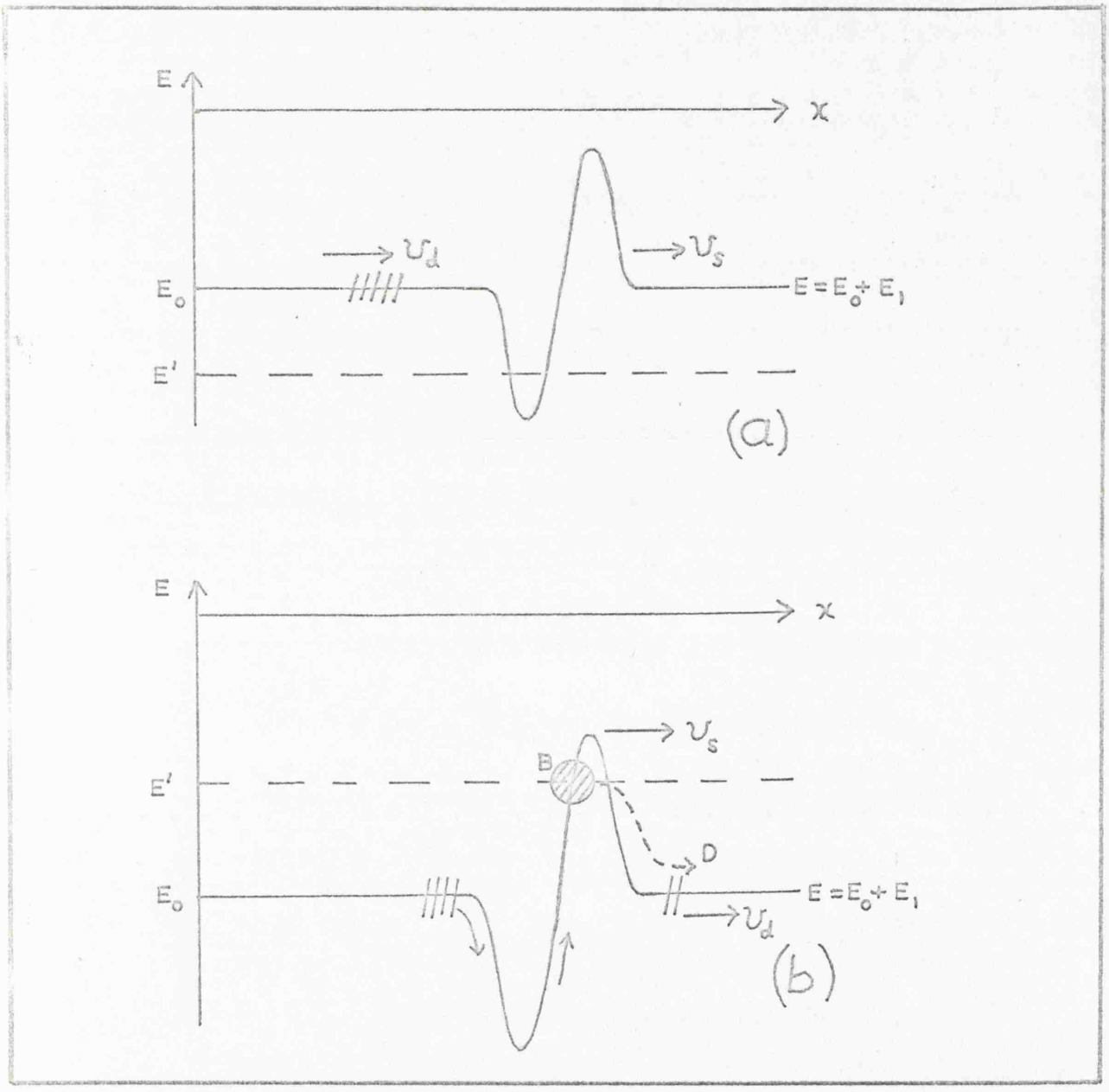

Fig.3.2 Illustration of the interaction between the layer of charge carriers and the piezoelectric field during the transit across the specimen. (a) $E_o < E'$ so that $v_d < v_s$; (b) $E_o > E'$; B is the stable bunching point; D denotes diffusion.

After LeComber, Spear and Weinmann (1966).

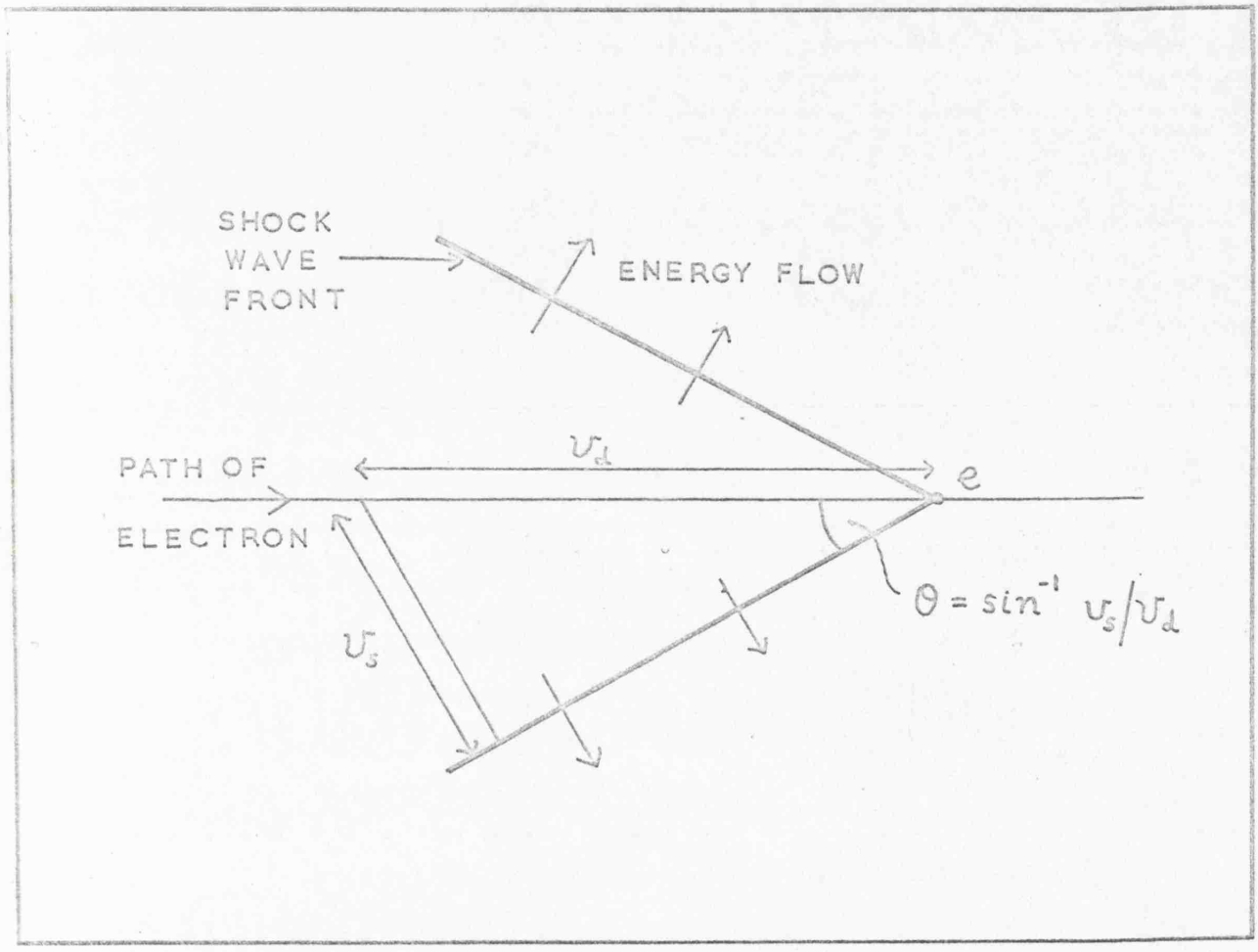

Fig.3.3 Showing the conical shock wave front produced when $v_d > v_s$.

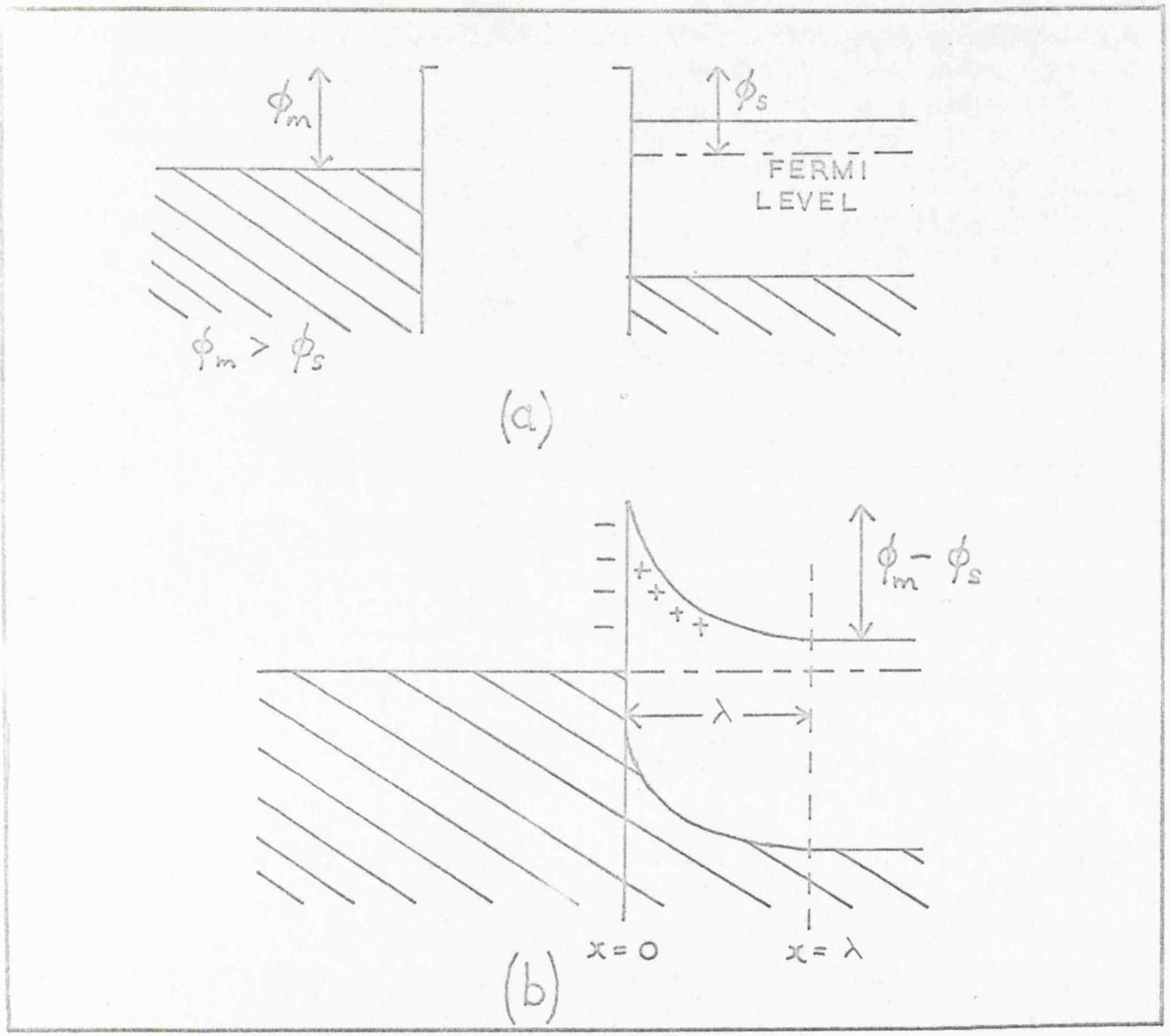

Fig.3.4 (a) and (b). Energy level representation of a contact between a metal and an n-type semiconductor. Fig. (a) and (b) before and after contact respectively, for a metal with a greater work function than that of the semiconductor.

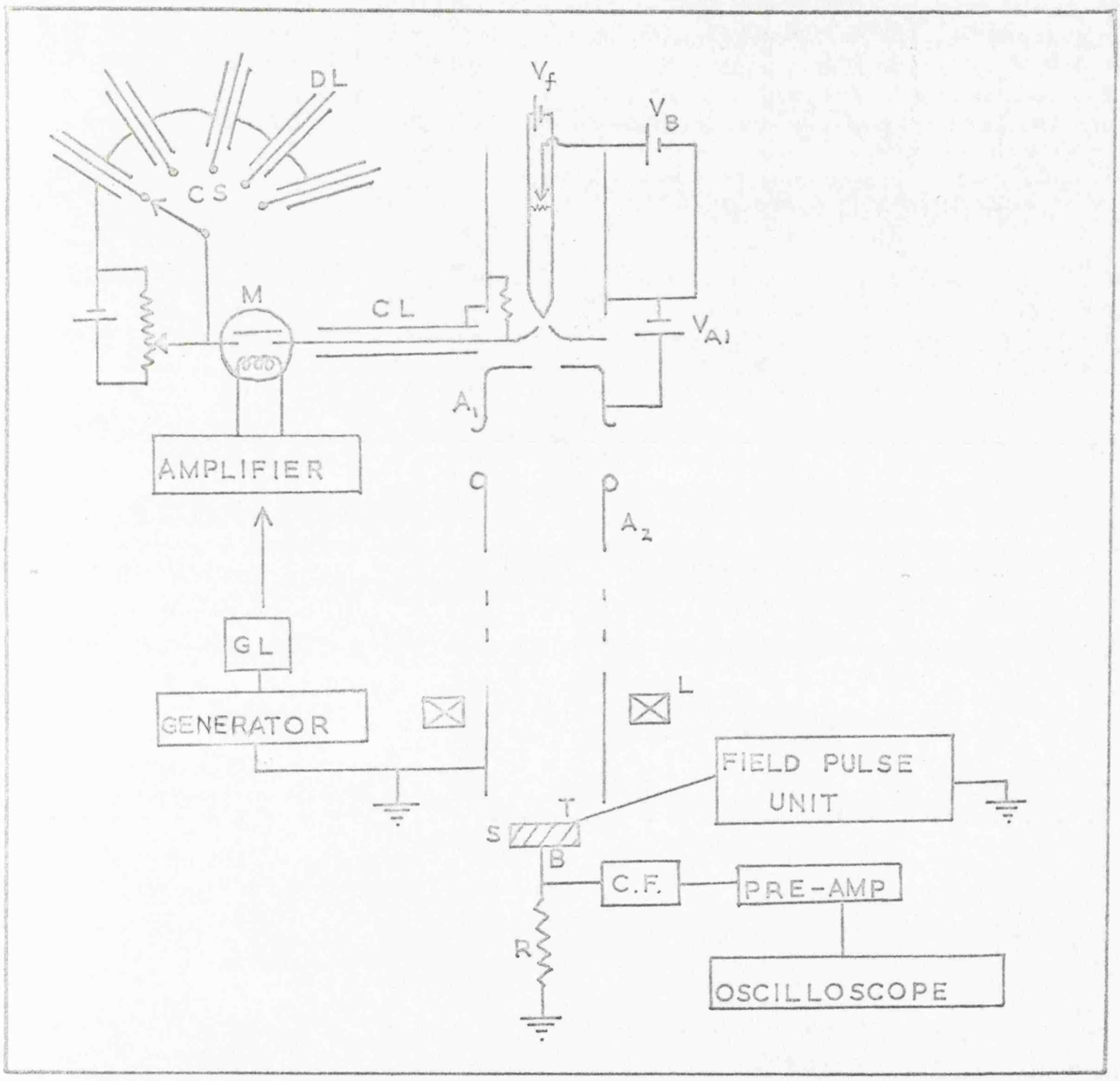

Fig.4.1 Block diagram of the experimental arrangement for electron pulse excitation.

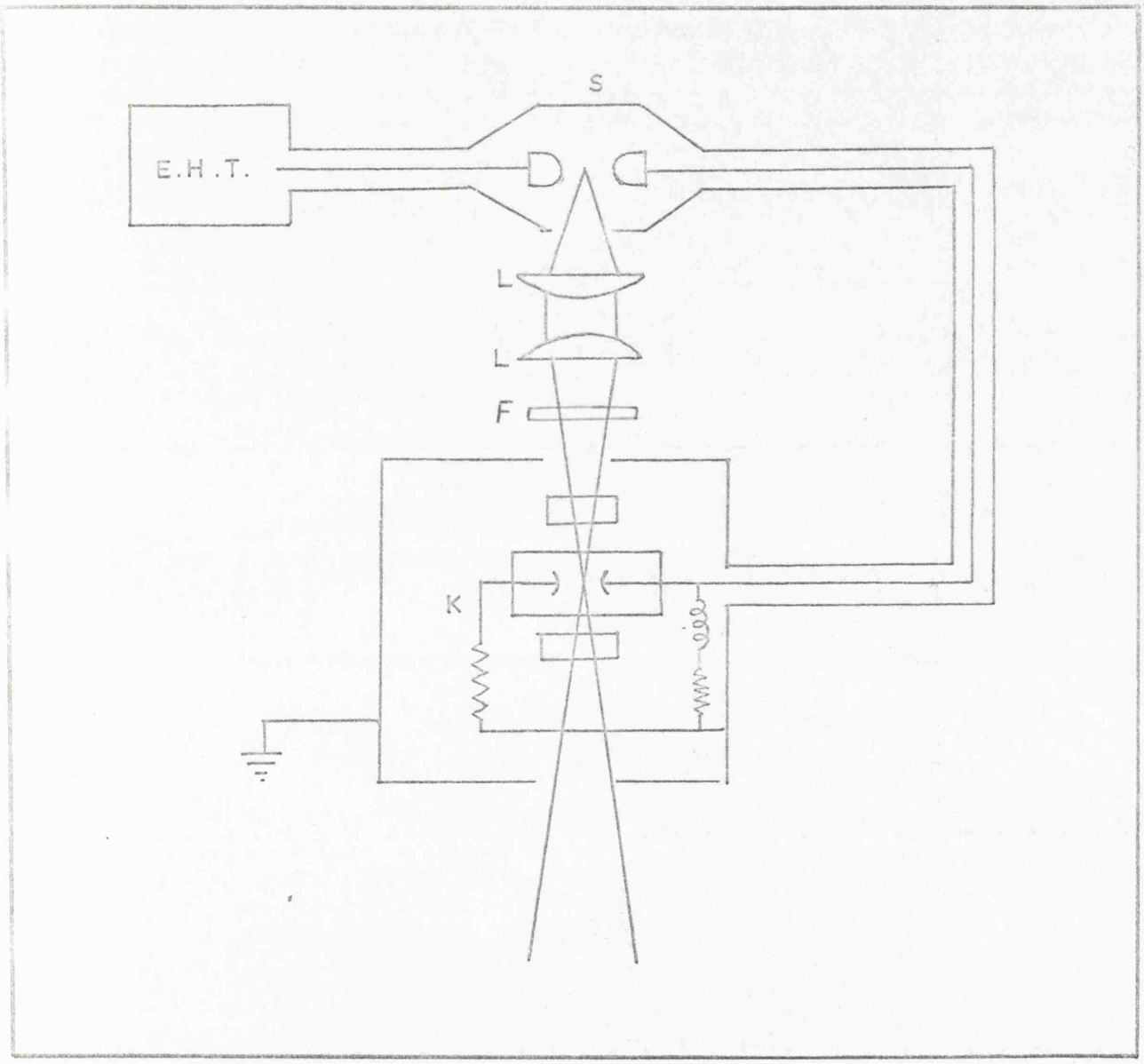

Fig.4.2 Block diagram of the experimental arrangement for light flash excitation.

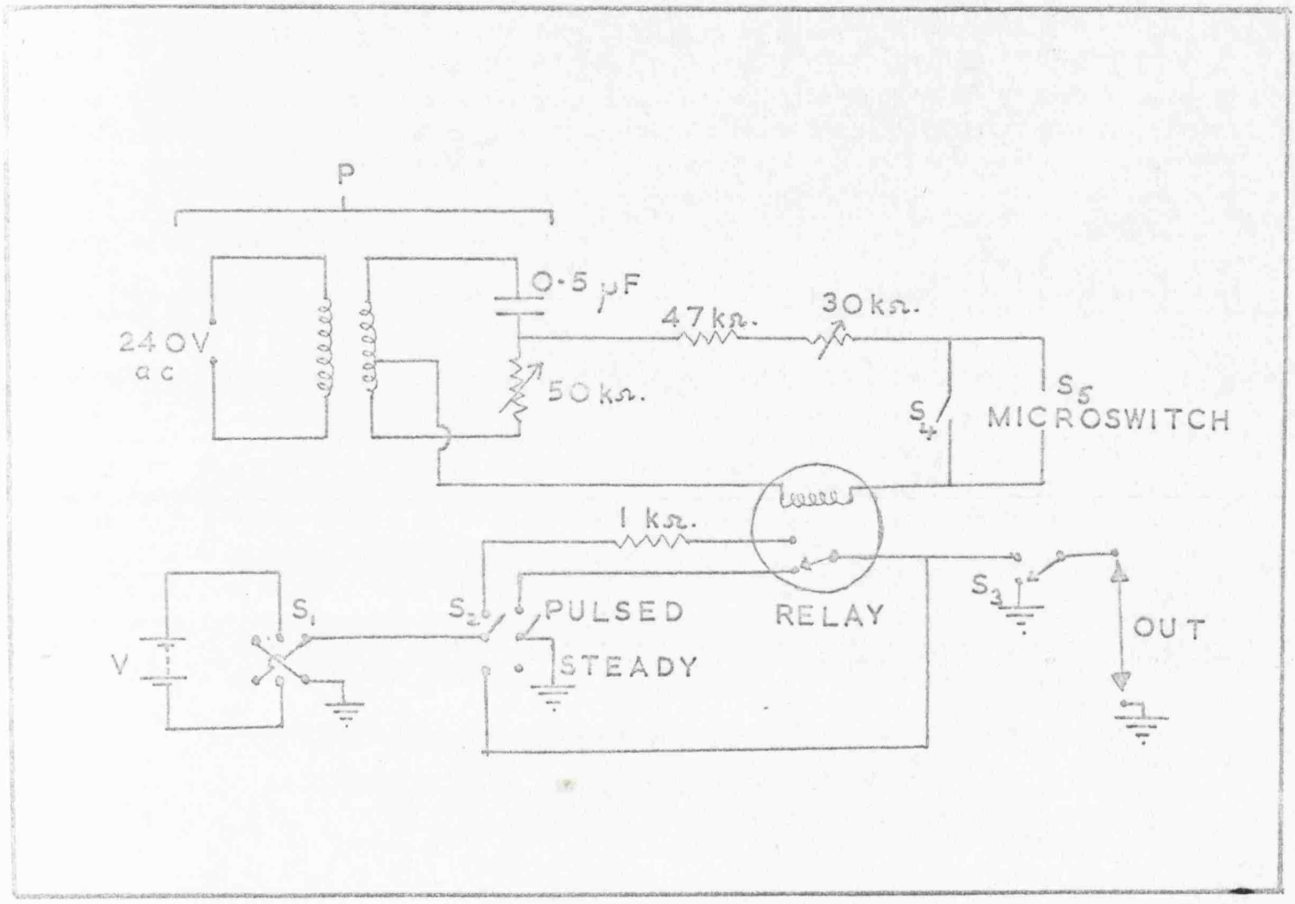

Fig.4.3 Circuit diagram of the millisecond field pulse generator.

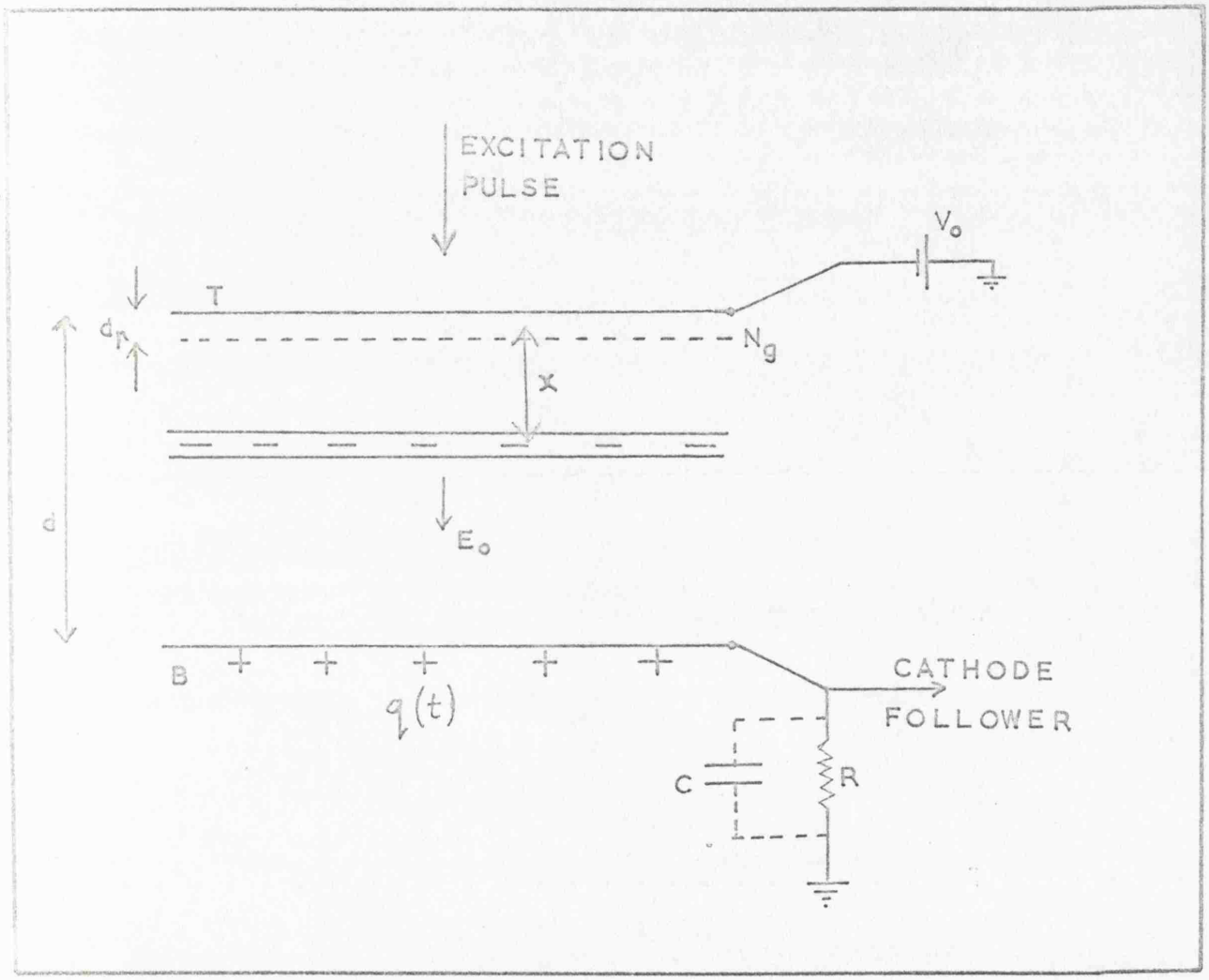

Fig.4.4 Illustrating the principle of charge integration for transit time measurements.

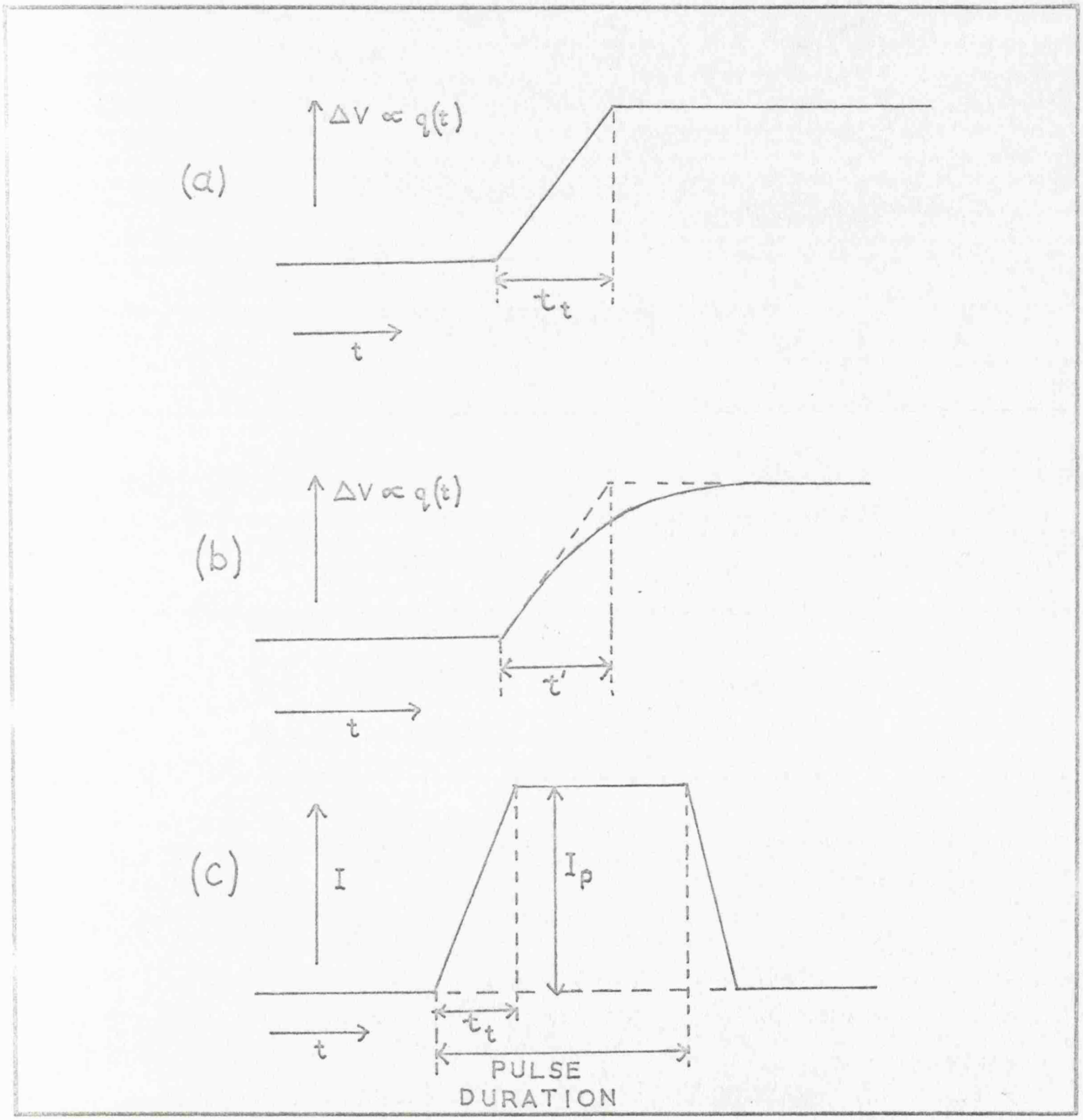

Fig.4.5 (a) Integrated signal of carrier transit expected under ideal conditions.

(b) Integrated signal of carrier transit in presence of deep traps.

(c) Measurement of current pulse height I_p.

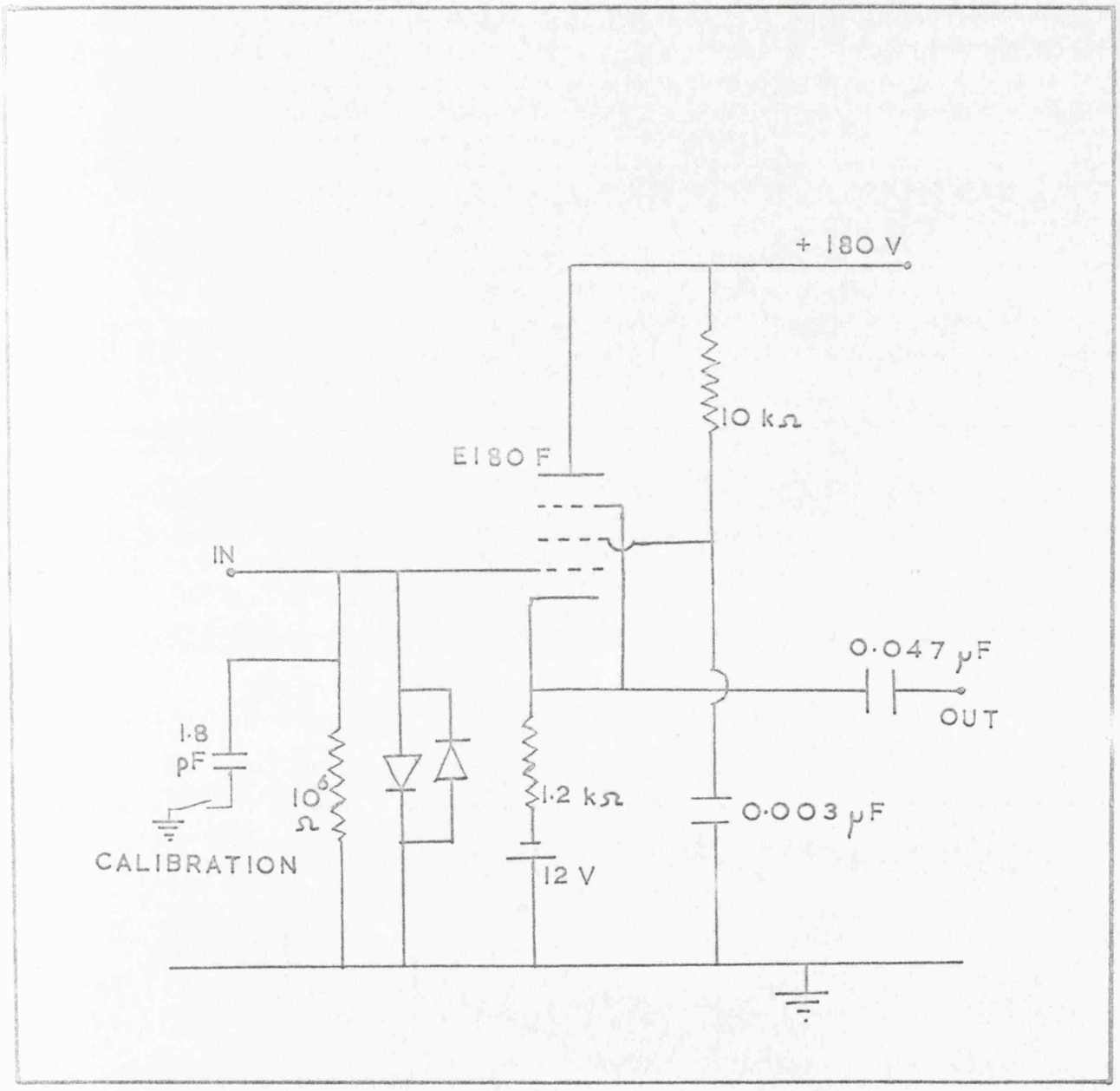

Fig.4.6 Circuit diagram of the cathode follower.

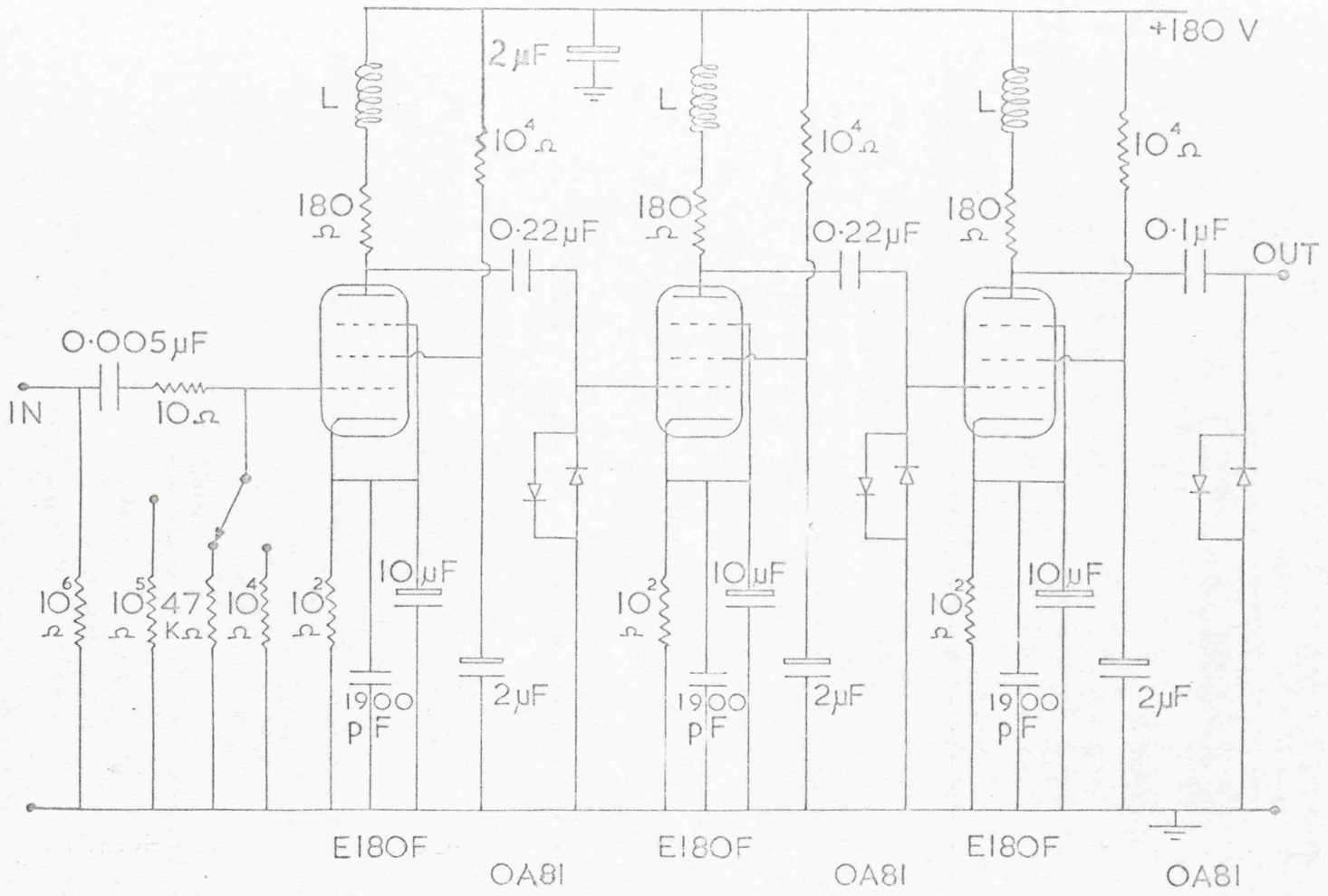

Fig.4.7 Circuit diagram of the wideband preamplifier.

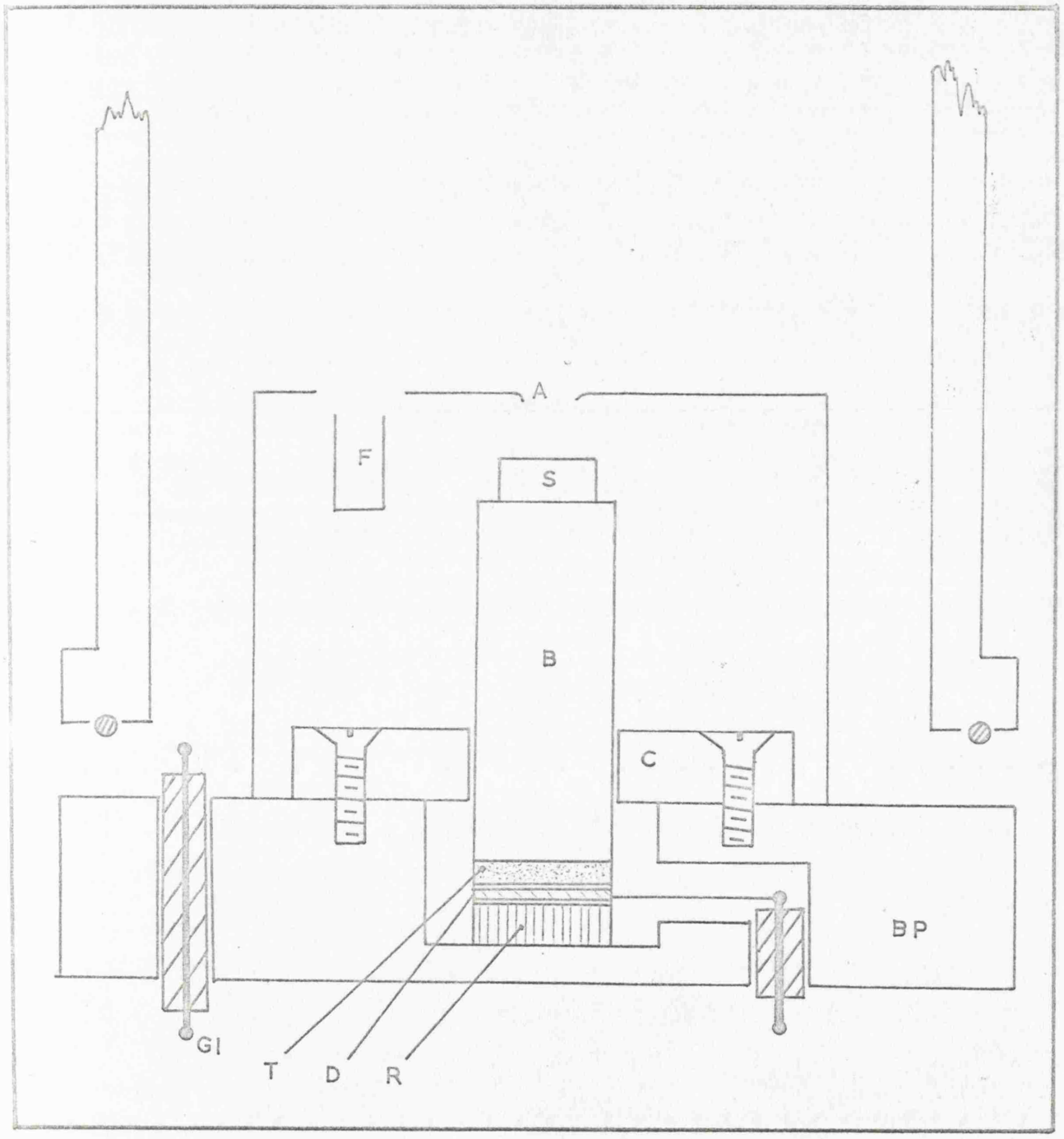

Fig.4.8 Diagram of the Basic Specimen Holder.

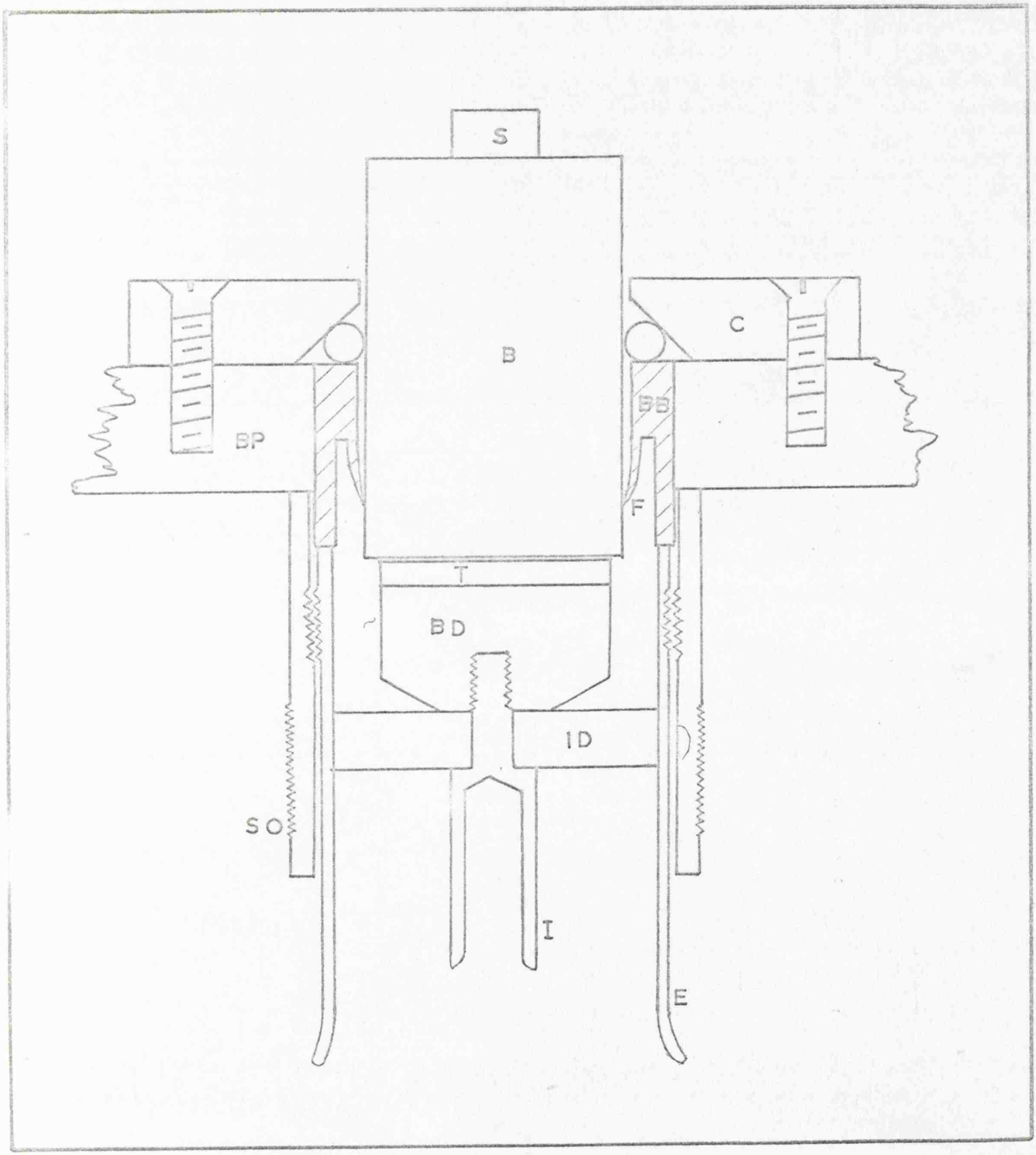

Fig.4.9 Diagram of the Coaxial Holder.

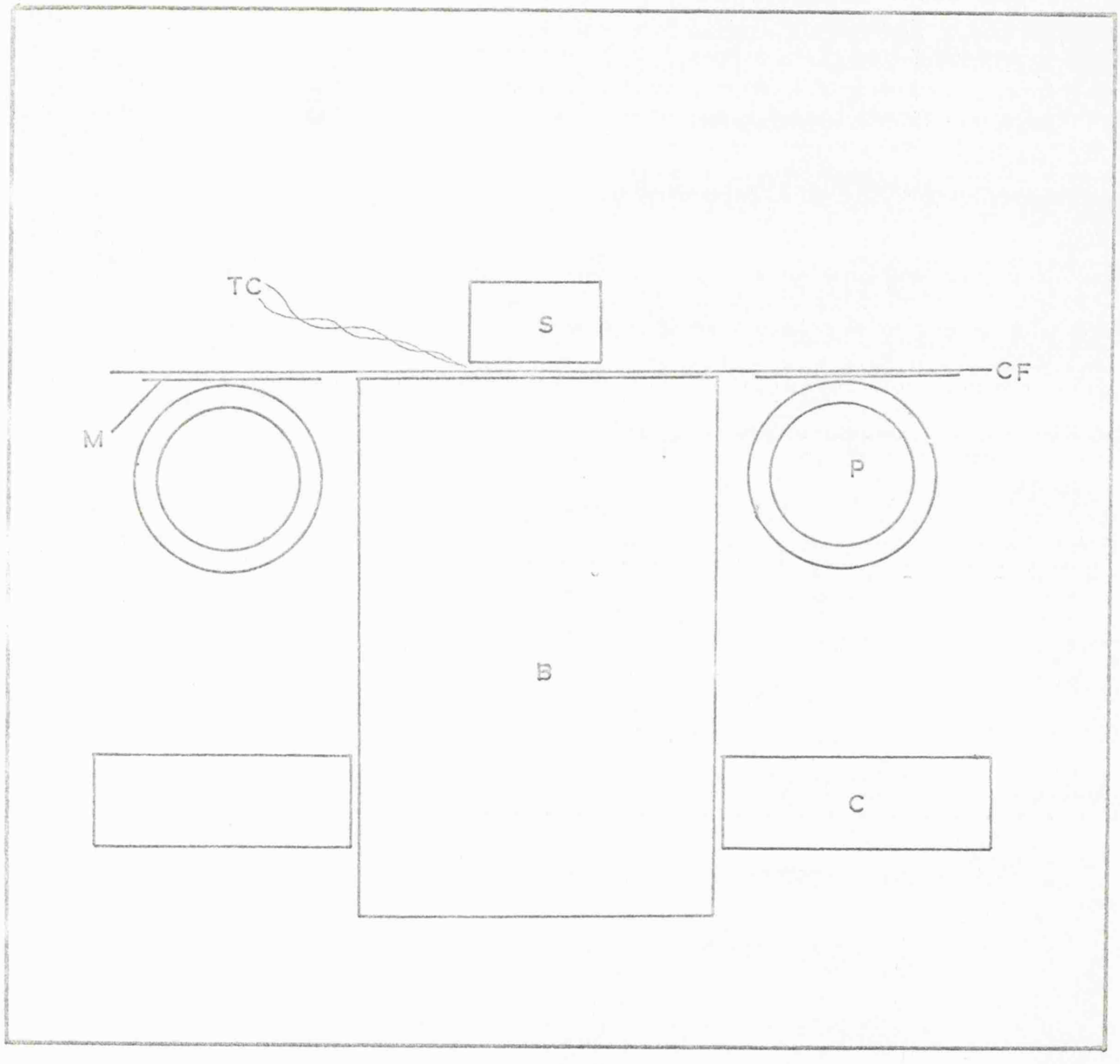

Fig.4.10 Diagram of the cooling arrangement for the Low Temperature Holder.

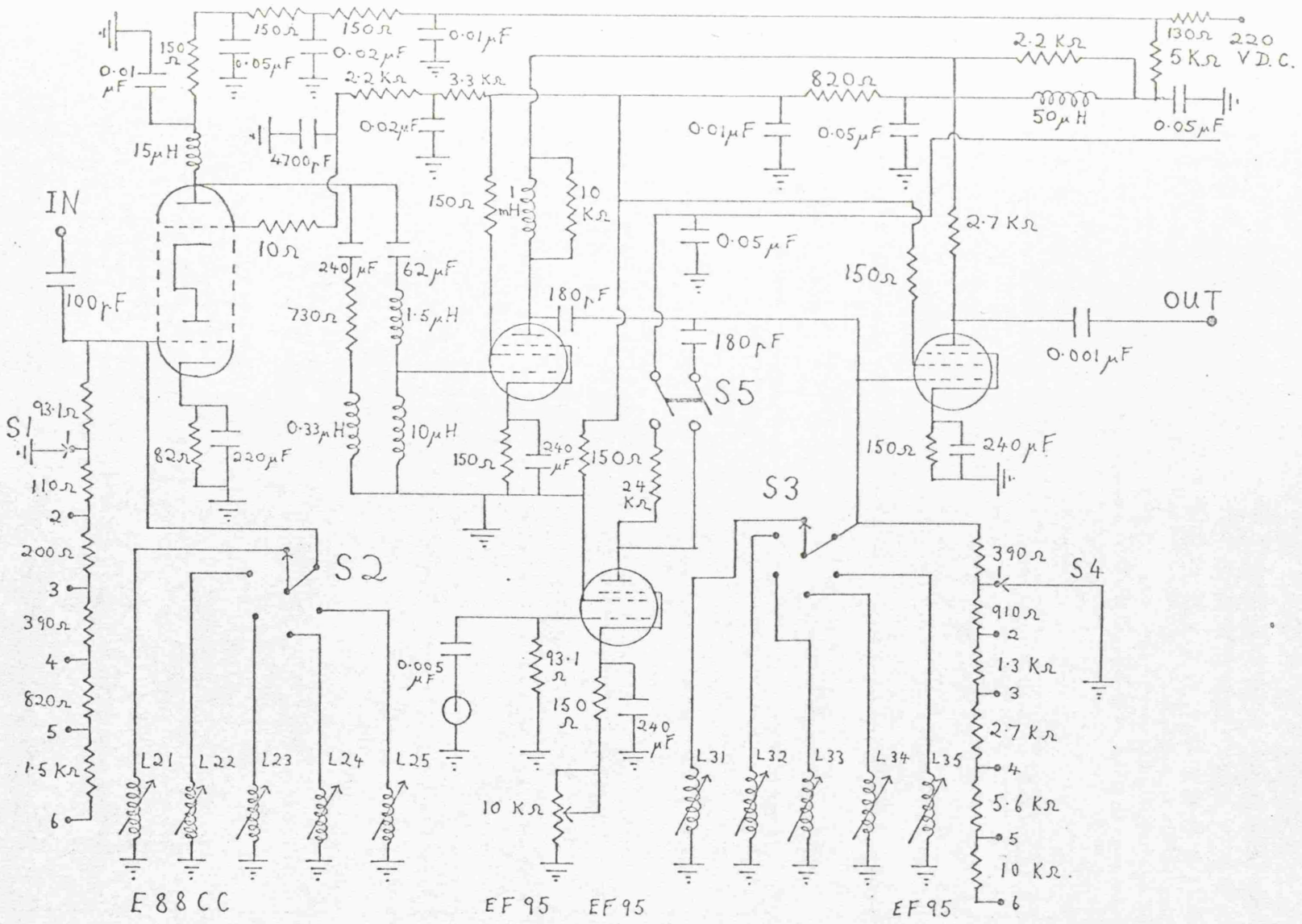

Fig.4.11 Circuit diagram of the tuned preamplifier.

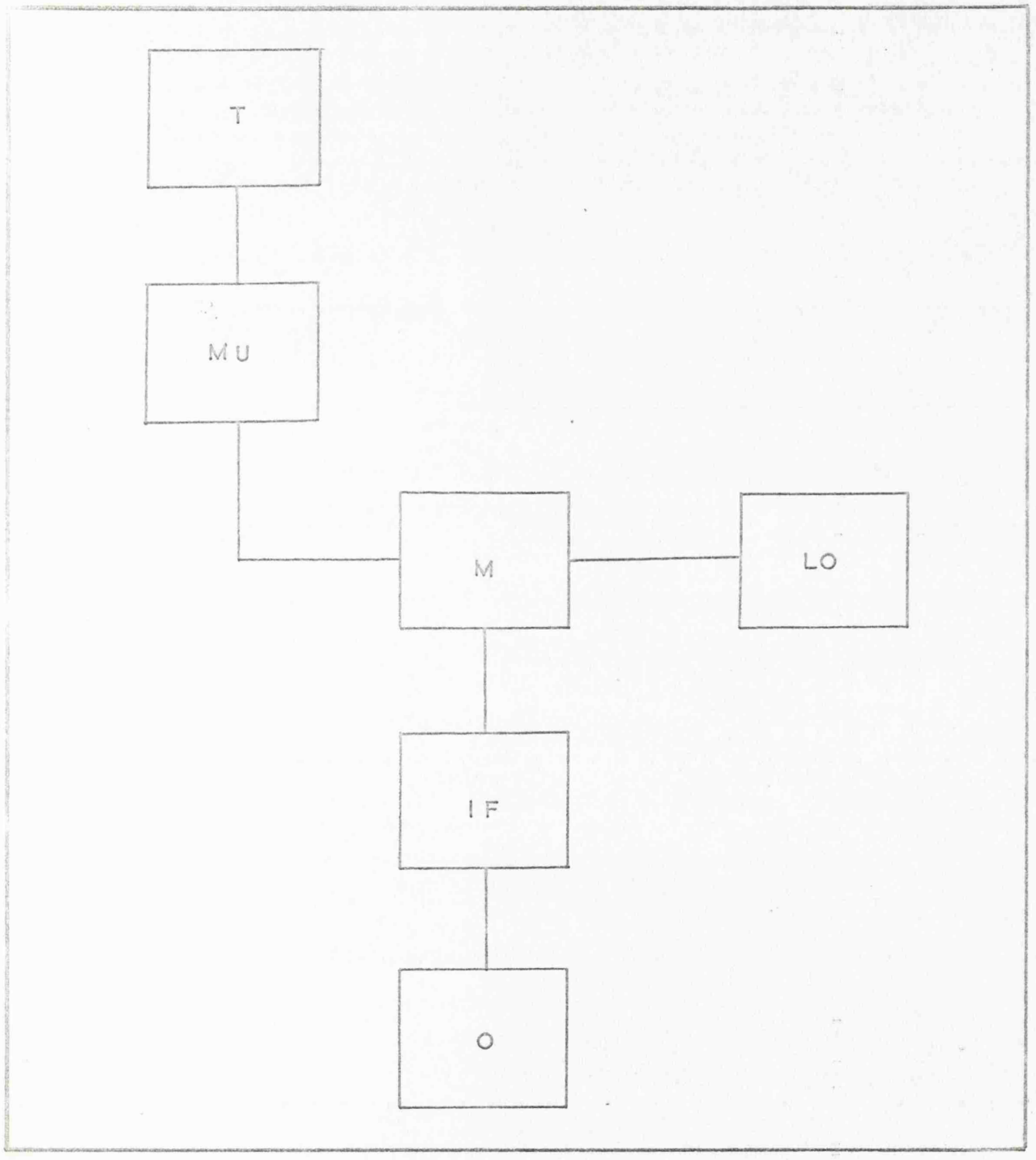

Fig.4.12 Block diagram of Detection Equipment for frequencies above 50 $Mc.sec^{-1}$.

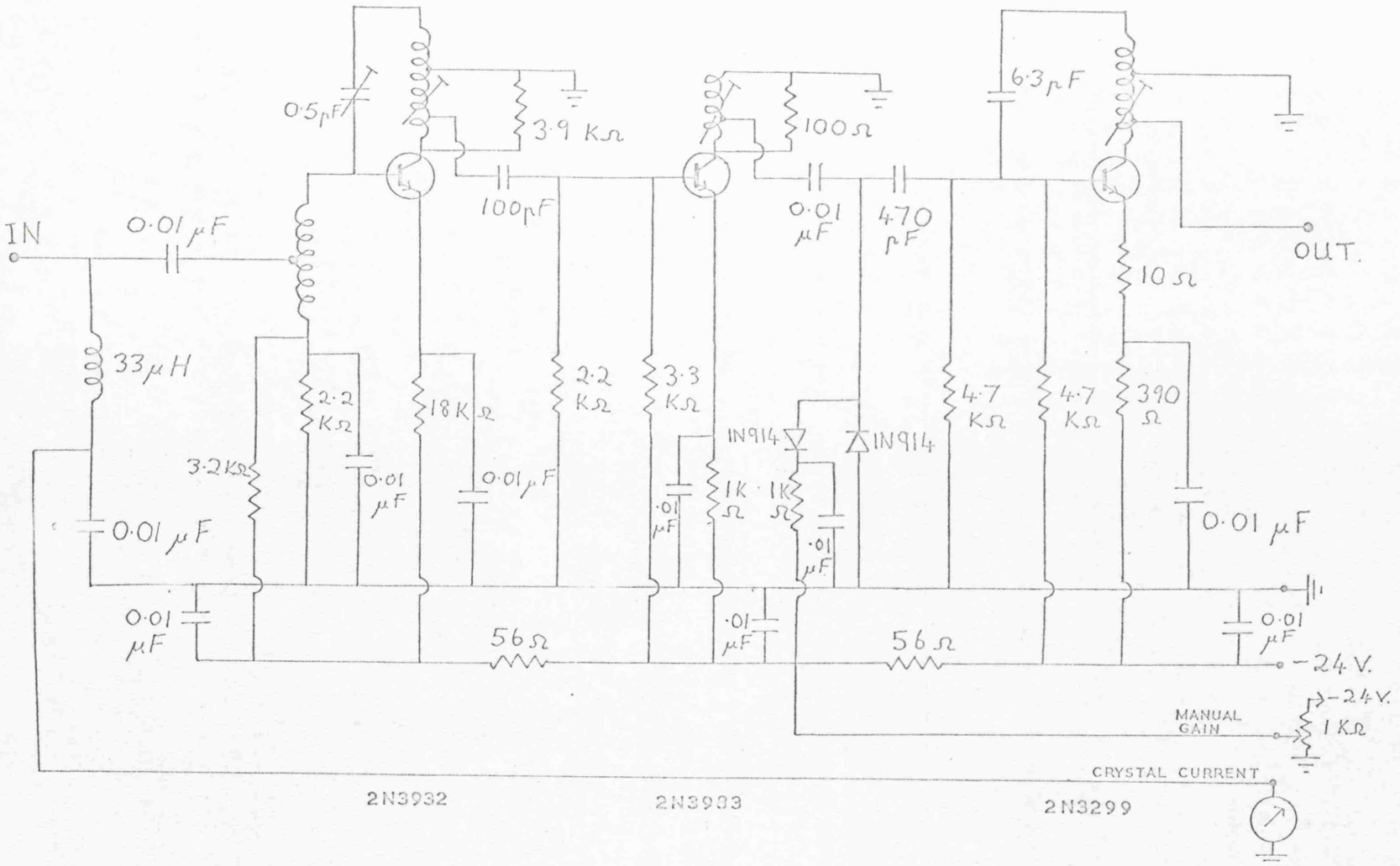

Fig.4.13 Circuit of the 30 Mc/s Intermediate Frequency amplifier.

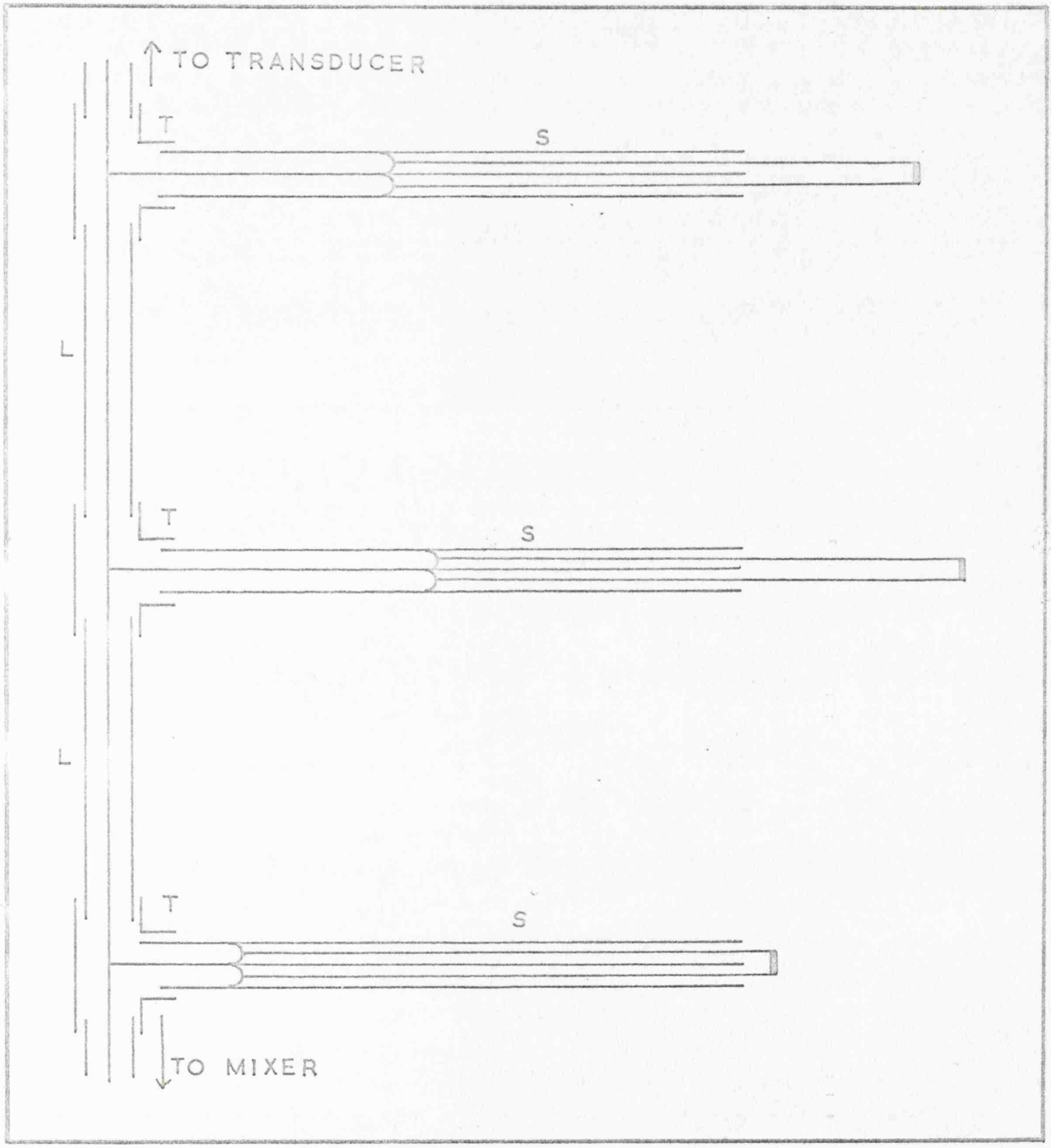

Fig.4.14 Diagram of the Triple-Stub Matching Unit.

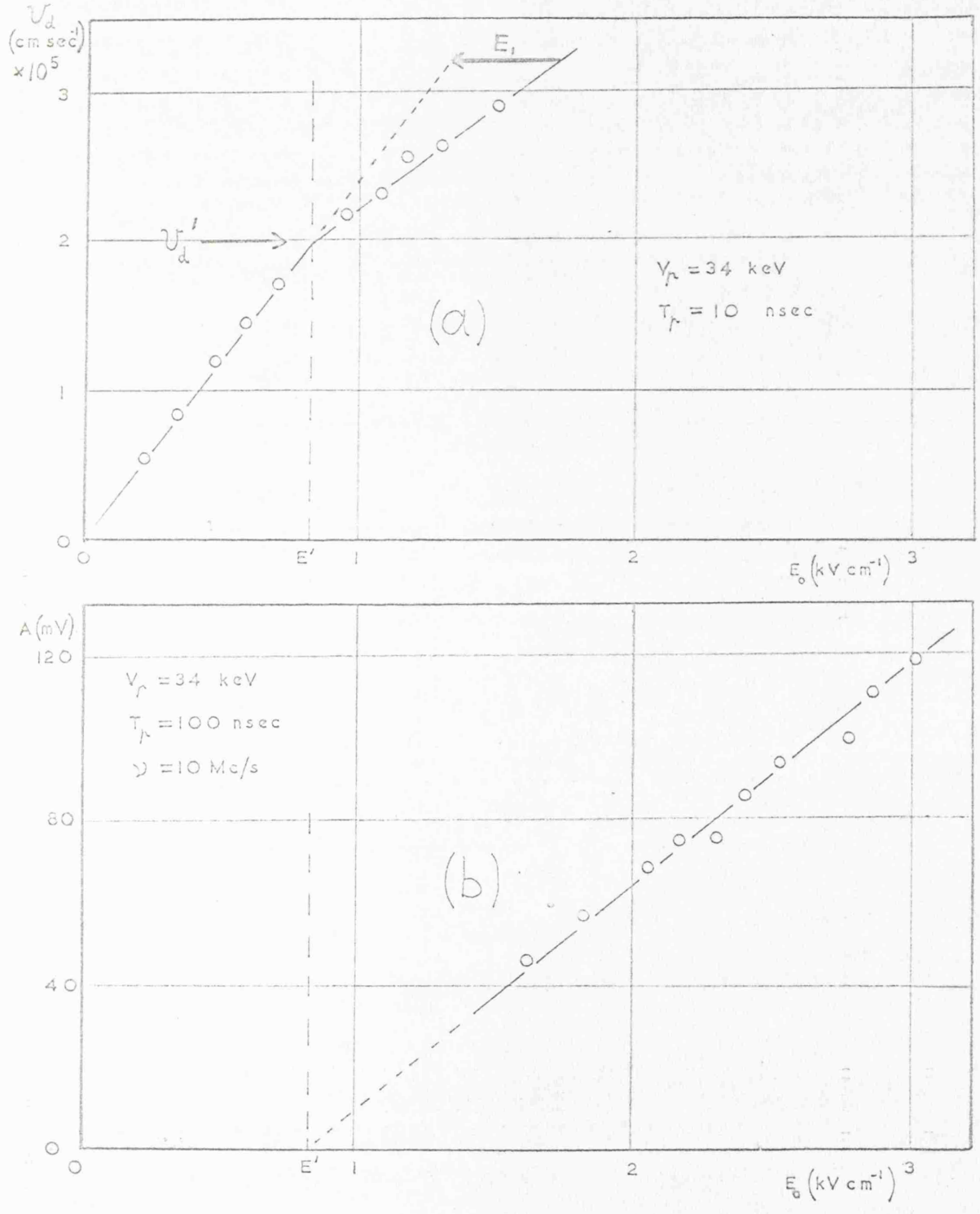

Fig.5.1 (a) and (b) Measured electron drift velocity v_d and stress wave amplitude A as a function of the applied field E_o (Shear wave interaction).

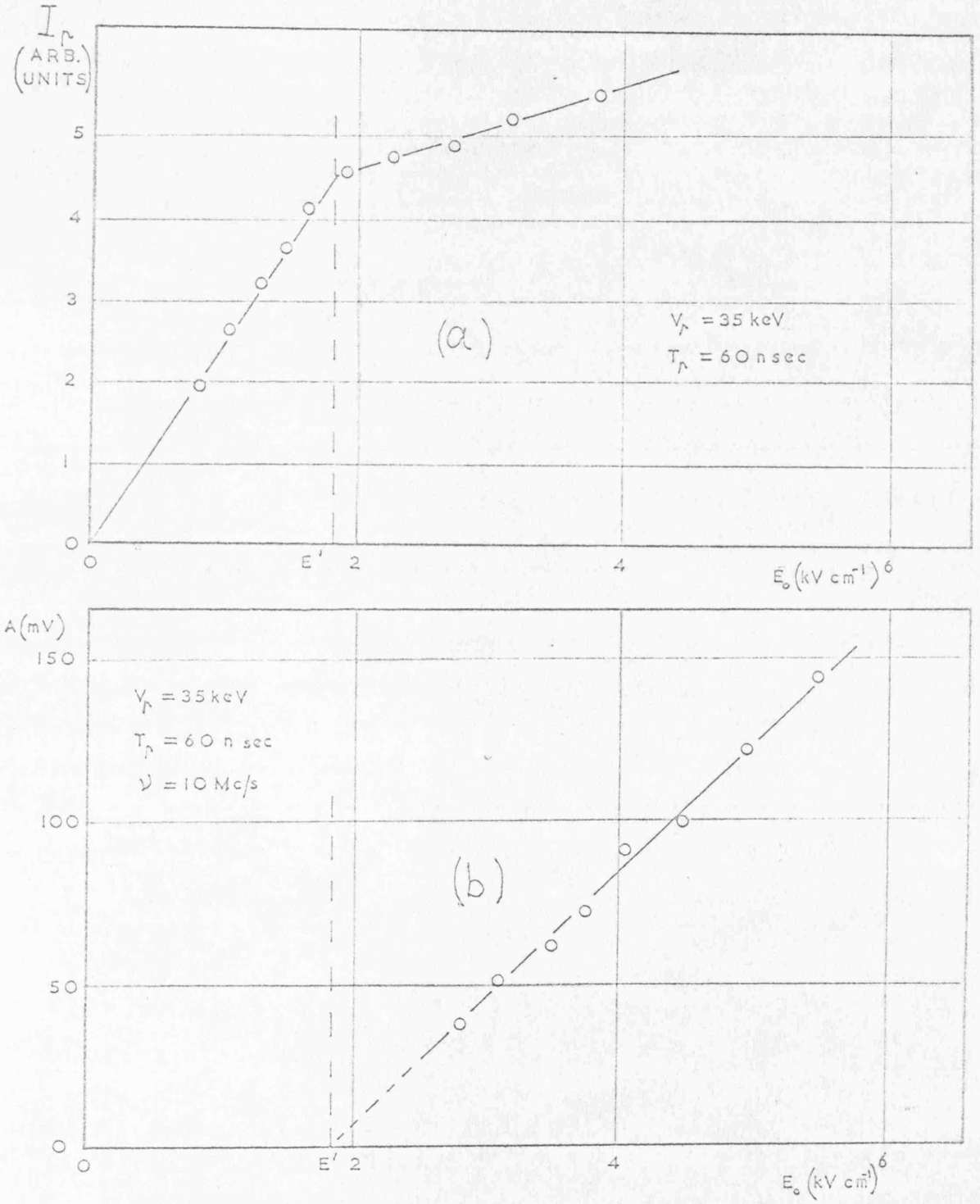

Fig.5.2 (a) and (b) Measured current pulse height I_p and stress wave amplitude A as a function of the applied field E_o (Longitudinal wave interaction).

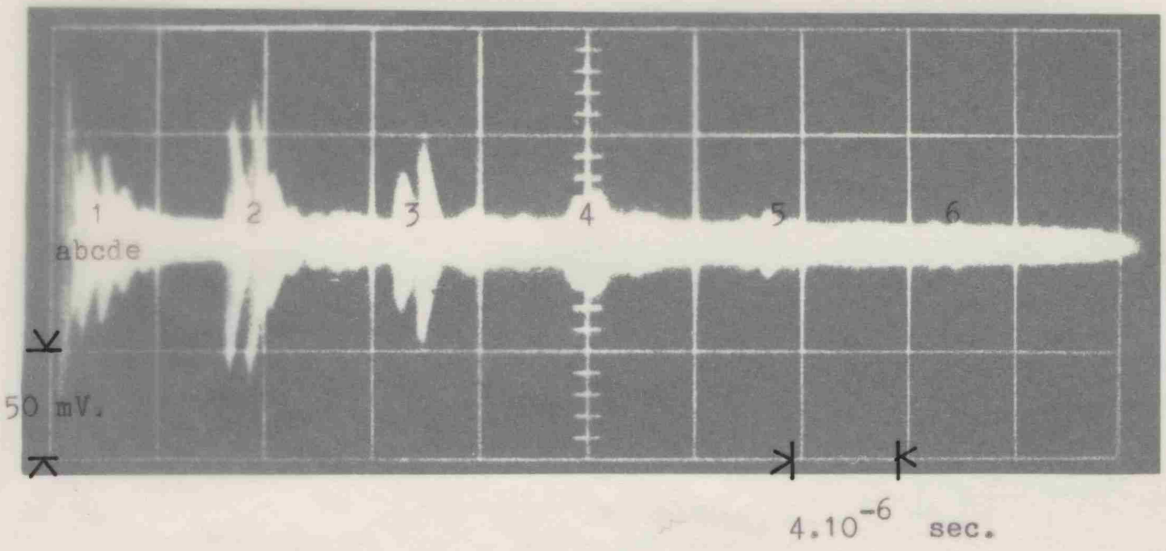

Fig. 5.3 (a)

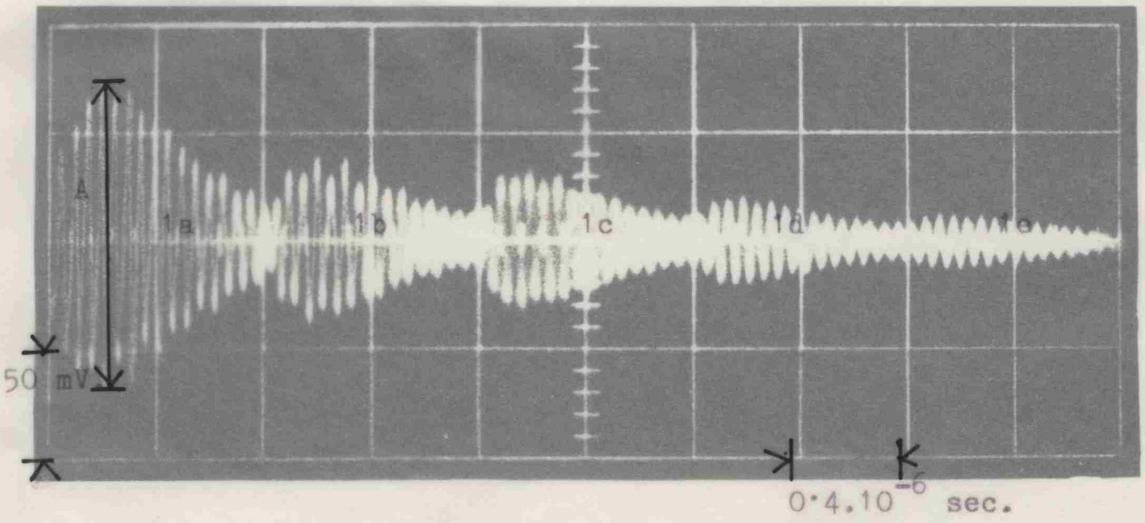

Fig. 5.3 (b)

Fig. 5.3 (a) and (b) Showing the observed ultrasonic signal (19 Mc/s). The labelling of the pulses is explained in the text.

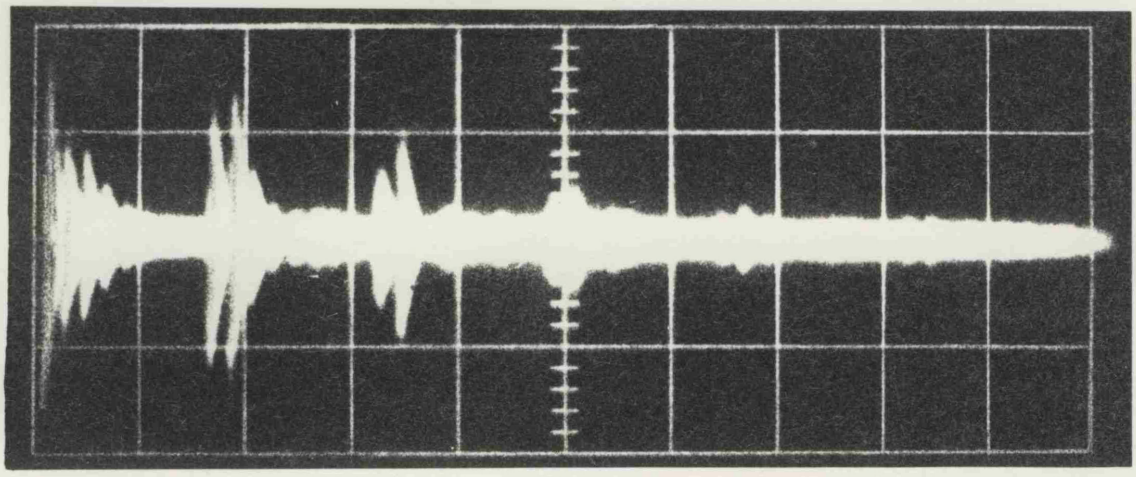

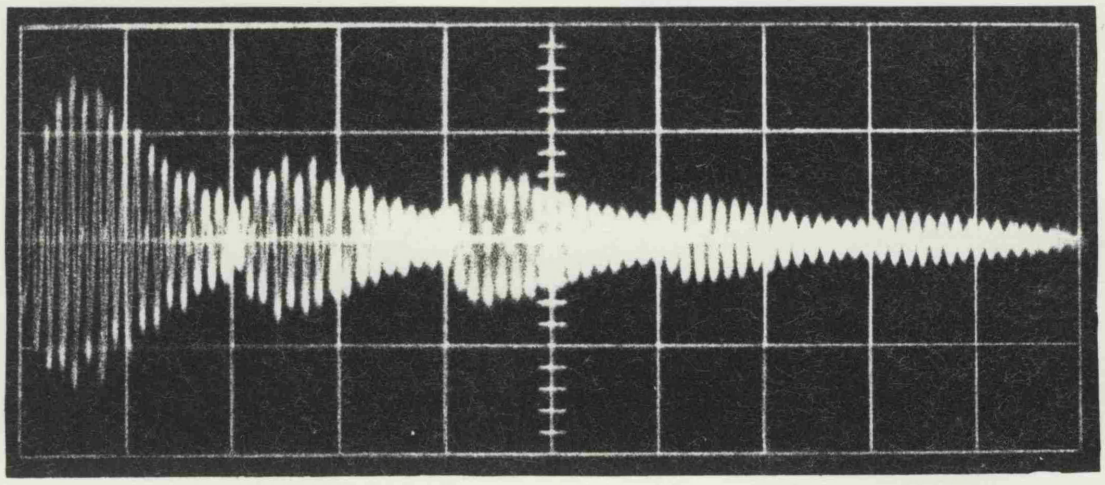

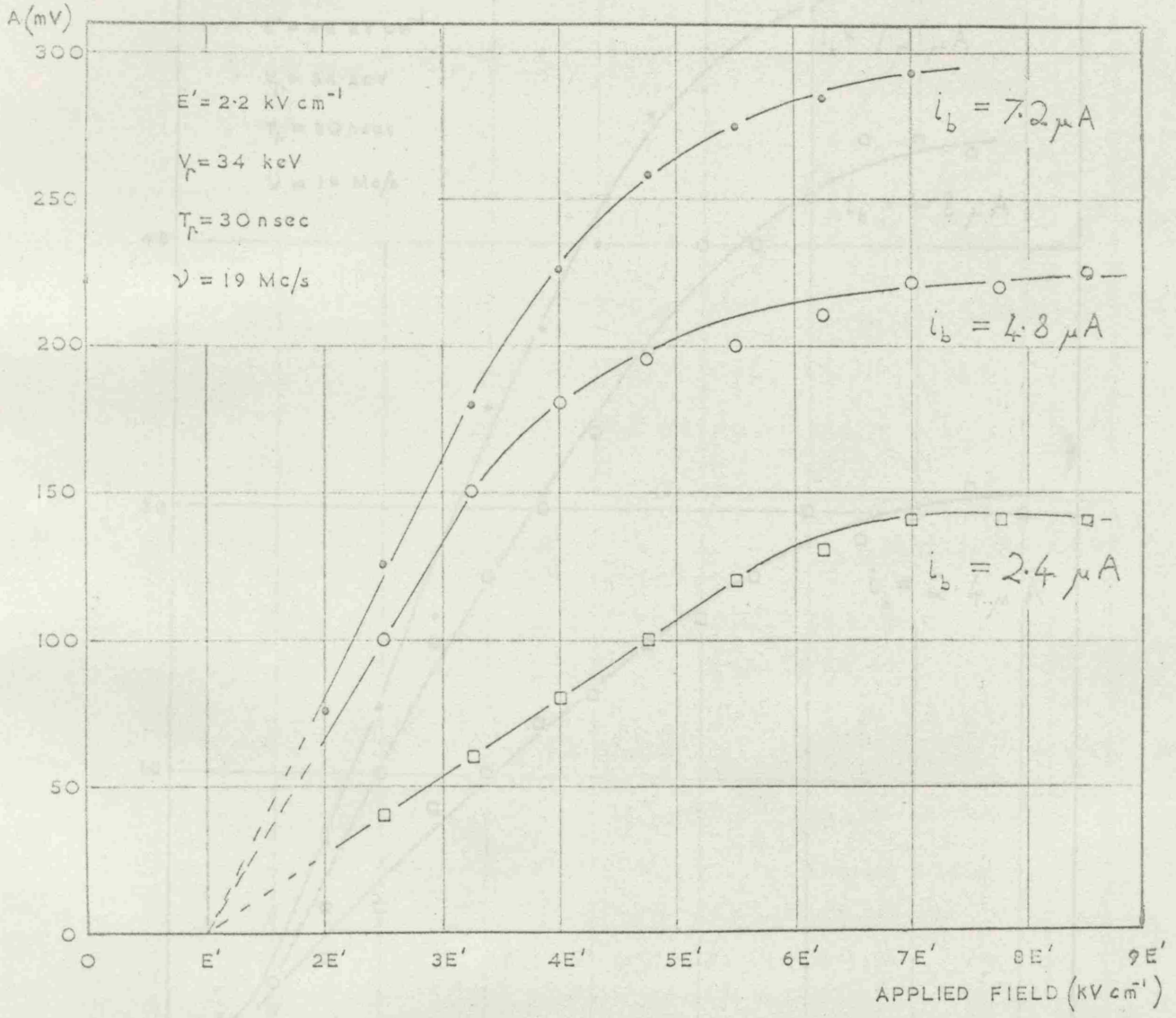

Fig.5.4 Measured stress wave amplitude A as a function of E_o for different values of the beam current.

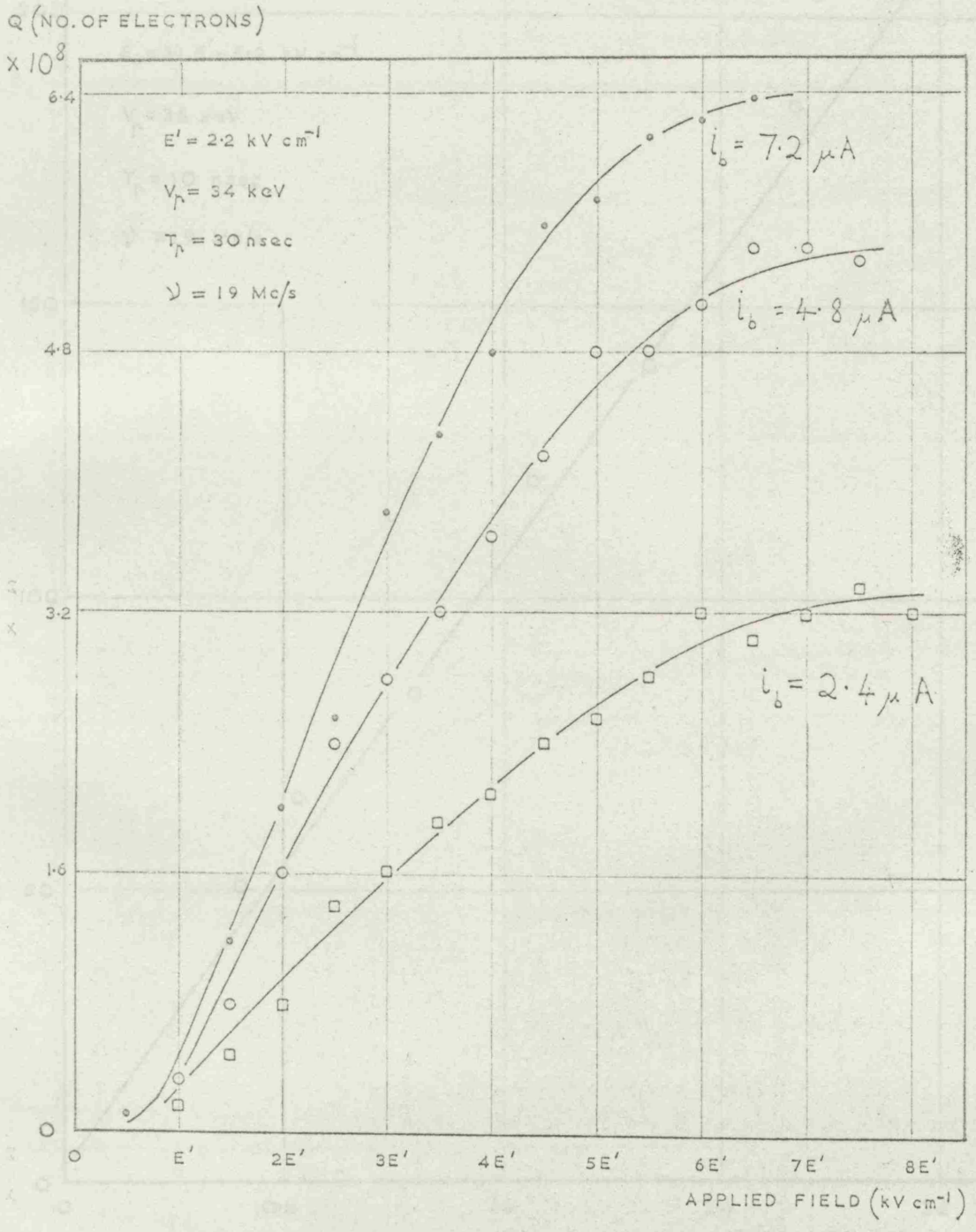

Fig.5.5 Showing the dependence of Q on E_o for different values of the beam current i_b.

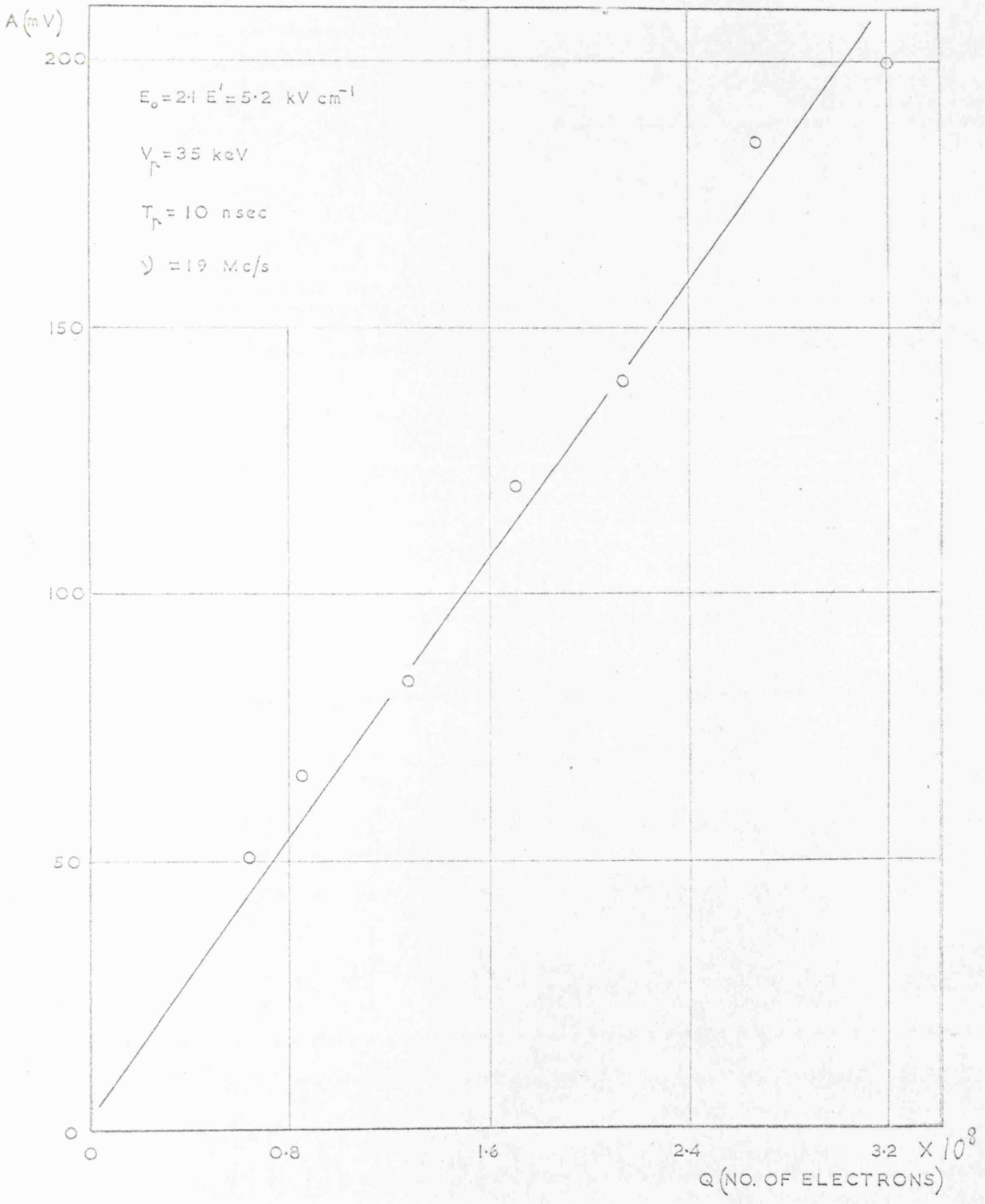

Fig.5.6 Measured stress wave amplitude A as a function of the number of drifting electrons Q.

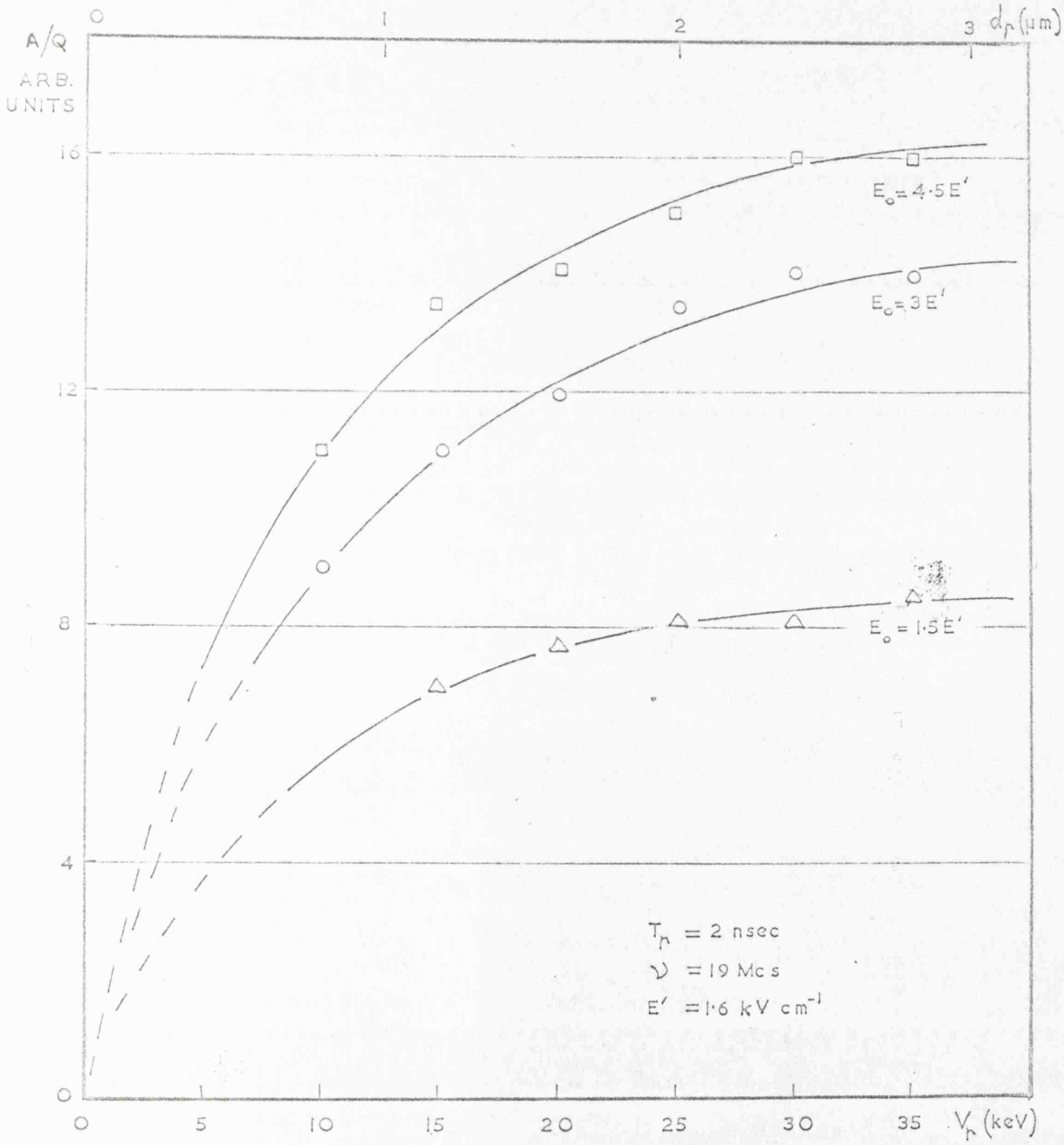

Fig.5.7 Showing the dependence of A/Q on the incident electron energy V_p and the depth d_p below the surface of the half-width of the distribution, for different applied fields E_o.

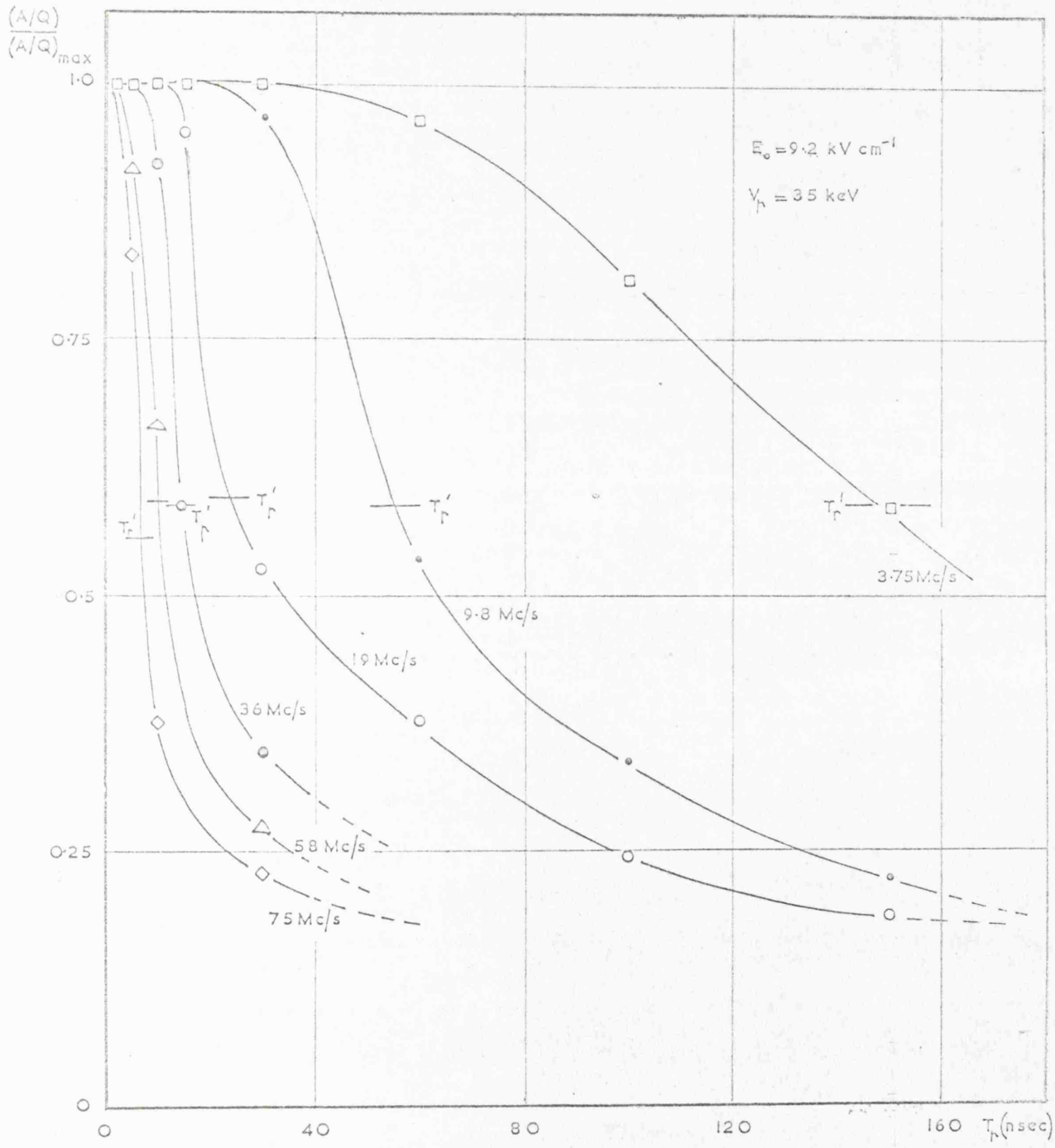

Fig.5.8 Measured stress wave amplitude $(A/Q) / (A/Q)_{max}$ as a function of excitation pulse duration T_p, for six different frequencies.

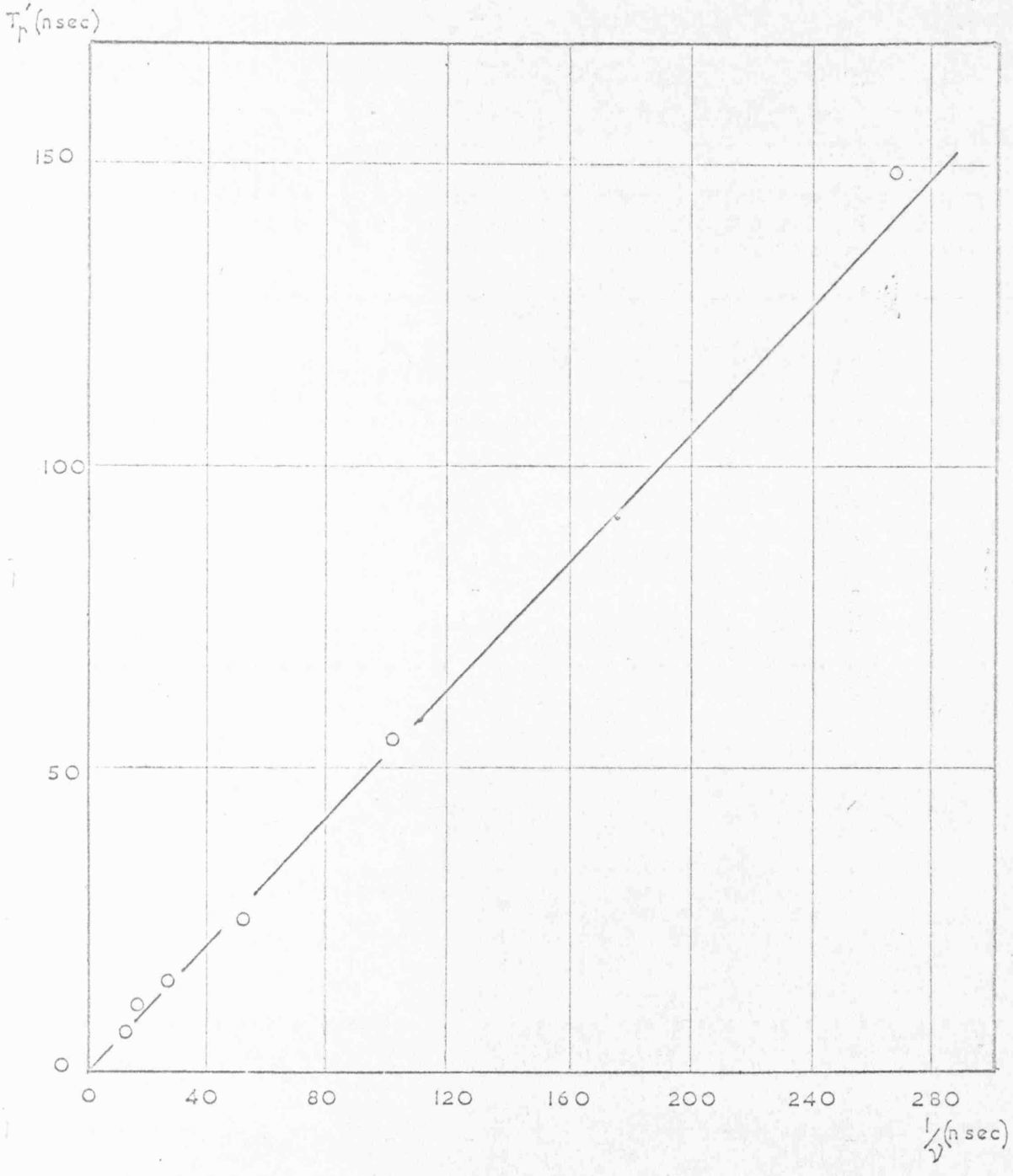

Fig.5.9 Graph of T_p' versus the inverse of the ultrasonic frequency ν .

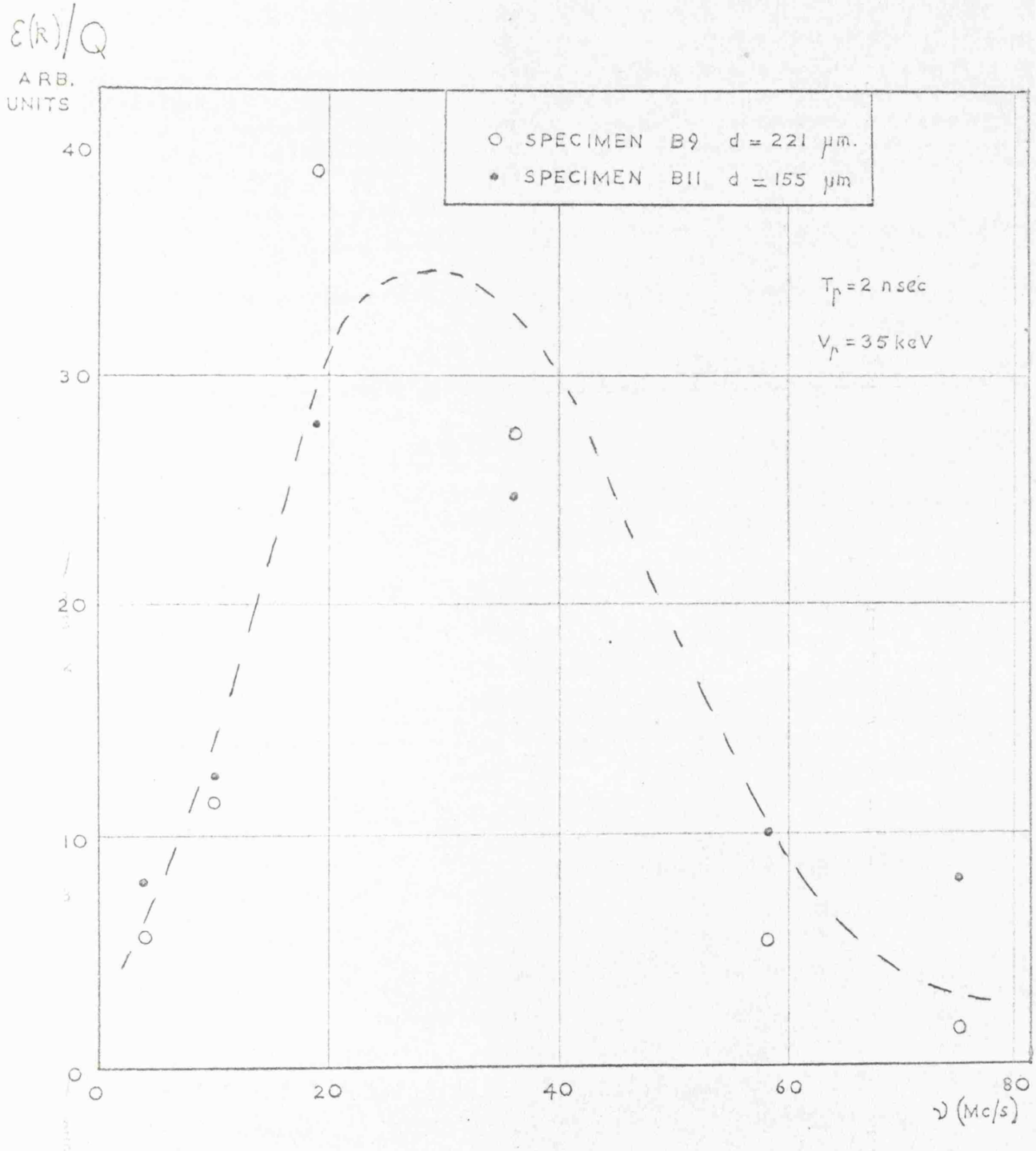

Fig.5.10 Graph showing the values of $\varepsilon(k) / Q$ for six different frequencies.

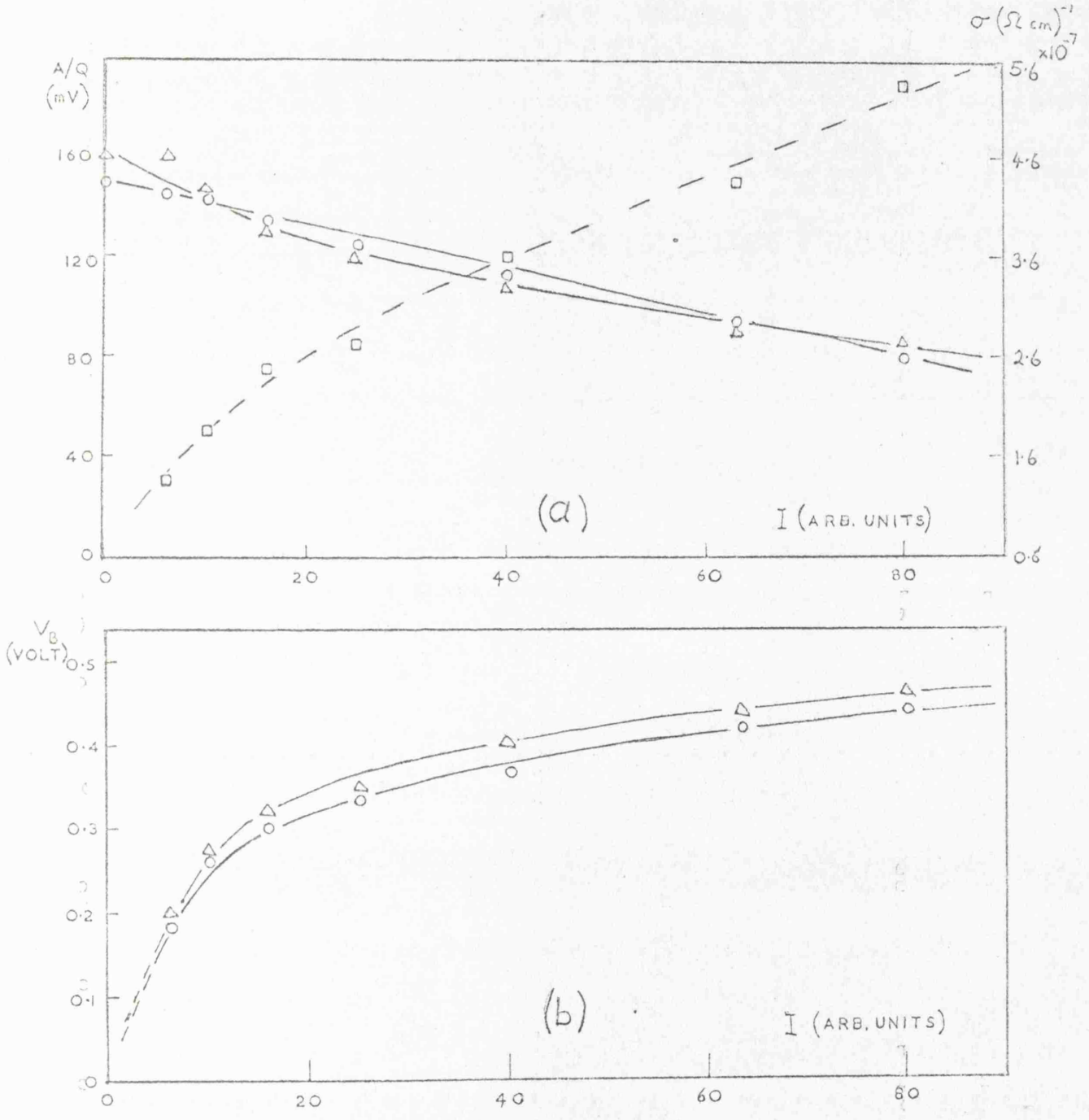

Fig.5.11 (a) and (b) The measured dependence of stress wave amplitude A/Q and the change in barrier height V_B respectively, as a function of light intensity I for two specimens. The increase in conductivity σ (right hand scale) is shown in Fig.5.11 (a) for one of the specimens by the dotted line.

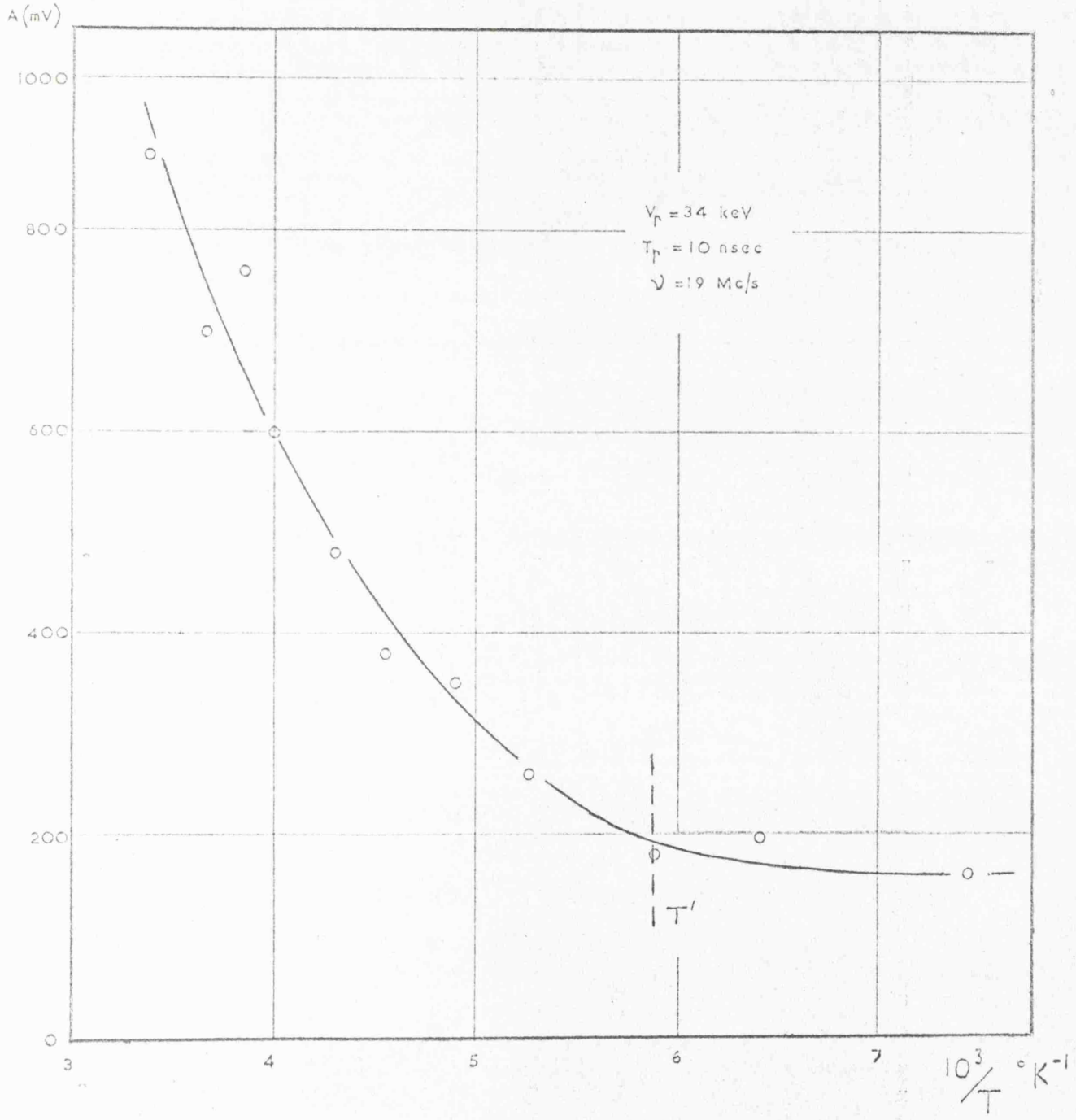

Fig.5.12 The measured dependence of the stress wave amplitude as a function of temperature.

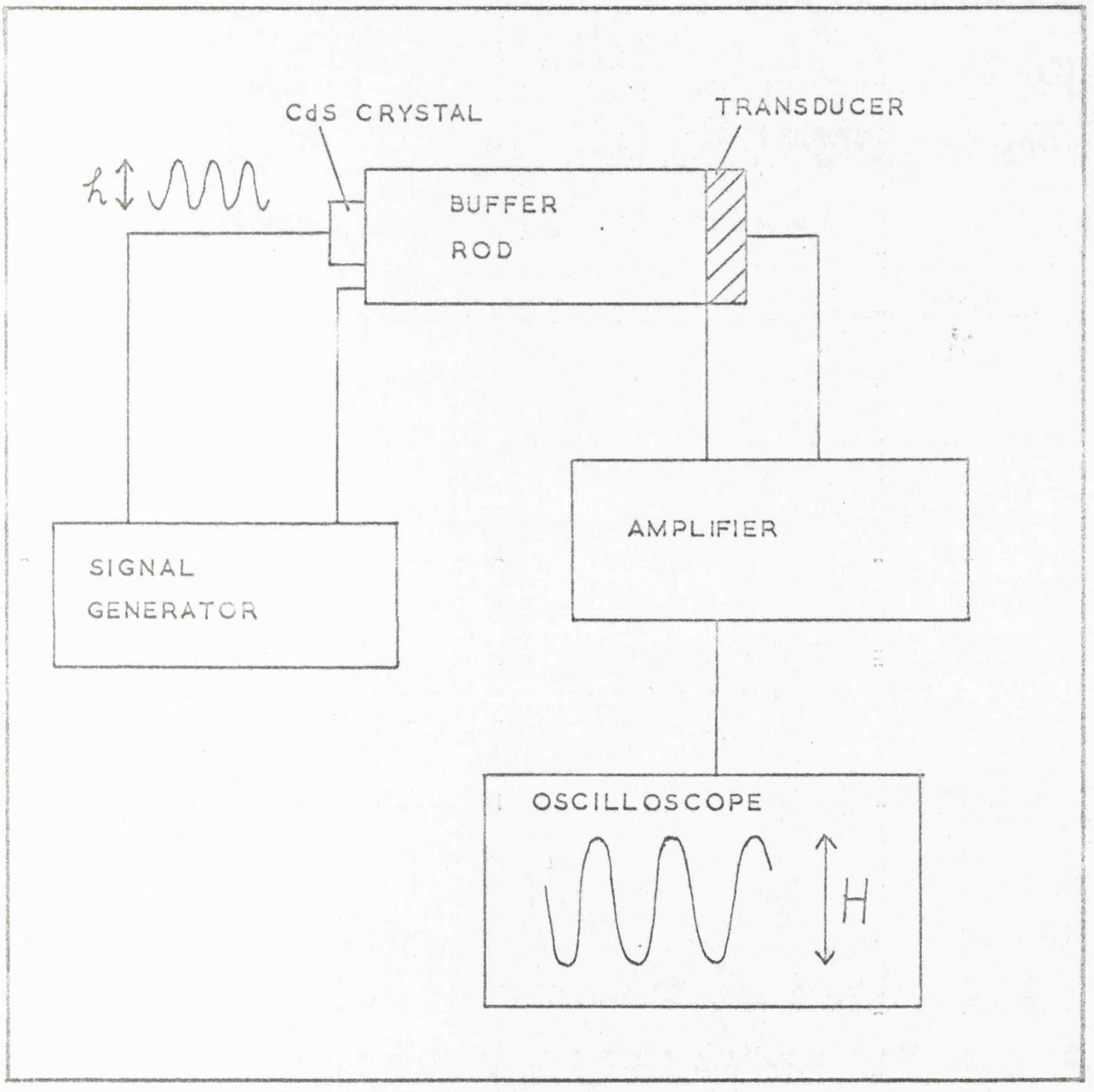

Fig. 6.1 Block diagram indicating the calibration method.

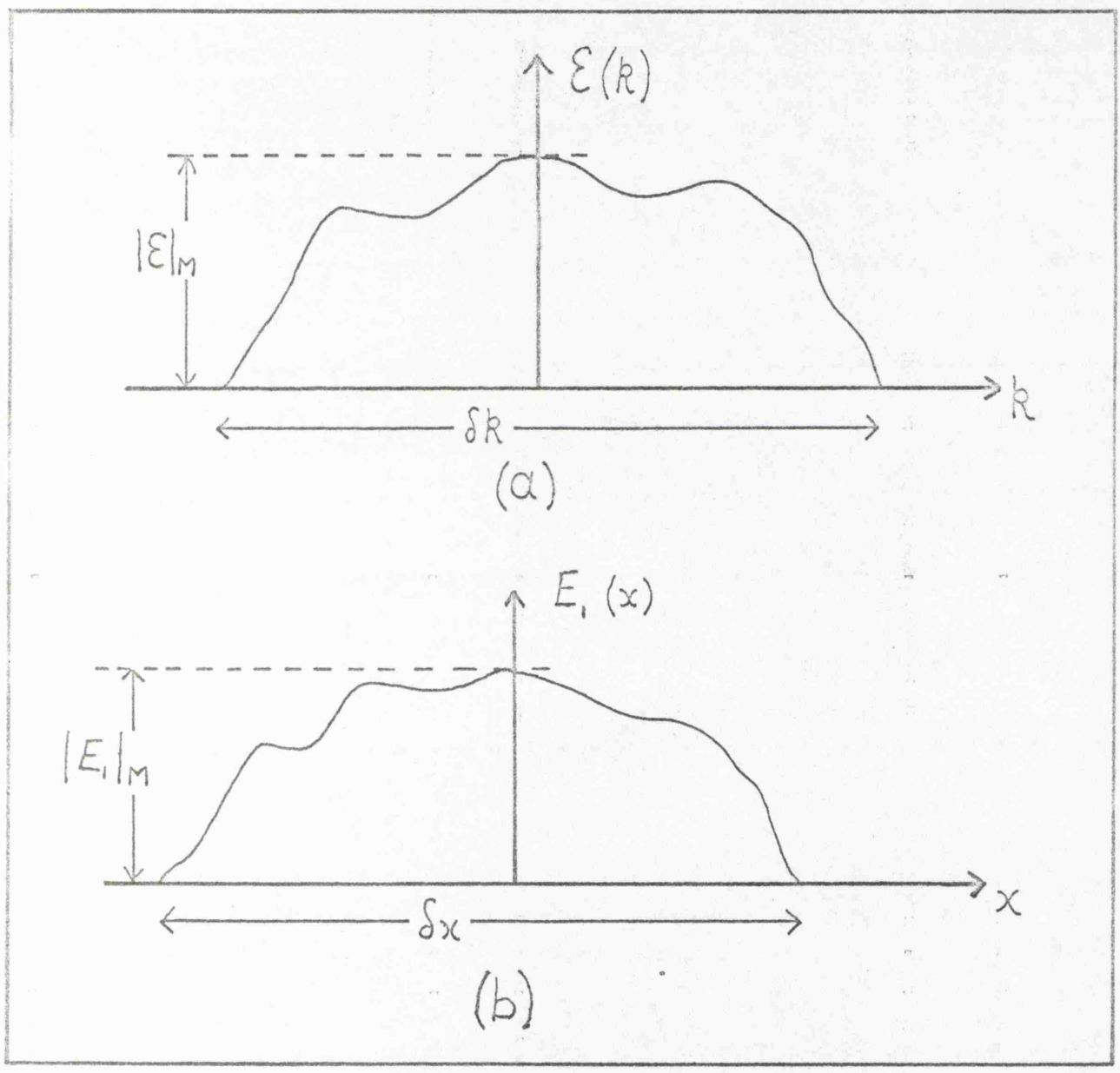

Fig.6.2 (a) and (b) Diagrams showing the possible distributions of $\varepsilon(k)$ and $E_1(x)$ as functions of k and x respectively.

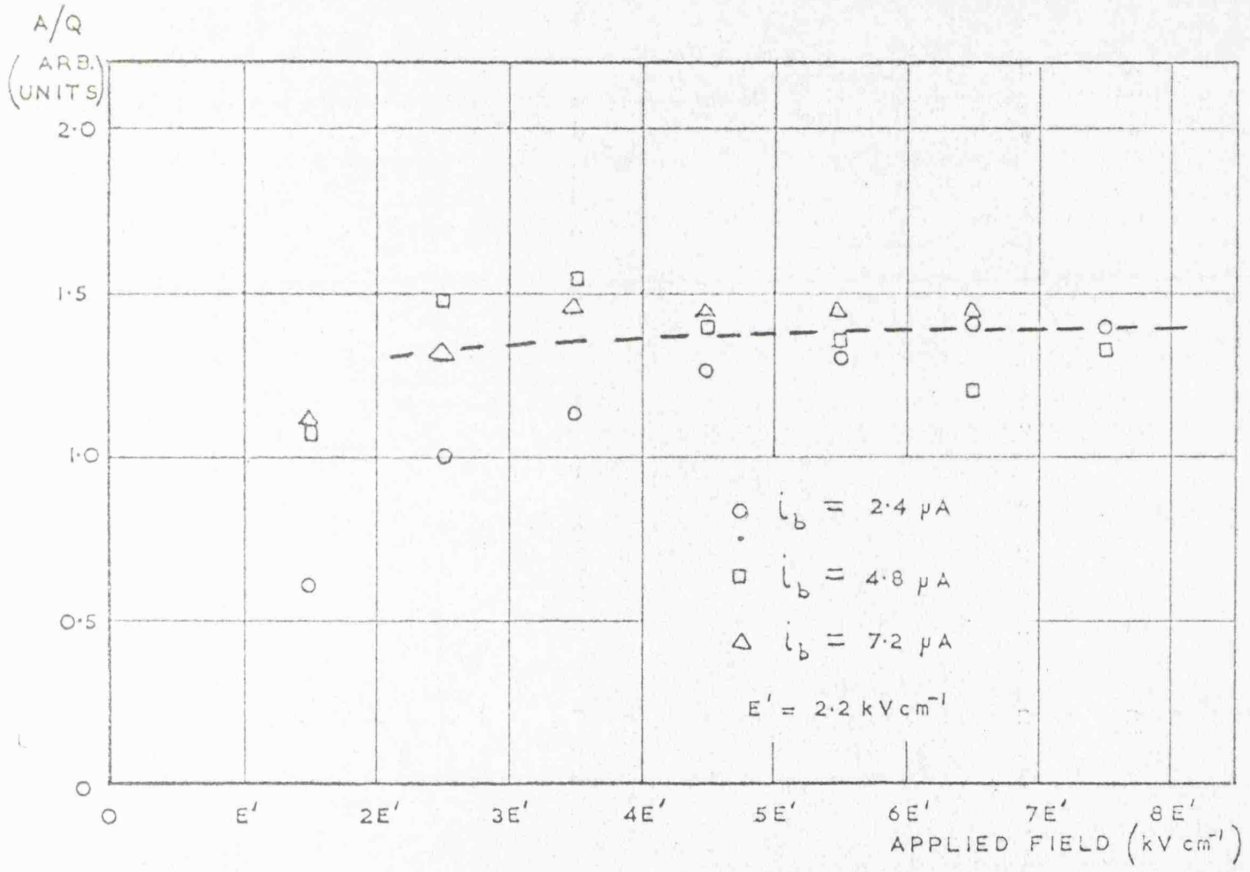

Fig.6.3 Showing the dependence of A/Q on the applied field for different values of the beam current i_b.

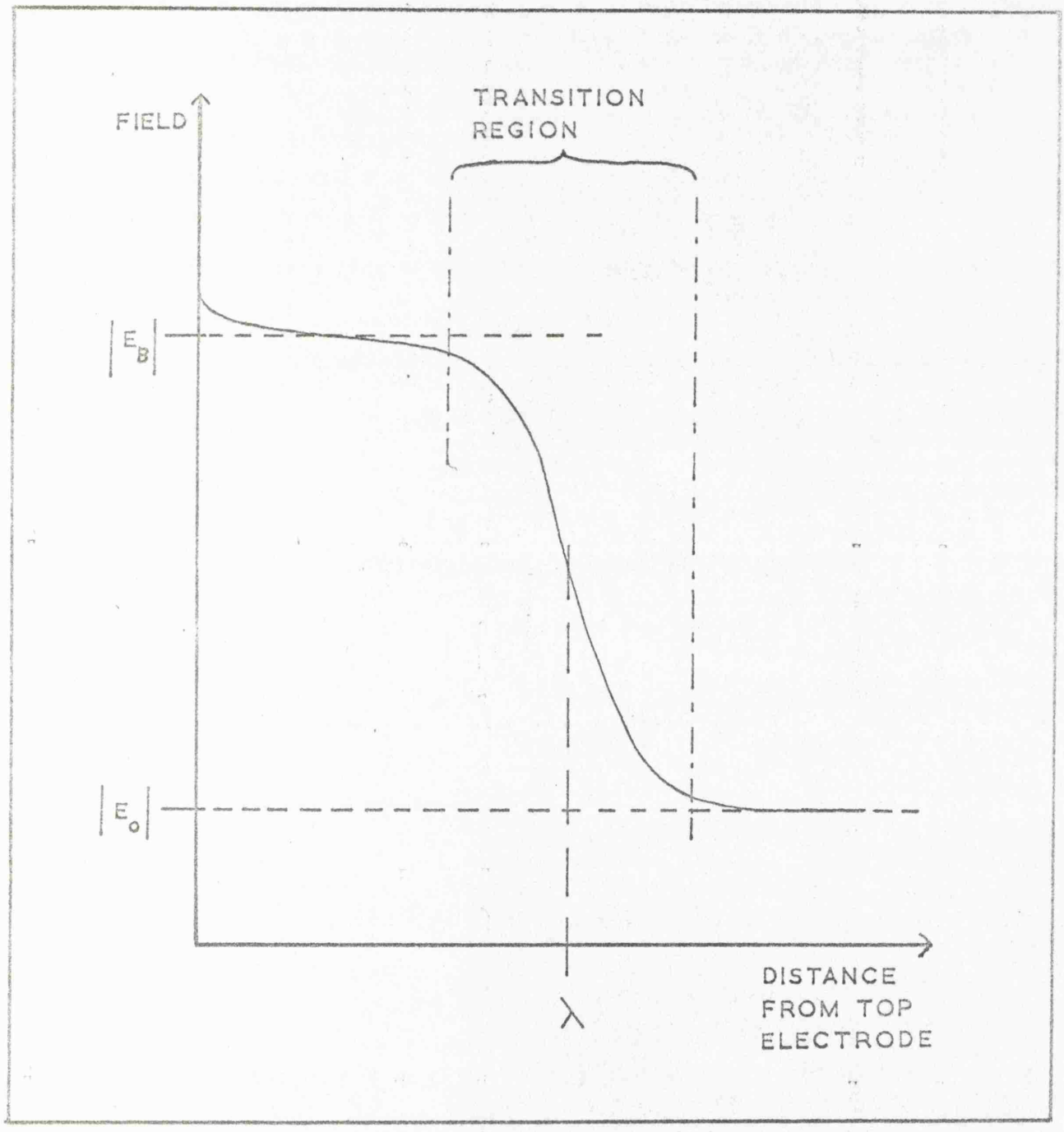

Fig.6.4 Showing the possible field distribution at the barrier in CdS with an applied field $E_o \simeq 3E'$.

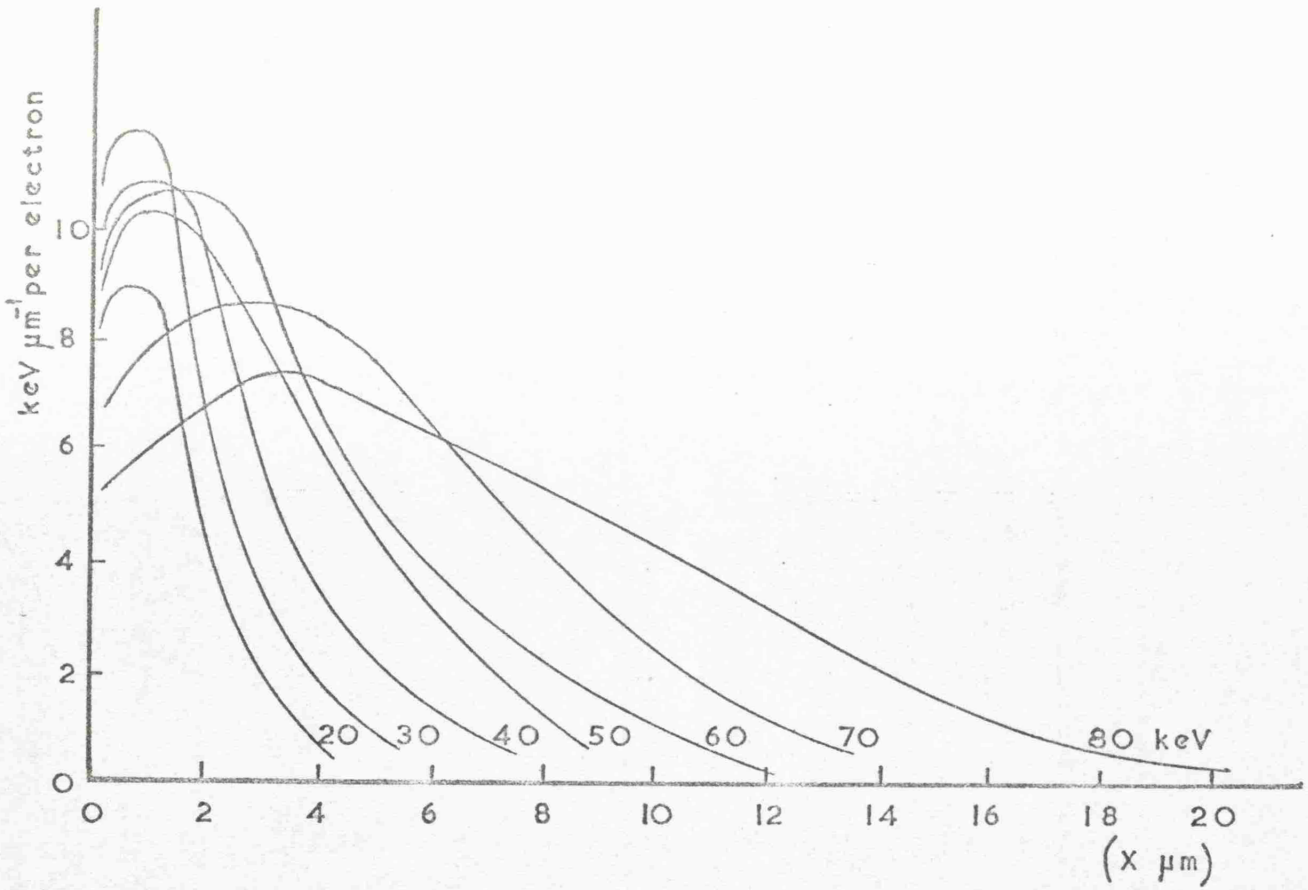

Fig.6.5 Dissipation of the energy of cathode rays, as a function of the depth below the surface for CsI. Units of the ordinates are keV per electron per μm. The parameter is the energy of the incident electron.

After Ehrenberg and King (1963).

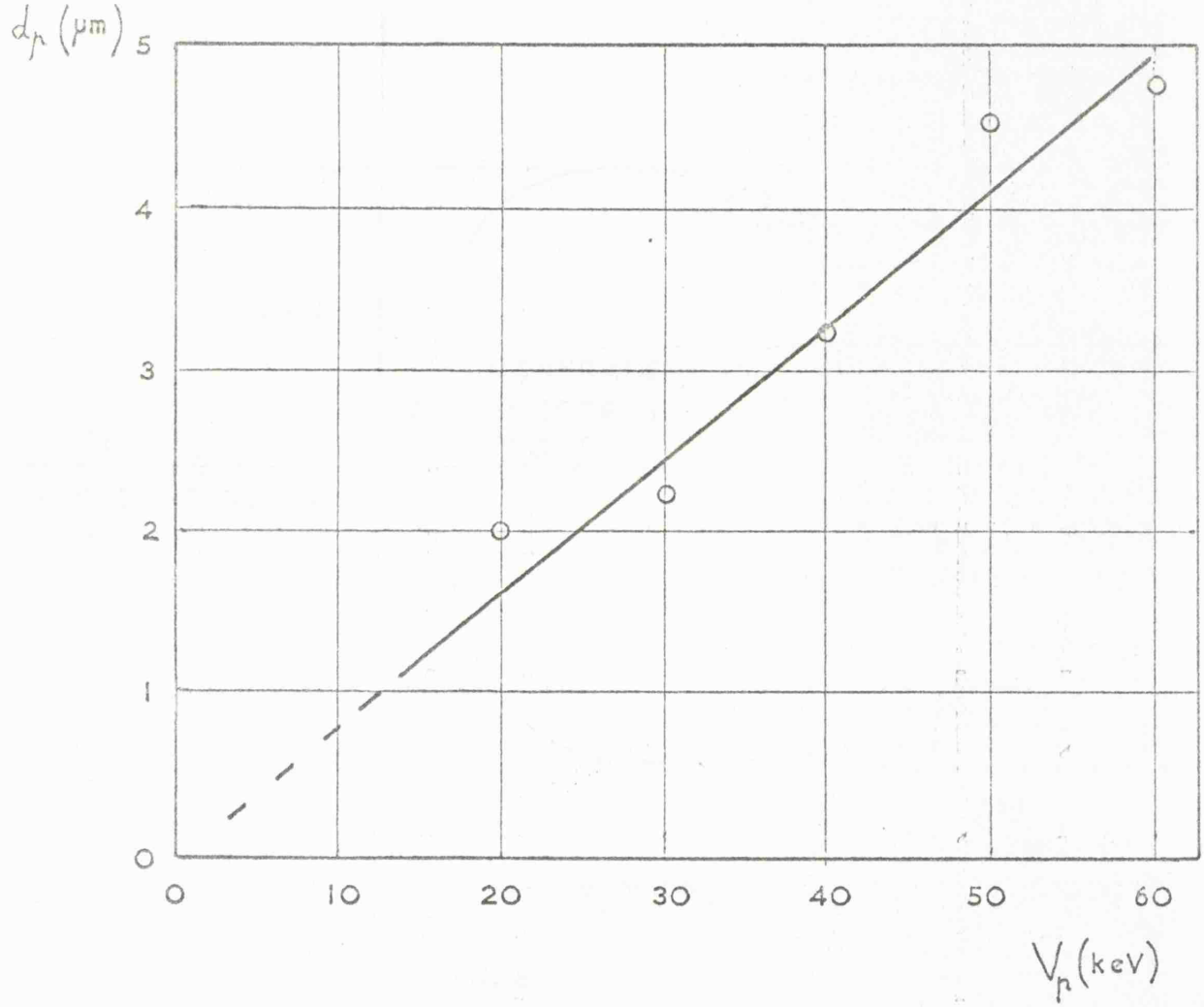

Fig. 6.6 Graph showing the depth d_p below the surface of the halfwidth of the generated electron distribution as a function of the incident electron energy V_p.
After Ehrenberg and King (1963).

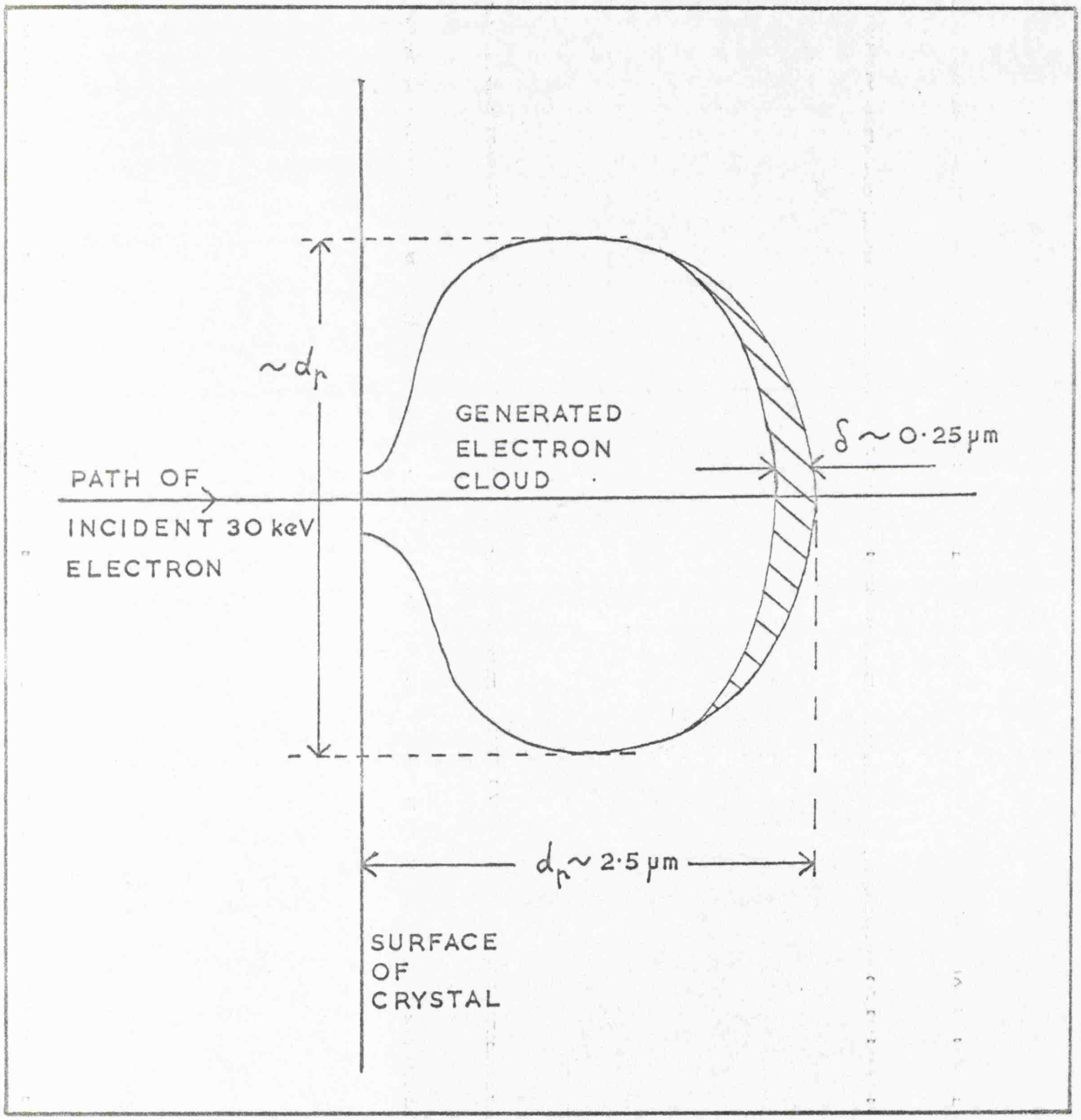

Fig.6.7 Diagram showing the generated electron cloud. The electrons in the shaded region are assumed to escape recombination. After Ehrenberg and Franks (1953).

TABLE I.

THIN FILM TRANSDUCER CHARACTERISTICS.

Details of Recrystallisation.						
Sample No.	Temperature	Time	Atmosphere	Results	Sample Thickness	Fundamental Resonant Frequency.
1. CdS on nesa. Black Cu_2S on top.	550°C.	1 hr.	N_2 1·5 litres per min.	Recrystallisation well marked.	8μm	275 Mc/s
2. As for No.1, but Cu_2S not black.	550°C.	1 hr.	N_2 1·5 litres per min.	Recrystallisation not so evident as for No.1.	14μm	157 Mc/s
3. CdS on nesa. No Cu_2S.	550°C.	1 hr.	$N_2 + S_2$ 1·5 litres per min. flowing over molten sulphur	Recrystallisation not visible to the naked eye.	5μm	440 Mc/s